Université catholique de Louvain
Ecole polytechnique de Louvain
Institut de mécanique, matériaux et génie civil
(iMMC)

Combustion in Homogeneous Charge Compression Ignition engines : experimental analysis using ethyl esters and development of a method to include detailed chemistry in numerical simulations.

Francesco Contino
Mai 2011

Composition du jury:
Prof. G. Winckelmans (président)
Prof. H. Jeanmart (promoteur)
Prof. P. Gerin (promoteur)
Dr. V. Dias
Prof. Y. Bartosiewicz
Prof. T. Lucchini
Prof. F. Foucher
Prof. S. Verhelst

Thèse présentée en vue de l'obtention du grade de docteur en sciences de l'ingénieur

Aknowledgments

I am very grateful to my supervisors, Hervé Jeanmart and Patrick Gerin. Hervé taught me a lot, in soft skills as well as in various scientific topics. He was always available for discussions and excited by new ideas and developments. His open-mindedness and support were invaluable contributions to my thesis. Patrick had a great impact on this work thanks to his infectious passion and his way of structuring thoughts. Performing my thesis under their supervision was a great pleasure and honor.

I would like to thank Véronique Dias who really added a new dimension to my thesis. I would not have been so fond of combustion chemistry for her not patiently explaining the mysteries of it. She was also extraordinarily supportive during my thesis.

I am very grateful to Tommaso Lucchini who gave me the great opportunity to work with him. He adopted me as a baby OpenFoamer and with careful listening and challenging questions raised me to walk by myself within the lines of code. His in-depth knowledge of the many aspects of engine simulations made him a terrific teacher. I also really enjoyed my time in Milan with the internal combustion engine group and I really thank Professor Angelo Onorati and all his team for making me feel like home with their warm welcome.

A great part of this work was made possible thanks to the hearty welcome of Christine Mouaïm-Rousselle and Fabrice Foucher who agreed without hesitation to host my experiments in Université d'Orléans. I was really like a kid in a candy store when they invited me to their laboratory. They both showed great enthusiasm for my research project which really

allowed me to reach my objective and even more. Also a special thanks to Bruno Moreau and his team from Laboratoire Prisme without whom I would never have managed to run my experiments on HCCI. For these guys nothing is impossible, I will not be afraid to completely change a test bench in a day anymore.

I would like to thank Yann Bartosiewicz for his constructive remarks and for accepting to be in my supervisory panel, Sebastian Verhelst for his valuable comments and for accepting to be in my jury, and Grégoire Winckelmans who accepted to chair the jury and diligently read this work.

This thesis has been financially supported by the F.R.S.-FNRS with a Research Fellowship. The numerical simulations of this thesis have been performed on the high-performance computing resources of UCL managed by the Institut de Calcul Intensif et Stockage de Masse.

I would like to thank all my colleagues and friends from TFL (former TERM) with whom I have spent so many good times. We have sometimes generated more heat than light but I always felt a very friendly atmosphere. Among them, I would like to name Jean-Marie and Laurent for their precious advices, Nicolas who have carefully read some parts of this work, Catherine who shared my office but also some of my stress, Julien who willingly stepped in to present one of my work, Matthieu who helped me so many times that I stopped counting, and all others who generously contributed with much appreciated inputs : Amel, Antoinette, Benjamin, François, Frank, Isabelle, Ivan, Julien, Lili, Michel, Nicolas, Philippe, Timothée, Xavier, Yves.

I am very grateful to my family and friends for their encouragements and specifically to my parents who patiently guided me for the first steps in the path towards this Ph.D.

I am deeply grateful to Céline for her dedicated support throughout my thesis, for being understanding when I have been abroad or when I was pressed for time, but most importantly for the happiness of being with her. I also thank Emma for making me so joyful when she grins.

Extended Summary

In the global energy context, many solutions are suggested to change our energy dependence and solve our CO_2 emission issues. Until now, no unique solution has been proposed but rather a range of technologies that cover all the main aspects of our day-to-day life. For transportation, and more specifically for internal combustion engines, biofuels are often mentioned as a possible alternative to fossil fuels. Yet many people argue that they could hardly replace oil. The main problem is the low efficiency of the conversion from biomass to biofuels which implies other main issues like land use and food competition. This low efficiency is mainly related to the specific fuel properties required by conventional engines (spark ignition and compression ignition engines).

More simple conversion routes using less energy-consuming steps can be used. They produce less refined fuels from the same feedstock or from biomass wastes not or barely used nowadays. However, the major drawback of these products is then the lack of compatibility with conventional engines. Instead of adapting the fuel to the engines, the opposite has been put forward recently with an engine burning any kind of fuel. The homogeneous charge compression ignition (HCCI) engine is a new concept based on this principle. This engine does not intrinsically rely on specific fuel properties. Given that a fairly homogeneous air-fuel mixture is prepared, it can be operated on a large range of fuels. One of the main challenges, that still restricts the operation of this engine, is the limited HCCI operating zone (speed and load range).

In the first part of this thesis, we analyzed the esters produced from

fermentable wastes by a simple biochemical process. We investigated experimentally the impact of these esters on the HCCI working zone, and the combustion characteristics of blends of these esters.

These experiments confirmed that the ethyl esters could be used in HCCI engines on a large range of equivalence ratios. We identified the key parameters of the fuel blend composition having an effect on the ignition timing, and thereby on the HCCI working zone. However, the successful implementation of these esters still requires further analysis such as the use of ignition promoters (e.g. n-heptane) that could help decreasing the inlet temperature.

In practice, the development of new engine concepts and the characterization of fuels rely more and more on numerical simulations. Computational fluid dynamics (CFD) simulations of chemically reactive flows in internal combustion engines can, for instance, accurately predict the performance of a particular fuel or the pollutant emissions of a specific engine configuration. However, the accurate and comprehensive modeling of the highly nonlinear combustion processes of realistic fuels is extremely demanding. It requires detailed mechanisms that involve hundreds of chemical species and thousands of elementary reactions. The computational costs of these simulations are generally prohibitive. This implies, first, that fairly detailed CFD simulations can only include global mechanisms, which only describe the main steps of the combustion; and, second, that very detailed reaction mechanisms are mainly limited to simplified systems.

In the second part of this thesis, we developed a new method that significantly mitigates the computational burden of detailed chemistry in complex CFD simulations.

The developed numerical method, named tabulation of dynamic adaptive chemistry (TDAC), speeds the CFD simulations up to 900 times with a very small simulation error compared to the direct numerical integration of the combustion mechanisms. This method therefore allows the use of detailed reaction kinetics in the simulations of HCCI engines. The future developments should focus on extending it to spark ignition and compression ignition engine simulations.

Contents

1 Introduction **1**
1.1 Motivation and outline 1
1.2 Homogeneous charge compression ignition engines 3
1.3 Esters produced by the acidogenesis route 8
1.4 Combustion kinetics in HCCI engines 13
1.5 Combustion chemistry in numerical simulations 19

2 HCCI experiments of pure ethyl esters **27**
2.1 Introduction 27
2.2 Experimental setup 29
2.3 Results 35
2.4 Conclusion 44

3 HCCI experiments of tri-component ethyl ester blends **45**
3.1 Introduction 45
3.2 Fuel blends 47
3.3 Experimental setup 50
3.4 Results 52
3.5 Conclusion 61

4 Iterative method for mechanism reduction **63**
4.1 Introduction 63
4.2 Reduction methodology 65
4.3 Computational setup 69
4.4 Operating zone 76

4.5 Conclusion 83

5 Tabulation of Dynamic Adaptive Chemistry 85
5.1 Introduction 85
5.2 Computational methods 87
5.3 Results 94
5.4 Conclusion 104

6 Reduction methods in TDAC 105
6.1 Introduction 105
6.2 Reduction methods 106
6.3 Computational setup 119
6.4 Results 122
6.5 Conclusion 135

7 Conclusion and perspectives 137

References 141

A Molecular structure of the esters 151

B Supplementary material for Chapter 4 159

C Pseudo-code of the methods in Chapter 6 165

D Supplementary material for Chapter 6 177

List of acronyms and symbols

AFR	Air-fuel ratio [-]
ATDC, BTDC	After or before top dead center
BDC	Bottom dead center
CAD	Crank angle degree
CAx	Crank angle where x% of the heat is released [CAD]
CI	Compression ignition (diesel engine)
CoV	Coefficient of variation [%]: CoV = std/mean
DAC	Dynamic adaptive chemistry
DRG	Directed relation graph
DRGEP	Directed relation graph with error propagation
EFA	Element flux analysis
EGR	Exhaust gas recirculation
EOA	Ellipsoid of accuracy : region where the ISAT algorithm can perform a linear approximation of a stored solution
EtAc	Ethyl acetate ($C_4H_8O_2$)
EtBu	Ethyl butyrate ($C_6H_{12}O_2$)
EtOH	Ethanol (C_2H_6O)
EtPr	Ethyl propionate ($C_5H_{10}O_2$)
EVO	Exhaust valve opening [CAD]
HCCI	Homogeneous charge compression ignition
HRR	Heat release rate [J/CAD]
IMEP	Indicated mean effective pressure [bar] : IMEP = $\text{Work}_{\text{cycle}}/V_d$
ISAT	In situ adaptive tabulation
IVC	Inlet valve closure [CAD]

LHV	Lower heating value [MJ/kg]
MPRR	Maximum pressure rise rate [bar/CAD]
NO_x	Nitrogen oxides (include NO and NO_2)
ODE	Ordinary differential equation
PFA	Path flux analysis
PM	Particulate matter
rpm	Revolutions per minute
SI	Spark ignition (gasoline engine)
TDAC	Tabulation of dynamic adaptive chemistry
TDC	Top dead center
uHC	Unburned hydrocarbon
VFA	Volatile fatty acid
$\mathbf{A}$	Mapping gradient matrix used by ISAT to perform the linear approximation of a stored solution
$k_{f,i}$, $k_{b,i}$	Forward and backward rate constants of reaction i
	Arrhenius formulation : $k_{fi} = \left(A_i T^{n_i} e^{\frac{-E_j}{RT}}\right) F_i$;
	(units depend on reaction) $k_{bi} = \dfrac{k_{fi}}{K_{ci}}$.
ν'_{ij} , ν''_{ij} , ν_{ij}	Forward, backward and net stoichiometric coefficient of species j in reaction i
ω_i	Net production rate of reaction i [mol/(cm^3.s)]
	$\omega_i = \omega_{fi} - \omega_{bi}$, where $\omega_{fi} = k_{fi} \prod_{j=1}^{N_s} C_j^{\nu'_{ij}}$
	and $\omega_{bi} = k_{bi} \prod_{j=1}^{N_s} C_j^{\nu''_{ij}}$
ϕ	Equivalence ratio : $\phi = \dfrac{\mathrm{AFR_s}}{\mathrm{AFR}}$
ψ	Composition of a thermochemical state : $\psi = \{Y_i, T, p\}$
r_{AB}	Contribution coefficient of species A to species B
$\mathbf{R}$	Reaction mapping: solution after a given time step of the ODE system describing the composition evolution
R_{AB}	Strength of the path leading from species A to species B
V_d	Displacement volume [cm^3]: $V_d = \frac{\pi}{4}\mathrm{bore}^2 \cdot \mathrm{stroke}$
Y_i	Species mass fraction

CHAPTER 1

Introduction

1.1 Motivation and outline

Environmentally sustainable transportation is among the most important challenges that we have to face in the near future if we want to solve our energy dependence and CO_2 emission issues. Biofuels are often mentioned as a possible solution to replace fossil fuels. However, in many cases, the viability of this alternative is questionable. Its low energy efficiency and low productivity are often pointed out as two major drawbacks.

These problems are mainly related to the specific fuel characteristics required by conventional internal combustion engines (ICE). To achieve these requirements, energy-consuming processes, for refining or transformation, are required. More simple conversion routes using less intermediate steps can be used instead. They produce less refined fuels from the same feedstock or from biomass wastes not or barely used nowadays. However, the major drawback of these fuels is then the lack of compatibility with conventional engines.

Instead of adapting the fuel to the engines, the opposite has been put forward recently with an engine burning any kind of fuel. A new engine concept is based on this principle: the Homogeneous Charge Compression Ignition (HCCI) engine. This engine does not intrinsically rely on specific fuel properties. Given that the air-fuel mixture is prepared properly, it can be operated on a large range of fuels. This multi-fuel ability could also be used to solve the two main challenges that still restrict the

operation of this engine: the limited speed-load range and the control of the ignition.

The first part of this thesis describes the analysis of esters, produced from fermentable wastes through a biochemical process, and used in a HCCI engine. To help directing the process towards the production of more desirable mixtures, we investigated whether these esters have different impact on the HCCI engine, and we analyzed whether a region of blends of these esters is more appropriate for engine operation.

When developing new engine concepts or fuels, numerical simulations are more and more considered as an essential tool. Computational fluid dynamics (CFD) simulations of chemically reactive flows in ICE can, for instance, accurately predict the performance of a particular fuel or the pollutant emissions of a specific engine configuration. Including realistic fuel chemistry requires, however, detailed mechanisms that describe accurately and comprehensively the complex combustion reaction network. The computational cost of these simulations is generally prohibitive and strongly restricts the use of detailed mechanisms to very simple cases.

In the second part of this thesis, we analyzed whether a numerical method could be used to significantly reduce these computational cost and help integrating very detailed mechanisms in CFD simulations of HCCI engines.

This manuscript is organized in six chapters: the first chapter provides some background information, then the next two chapters report the experimental investigations, and finally the last three chapters discuss the numerical simulation methods.

In the following sections of this chapter, we first describes the principles of the HCCI engine with its advantages and its drawbacks. Then we introduce the characteristics of the esters produced from wastes and we briefly describe the biochemical production process. We also present the chemical kinetic pathways leading to the auto-ignition and controlling the main combustion event in HCCI engines. Finally, we examine how the existing numerical methods can reduce the kinetic mechanisms to use them in CFD simulations.

Chapter *two* presents the experimental investigation of the esters

presented in this introduction. It compares these esters to ethanol with respect to the HCCI working zone and the combustion characteristics. It is mainly based on a paper published in *Energy & Fuel*.

Chapter *three* reports the experimental investigation of blends of these esters. It presents the mixture design for tri-component blends and identifies the type of interaction between these components. It is based on a paper published in *Energy & Fuel*.

Chapter *four* describes a first step towards accommodating realistic fuel chemistry in complex CFD simulations. We first present an iterative method to reduce the size of the mechanism and then we define a new way to compute the HCCI working zone based on simulation results. The content of this chapter is mainly based on a paper published in *SAE Technical Paper*.

Chapter *five* presents an innovative method to include very detailed mechanisms in CFD simulations. This method, named tabulation of dynamic adaptive chemistry (TDAC), couples two different levels of reduction and takes advantage of the synergy between them. This chapter is mainly based on a paper published in the *Proceedings of the Combustion Institute*.

Chapter *six* further analyzes the TDAC method. After presenting five selected reduction methods, we compare their behavior and their performance within the TDAC framework.

Chapter *seven* outlines the main conclusions of this work and presents some perspectives.

1.2 Homogeneous charge compression ignition engines

1.2.1 Principles

The HCCI engine is a rather new concept with features from both compression ignition (CI) and spark ignition (SI) engines. This alternative combustion mode has been first investigated in 1979 by Onishi et al. [1] and Noguchi et al. [2] while trying to control the irregular combustion of lean mixtures in ported 2-stroke gasoline engines. Following the work

on 2-stroke engines, this new concept has been applied to 4-stroke engines in 1983 by Najt and Foster [3] and extended in 1989 by Thring [4], who introduced the name HCCI that is now commonly used for these engines.

Like in conventional SI engines, the fuel and air are mixed together to obtain an homogeneous charge at the beginning of the compression stroke. As the piston compresses the charge, the mixture heats up and auto-ignites close to the top dead center (TDC), similarly to conventional CI engines.

There are two main requirements for HCCI: obtain a homogeneous air-fuel mixture, and reach the auto-ignition temperature close to TDC, for maximum efficiency. These requirements are met in different ways according to the fuel volatility and the auto-ignition temperature. The fuel can be port injected or directly injected at the beginning of the compression stroke. The intake air can be heated before entering the cylinder or the compression ratio can be adapted. The air-fuel mixture can also be heated by mixing with part of the exhaust gas. In this case, several strategies have been developed to take advantage of the sensible heat in the exhaust gas: conventional recycling through a bypass valve, early opening of the inlet valve to direct some of the exhaust gas in the intake plenum and negative valve overlapping to trap a portion of the exhaust gas in the combustion chamber. The later is generally preferred because it avoids exchanging heat in the exhaust or inlet plenums [5].

The heat release characteristics of the HCCI engine are quite different from that of the SI and CI engines. In SI, the combustion starts near the spark plug and propagates throughout the chamber. The burned gas is separated from the unburned gas by the flame front, a small region where all the combustion reactions take place. The cumulative heat released in a SI engine is

$$Q = \int_{\text{mix.}} q \; dm \; , \tag{1.1}$$

where q is the heating value per unit mass of air-fuel mixture and dm is the mass of the mixture that is converted to burned gas in this flame front (see Figure 1.1a).

In a CI engine, the fuel injected in the cylinder is mixed with the compressed hot air. A small part of the mixture is in the conditions to auto-ignite, whereas the release of most of the heating value of the fuel is controlled by the molecular diffusion during the air-fuel mixing. The heat released is the sum of the premixed combustion and the diffusion combustion:

$$Q = \int_{\text{premix.}} m_p \; dq_p + \int_{\text{dif.}} m_d \; dq_d \; , \tag{1.2}$$

where m_p and dq_p are the mass and heating value of the air-fuel mixture involved in the premixed combustion, m_d and dq_d are the mass and heating value of each zone involved in the diffusion flame (see Figure 1.1b). The heating value depends on the local equivalence ratio which explains the variations in the illustration of Figure 1.1b.

In HCCI, the air-fuel mixture simultaneously burns throughout the combustion chamber:

$$Q = \int_{\text{mix.}} m \; dq \; , \tag{1.3}$$

where m is the mass of air-fuel mixture in the combustion chamber and dq is the heat released by the combustion reactions (see Figure 1.1c).

1.2.2 Advantages and drawbacks

To a certain extent, the HCCI engine combines the best features of SI engines and CI engines: diesel-like efficiency and gasoline-like emissions (see Figure 1.2). It is operated unthrottled and at low equivalence ratio which gives high thermal efficiency[1]. A homogeneous mixture eliminates fuel-rich diffusion combustion which results in a great reduction of particulate matter (PM) emissions. Finally, the auto-ignition occurs in the entire combustion chamber which eliminates high temperature flames

[1] At low equivalence ratio, the temperature and the proportion of triatomic species (CO_2 and H_2O) in the burned gas decrease. Both effects decrease the specific heat of the burned gas and increase the effective value of the ratio of specific heats over the expansion stroke. For a given compression ratio, the expansion work per unit mass of fuel is increased, which also increases the thermal efficiency.

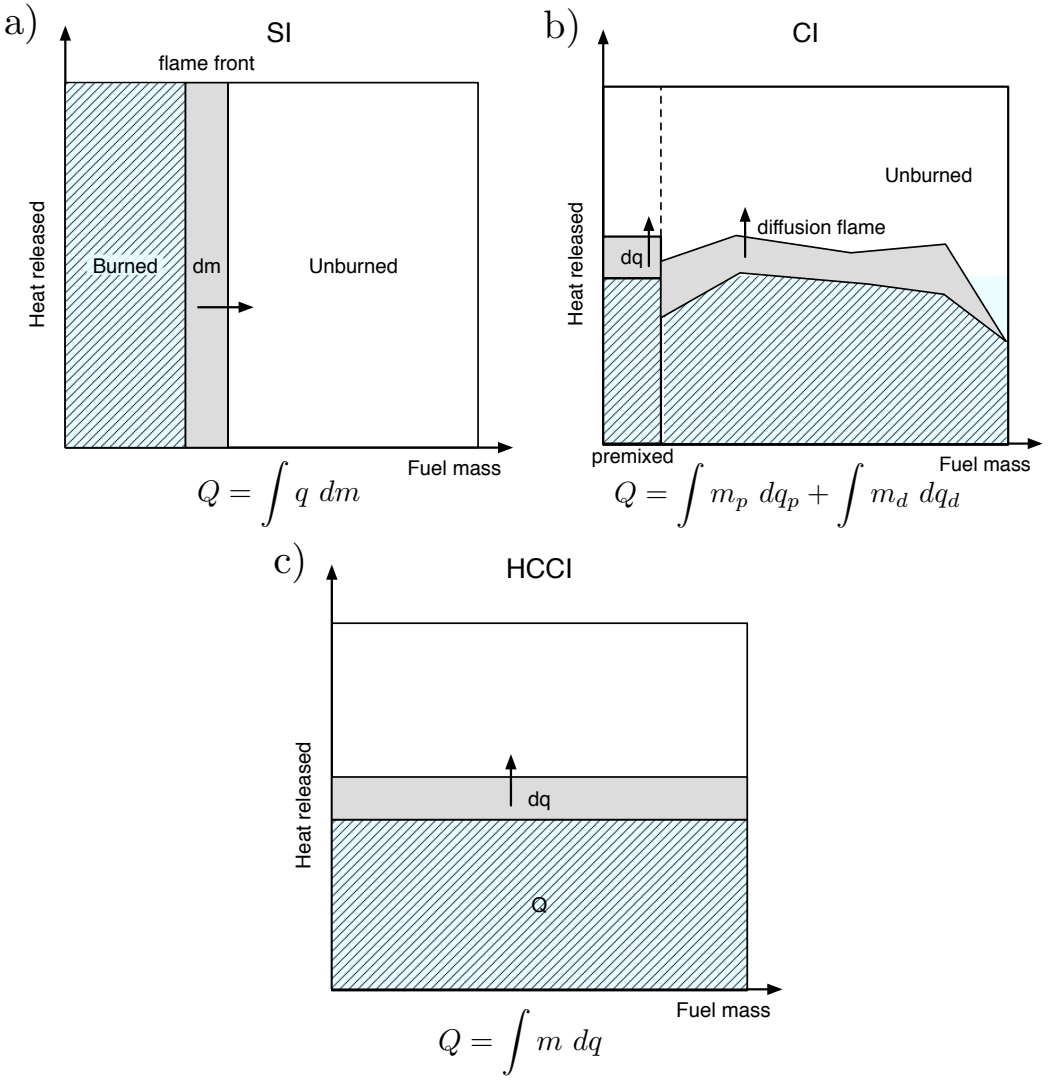

Figure 1.1: The heat release characteristics of a) SI (flame front), b) CI (diffusion flame), and c) HCCI (bulk combustion) engines [5].

and the resulting NO_x emissions.

There are still some challenges for the HCCI engine: no direct control on the onset of the combustion, increased hydrocarbon and carbon monoxide (CO) emissions, and a limited working zone. The control of the HCCI engine is particularly difficult because there is no direct means to trigger the ignition unlike the spark of the SI engine or the

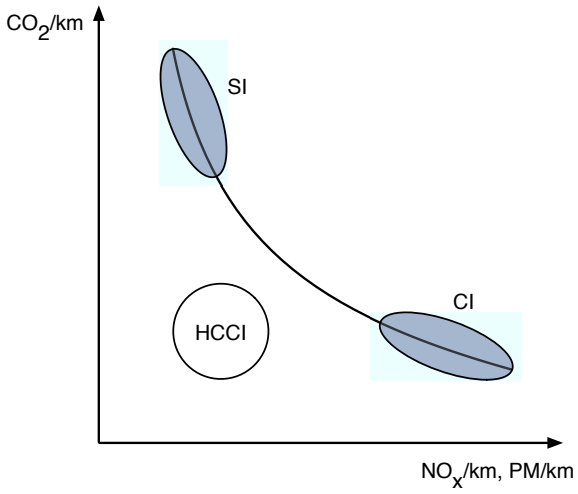

Figure 1.2: The HCCI engine combines the best features of SI and CI: diesel-like thermal efficiency and gasoline-like, with three-way catalyst, PM and NO_x emissions.

injection of the CI engine. The ignition is only controlled by the reaction kinetics which requires to prepare the air-fuel mixture such that it will reach the auto-ignition conditions close to TDC. In HCCI, like in SI, part of the air-fuel mixture remains in the crevices during the main combustion. In SI, the unburned fuel leaving the crevices during the expansion stroke is consumed because of the high temperature (around 2500 K) of the burned gas. However, in HCCI, the temperature of the burned gas is lower than in SI (around 1600K), thus the unburned fuel is not totally consumed. This results in increased hydrocarbon and CO emissions. At the lowest loads the peak temperature is even too low (around 1200K) to sustain the CO to CO_2 conversion which leads to ignition problems. At higher loads, because the combustion simultaneously takes place throughout the combustion chamber with a rapid rate of heat release, the bulk combustion leads to very high pressure rise rates which can damage the engine. These two phenomena define the main operating limits of the HCCI engine: the misfire limit and the knocking limit. At higher engine speeds, the auto-ignition is more difficult be-

cause there is less time for the reactions to initiate combustion. Because thermal conditions are very important, cold starts are also an issue for this engine [6].

While a lower equivalence ratio increases the thermal efficiency, it also reduces the specific power and requires engines with higher displacement to obtain a specific power output. This is in opposition to the current downsizing trend in the engine industry.

Because this engine is controlled by reaction kinetics, it is also a very useful tool to investigate auto-ignition kinetics in engine conditions, and apply the findings to the conventional engines.

1.2.3 Multi-fuel capability

The HCCI engine does not rely on specific fuel physicochemical properties and is inherently fuel flexible as long as the fuel can be fully vaporized and sufficiently mixed with air. Christensen et al. [7] have shown that it could be operated on virtually all liquid fuels by using a variable compression ratio to obtain auto-ignition close to TDC. Conveniently, this flexibility allows using the fuel formulation to help controlling the engine or extending the operating range, i.e. smoothing the higher loads and promoting the lower loads. Moreover, the HCCI engine can also be run with low-grade fuels. It avoids using further energy intensive separation processes and thereby improve the efficiency of fuel production processes. This has been illustrated by Mack et al. using wet ethanol containing up to 60% of water [8], which can improve the net energy gain from 21% to 55% of the total energy output. It is also the basic idea that is further investigated in the experimental part of this thesis, where esters produced by a biochemical process are used. More details about these esters are presented in the next section.

1.3 Esters produced by the acidogenesis route

The acidogenic fermentation (acidogenesis) is one of the first steps in the anaerobic digestion of complex organic materials. After the hydrolysis of the biopolymers present in the organic matter into soluble monomers,

the acidogenic bacteria convert them into volatile fatty acids (VFA): mainly acetic, propionic and butyric but also isobutyric, valeric and isovaleric acids. This fermentation also produces hydrogen and carbon dioxide. The conventional anaerobic digestion proceeds with the acetogenic and methanogenic fermentations and produces biogas (mostly methane with a high proportion of CO_2) [9–11]. The objective is here to cut this process before the biogas production and directly use the product of the acidogenesis.

The anaerobic conversion is a natural and well-known process that has been extensively used in the treatment of polluting compounds (e.g. agroindustrial waste, wastewater, crop residues, ...) to generate a product that can be reused in a natural environment without detrimental ecological effects [9]. However, given its easy implementation and its ability to convert many types of biomass, a second objective is the treatment of waste streams for the production of specific organic products. In particular, we will focus here on the production of transportation fuels.

Compared with the production of biofuels from specific high-value biomass feedstock such as sugar rich, starch rich or oily substrates, the major advantage is that this process uses low-grade wastes as raw material for the production. Therefore, the acidogenesis is not competing against other agroindustrial processes but it is rather a complementary treatment applied to the remaining low-grade biomass.

Other important advantages of this fermentation process include: no sterilization requirements, adaptive capacity owing to microbial diversity, the capacity to use mixed substrates, and the possibility of a continuous process [9].

After the fermentation step, the recovery of the VFA from the fermentation broth requires the use of an extraction step. The VFA are generally in low concentration, 1-20 g/l [10–13], and the energy intensive extraction step therefore requires careful identification of what is the desired output and the level of refining that should be obtained.

To guarantee the maximum efficiency of the overall process, the extracted VFA should be directly used in the ICE. However, materials resistance is generally an issue when using acids. Therefore, one solution, as suggested by [14], is to produce ethanol by hydrogenation of the

acetic acid. This solution however requires an external source of hydrogen and the extraction of the acetate. Another solution, analyzed in this thesis, is to esterify these acids with ethanol and/or glycerol. Here, the ethanol is either an output from another process or a product obtained by ethanolic cofermentation of adequate low-grade substrates. Because wastes are used as raw materials, the use of ethanol from another source still increases the productivity of this source by adding to its net energy output while using low-grade input. The glycerol considered here is mainly a by-product of the biodiesel production process. This would increase the energy output but also the efficiency of the biodiesel process by giving value to glycerol that often ends in waste streams due to low demand.

The esterification with ethanol mainly produces ethyl esters : ethyl acetate (EtAc; $C_4H_8O_2$), ethyl propionate (EtPr; $C_5H_{10}O_2$) and ethyl butyrate (EtBu; $C_6H_{12}O_2$), whereas the esterification with glycerol produces glyceryl esters : mono-, di- and triacetin ($C_5H_{10}O_4$, $C_7H_{12}O_5$ and $C_9H_{14}O_6$), mono-, di- and tripropionin ($C_6H_{12}O_4$, $C_9H_{16}O_5$ and $C_{12}H_{20}O_6$), and mono-, di- and tributyrin ($C_7H_{14}O_4$, $C_{11}H_{20}O_5$ and $C_{15}H_{26}O_6$). The molecular structure of all major esters are illustrated in Appendix A.

As far as we know, engine experiments on these products have not been reported. In this thesis, we have investigated the three ethyl esters which are the fundamental building blocks of the other molecules. The main properties of the ethyl esters are given in Table 1.1.

Compared with iso-octane, the lower heating values (LHV) of the esters are significantly smaller. However, because their stoichiometric air-fuel ratio (AFR_{stoich}) is also significantly smaller, this only results in loss of energy content for a given mass or volume of fuel but not a loss of power for the engine since the energy content of the stoichiometric air-fuel mixtures are similar. The ignition points (or autoignition temperatures measured with the procedure described in the ASTM E659[2])

[2]In the ASTM E659 procedure, a 500-mL flask is heated in a furnace that maintains uniform temperature. Samples of the fuel are injected in the flask containing air at a given temperature. The autoignition point is the lowest temperature at which the mixture exhibits flames within 10 minutes.

Table 1.1: Fuel characteristics

	EtAc $C_4H_8O_2$	EtPr $C_5H_{10}O_2$	EtBu $C_6H_{12}O_2$	Ethanol C_2H_6O	Iso-octane C_8H_{18}
AFR_{stoich}	7.85	8.8	9.52	9.00	15.13
Density [kg/l]	0.897	0.891	0.886	0.789	0.690
LHV [MJ/kg]	23.79	26.53	28.64	27.75	44.65
LHV [MJ/l]	21.34	23.64	25.38	21.89	30.81
Ignition [°C]	460	440	463	362	396
Flash point [°C]	-4	12	26	12	-7
Boiling T @1 atm. [°C]	77	99	120	78	98
Vapour p @20°C [hPa]	124	58	17	79	54
Δh_{vap} @25°C [kJ/kg]	404	368	367	837	309
Mm [kg/kmol]	88	102	116	46	114
Stoich. energy content [kJ/kg_{mix}]	2689	2707	2741	2774	2768
Process production range [$\%_{vol}$]	15–87	5–50	7–78		

are not obtained in engine conditions but they still give some information on the level of ignitability. This temperature is similar among the esters and higher than ethanol and iso-octane, indicating that these products are more resistant to ignition. The analyses in engine conditions, presented in Chapters 2 and 3, confirmed the first indication given by the ignition points and helped to identify the difference within the esters. Compared with two known references, iso-octane and ethanol, the flash point, the boiling temperature at atmospheric pressure and the vapour pressure at 20°C are similar for all fuels, except for ethyl butyrate with a slightly higher boiling temperature and a lower vapour pressure. The energies of vaporization of the esters are in the same range as iso-octane but significantly lower than ethanol. This aspect facilitates the mixture preparation and alleviates the cold start problem of HCCI engines.

We have performed preliminary tests in a SI engine using EtAc [15]. These experiments have shown that the engine can be run on pure EtAc but requires a slightly higher spark advance to match the gasoline pressure trace.

The proportions of each volatile fatty acid vary with the fermenta-

tion conditions and the type of biomass. The maximum volume fraction of propionic acid is generally lower than acetic acid and butyric acid due to the competition between butyrate type fermentation and propionate type fermentation [13]. The production ranges reported in Table 1.1 aggregate the results of several studies [10–13]. Besides the extraction from the fermentation broth, these production ranges are obtained without further separation processes to concentrate specific products. Therefore, the tested blends of esters are preferably located in the region shown in Figure 1.3.

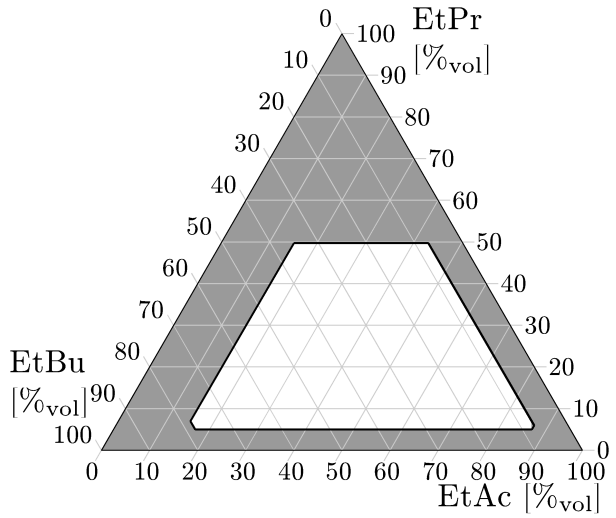

Figure 1.3: Region of fuel blends that could be produced by the biochemical process after a non-selective extraction. The proportion of EtPr is limited by the competition between the butyrate type fermentation and the propionate type fermentation.

While trying to increase the conversion efficiency, the challenge for the overall production process is to handle the diversity of the raw materials and of the resulting fuels so that they can be used as transportation fuels.

1.4 Combustion kinetics in HCCI engines

This section presents the main reaction steps of the combustion in HCCI engines. More details can be found in [6, 16]. The fuel chemistry plays a key role in the onset of this combustion. Therefore, a basic understanding of the involved phenomena is important.

The combustion of hydrocarbon fuels typically involves a chain reaction mechanism where the fuel is converted into products (H_2O and CO_2), and where heat is released.

To describe this chain reaction mechanism, elementary reactions are grouped into four general classes: initiation, propagation, chain branching and termination. Initiation reactions produce radicals from stable species. Their rates of reaction are small and they have a minor contribution to the overall reaction rate but the produced radicals play a major role in the first steps of the chain reaction. Propagation reactions produce and consume the same number of radicals. They do not directly contribute to the reactivity of the system but to the continuation of the chain reaction. Chain branching reactions produce more radicals than they consume. They are the major source of radicals and initiate the exponential growth of reactivity during the main combustion event. Termination reactions reduce the concentration of radicals by recombination of two radicals into a stable species and therefore reduce the reactivity.

During the compression stroke, as the temperature increases, the air-fuel mixture proceeds through three distinct kinetic steps : low (below 800 K), intermediate (800 to 1000 K) and high (above 1000 K) temperature chain branching.

1.4.1 Low temperature combustion

When the temperature reaches 550 K, the first initiation steps start producing a small amount of radicals. They involve decomposition reactions

$$\mathrm{RH} \rightarrow \mathrm{R'}\bullet + \mathrm{R''}\bullet \,, \tag{1.4}$$

or bimolecular reactions

$$RH + O_2 \rightarrow R\bullet + HO_2\bullet \ , \tag{1.5}$$

where the fuel (RH) is considered as an alkane, "•" indicates a radical, R• is the corresponding alkyl radical, R′• and R″• are smaller radical species[3], and HO_2• is the hydroperoxyl radical.

Then, R• primarily adds to O_2 to produce alkylperoxyl radicals (RO_2•):

$$R\bullet + O_2 \rightleftarrows RO_2\bullet. \tag{1.6}$$

This reaction is reversible and rapidly reaches dynamic equilibrium during the compression stroke. It is very sensitive to both temperature and pressure, shifting to the R• + O_2 side when temperature increases and to the RO_2• side when pressure increases. The production of RO_2• controls the start of a possible chain branching at low temperature, as developed below. When the temperature reaches the range 700-850 K, its effect on the reaction exceeds the effect of the pressure, hence the backward reaction becomes faster, which thereby decreases the concentration of RO_2• and the chain branching activity. This is the negative temperature coefficient (NTC) of reaction, where the reactivity of the system counterintuitively decreases when the temperature increases.

To better understand the NTC and the conditions for low temperature chain branching, the next reaction steps of RO_2• have to be analyzed.

First, a H atom is transferred from a location within RO_2• to the end of the attached O_2 to produce hydroperoxyalkyl radicals •QOOH:

$$RO_2\bullet \rightleftarrows \bullet QOOH \ . \tag{1.7}$$

The •QOOH species then proceeds through four distinct propagation reactions depending on its structure and its size:

[3]The generic notation illustrates the diversity of the radicals produced by these reactions. For example, n-heptane may decompose in $C_7H_{16} \rightarrow \bullet C_3H_7 + \bullet C_4H_9$.

$$\bullet\mathrm{QOOH} \rightarrow \mathrm{Q} + \mathrm{HO_2}\bullet \,, \tag{1.8}$$

$$\bullet\mathrm{QOOH} \rightarrow \mathrm{Q'} + \mathrm{QO} + \bullet\mathrm{OH} \,, \tag{1.9}$$

$$\bullet\mathrm{QOOH} \rightarrow \mathrm{Q'O} + \bullet\mathrm{OH} \,, \tag{1.10}$$

$$\bullet\mathrm{QOOH} + \mathrm{O_2} \rightleftarrows \bullet\mathrm{O_2QOOH} \,, \tag{1.11}$$

where •OH is the hydroxyl radical, Q and Q′ are olefins, QO is an aldehyde, Q′O is a cyclic ether and •O_2QOOH is a ketohydroperoxyalkyl radical.

Reaction (1.11) is fundamentally similar to reaction (1.6) and is the only intermediate propagation reaction that can lead to chain branching. It is followed by several elementary reactions, which are summarized by the global reaction:

$$\bullet\mathrm{O_2QOOH} \rightarrow \bullet\mathrm{OPO} + \bullet\mathrm{OH} + \bullet\mathrm{OH} \,, \tag{1.12}$$

where •OPO represents an oxygenated hydrocarbon radical that can have many forms depending on the structure and pathway of •O_2QOOH. Three radicals are produced by this global reaction, their concentration therefore increases and they primarily react with the fuel through H abstraction reactions like:

$$\mathrm{RH} + \mathrm{X}\bullet \rightarrow \mathrm{R}\bullet + \mathrm{XH}, \tag{1.13}$$

where X• is a radical (mainly •OH and HO_2•) and XH a stable product at this temperature.

Low temperature auto-ignition can be produced by the successive reactions (1.6), (1.7), (1.11), and (1.12). However, this low temperature combustion is not observed for every fuels. Some fuels (e.g. gasoline, ethanol, ...) ignite in a single step while others (e.g. diesel, dimethyl ether, ...) proceed through a two-stage ignition, a small amount of heat being released early before the main ignition (see Figure 1.4).

This low temperature pathway thus depends on the fuel type because its structure controls the rate of RO_2• isomerization (1.7), which then

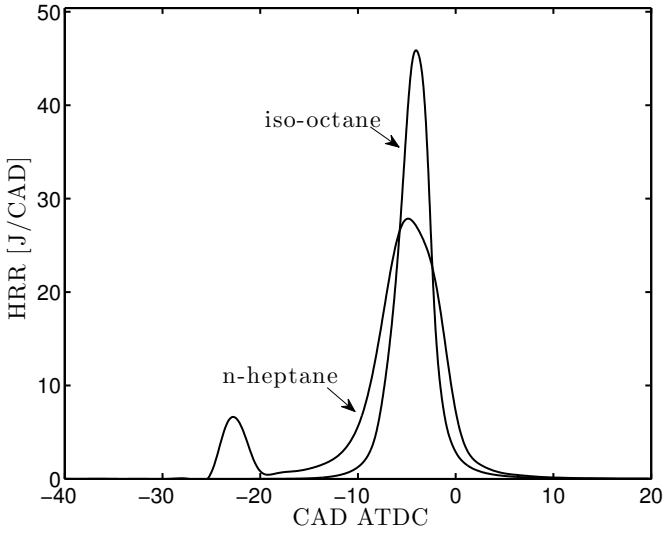

Figure 1.4: Heat release rate (HRR) computed by CFD simulations for a single-stage fuel (iso-octane) and a two-stage fuel (n-heptane) in a HCCI engine. The main combustion timing is similar for both fuel but the inlet temperature for iso-octane is higher than for n-heptane due to the small amount of heat released during the low temperature combustion.

controls the •QOOH reactions.

When the temperature increases above 700-750 K, these reactions shift toward •QOOH and at about 800-850 K, these reactions are stopped. Along with the shift of reaction (1.6), this leads to the reduction of the overall reaction rate and the heating is therefore mostly due to the compression of the piston. The pathway leading to this auto-ignition is summarized in Figure 1.5.

While this low-temperature auto-ignition only provides a small temperature increase (10-20 K), it strongly determines the subsequent main ignition.

1.4.2 Intermediate and high temperature combustion

Above 850 K, reaction (1.6) evolves smoothly to the reaction

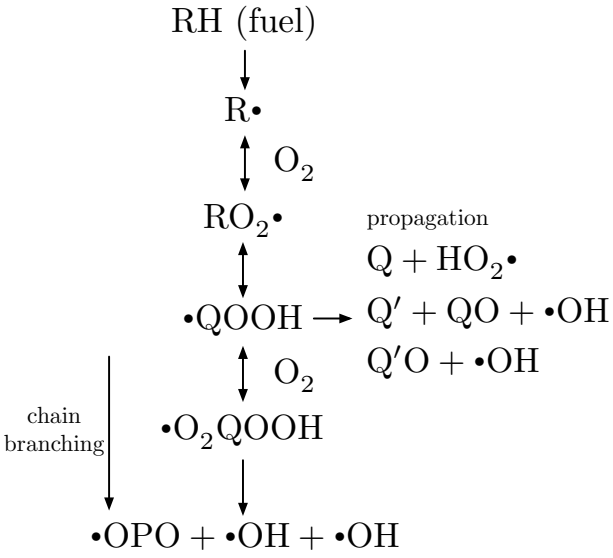

Figure 1.5: The low-temperature auto-ignition characterizes two-stage ignition fuels where a reaction chain leads to a small heat release before the main ignition event [16].

$$R\bullet + O_2 \rightarrow \text{olefin} + HO_2\bullet \ . \tag{1.14}$$

Moreover, the fuel primarily reacts with OH and HO_2 through reaction (1.13), and the recombination reaction of the hydroperoxyl radical becomes important:

$$HO_2\bullet + HO_2\bullet \rightarrow H_2O_2 + O_2 \ . \tag{1.15}$$

These reactions increase the temperature and the concentration of hydrogen peroxyde (H_2O_2). When the temperature reaches 1000 K, the onset of the main auto-ignition event is mainly controlled by the decomposition of H_2O_2 into two •OH radicals :

$$H_2O_2 + M \rightarrow \bullet OH + \bullet OH + M \ , \tag{1.16}$$

where M is any other molecule. For this decomposition reaction to proceed, the energy in H_2O_2 should be sufficient to break the bond. In this case, extra energy is necessary and is provided by collision with M.

The growing concentration of •OH radicals increases the fuel consumption through reaction (1.13), which increases the temperature due to the production of water. This further accelerates the decomposition of H_2O_2, which thereby leads to the exponential growth of the reactivity.

The pressure has a great effect on reaction (1.16) because of the collision with another molecule. When the pressure increases, the critical temperature needed for ignition decreases. Therefore, in HCCI engines, the pressure is also a critical parameter when preparing the air-fuel mixture.

Because the decomposition reaction of H_2O_2 is not related to the fuel but is part of the H_2/O_2 system, the temperature at which auto-ignition is observed is basically fuel-independent. However, as mentioned above, the timing of this event is greatly controlled by the fuel because close to TDC, when the heating due to compression is slower, the possible small increase of temperature induced by the low-temperature chemical reactions allows the mixture to reach the critical temperature significantly sooner.

After the rapid consumption of H_2O_2 and above 1200 K, the high temperature kinetics pathway is mainly dominated by the chain branching reactions

$$\mathrm{H\bullet} + \mathrm{O_2} \rightarrow \mathrm{O\bullet} + \mathrm{\bullet OH}, \tag{1.17}$$

$$\mathrm{O\bullet} + \mathrm{H_2} \rightarrow \mathrm{H\bullet} + \mathrm{\bullet OH}, \tag{1.18}$$

$$\mathrm{O\bullet} + \mathrm{H_2O} \rightarrow \mathrm{\bullet OH} + \mathrm{\bullet OH}. \tag{1.19}$$

Moreover, at high temperatures, the alkyl radicals primarily decompose into smaller species by β-scission (splitting of a C-C bond):

$$\mathrm{R\bullet} \rightarrow \text{olefin} + \mathrm{R'\bullet}\ . \tag{1.20}$$

A significant portion (around 50%) of the fuel heating value is released at high temperature by the CO oxidation. It is mainly consumed through

$$\mathrm{CO} + \mathrm{\bullet OH} \rightarrow \mathrm{CO_2} + \mathrm{H\bullet}\ . \tag{1.21}$$

But the hydroxyl radical (•OH) first reacts with the fuels, through reaction (1.13), which inhibits this reaction until the fuel has been consumed.

While only a few reactions are presented here, the overall oxidation process of typical automotive fuels requires many thousands of coupled elementary reactions involving many hundreds or even thousands of chemical species. The next section describes how to handle this complex network and use it in CFD simulations.

1.5 Combustion chemistry in numerical simulations

To accurately and comprehensively describe the fuel oxidation, detailed chemical reaction mechanisms are developed over wide ranges of system parameters such as pressure, temperature, equivalence ratio and residence time [17]. As the fuel complexity increases, the number of reactions and species grows exponentially. This increase of complexity explains that mechanisms for realistic fuel surrogates are very large. For example, the mechanism for methyl decanoate, a surrogate for biodiesel, includes more than 3000 species (see Figure 1.6).

The progression between Figures 1.7 and 1.8 further illustrates the different level of details embedded in a simplified mechanism (Figure 1.7) and in a detailed mechanism (Figure 1.8) for molecules of similar complexity (n-heptane and iso-octane).

For simulations of the combustion in engines, comprehensive mechanisms allow to describe the combustion of fuels for many operating conditions, the formation of the main pollutant emissions (CO, soot, NO_x and unburned hydrocarbons), and the heat release rate under conventional and innovative combustion modes such as HCCI. When complex chemical mechanisms are included in CFD simulations, the evolution of the chemical species mass fractions in each computational cell is performed by an operator-splitting technique, where the transport term and the source term of the ordinary differential equations (ODE) are solved

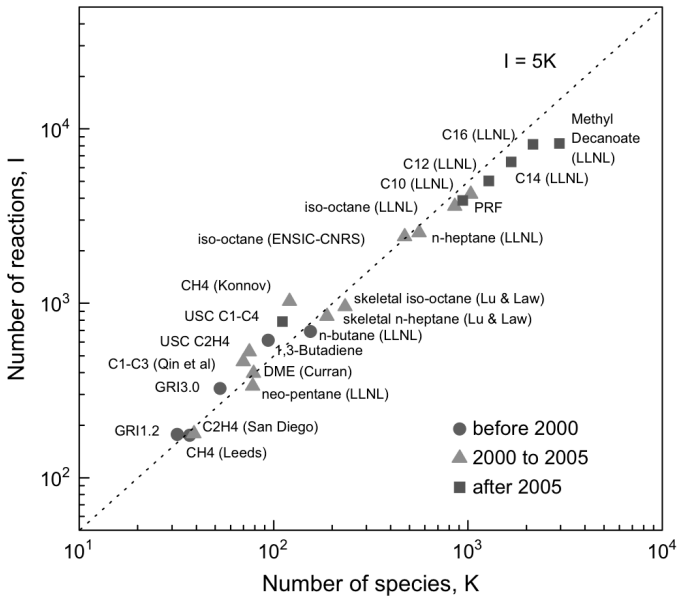

Figure 1.6: As more complex fuel surrogates are modeled, the number of species and reactions grows exponentially. For example, the mechanism for methyl decanoate, a biodiesel surrogate, has more than 3000 species [18].

separately. While the transport term is solved by the CFD solver, a specific ODE solver takes the thermochemical conditions (temperature, pressure and species concentration) and integrates the chemical problem over the time-step [23]. Solving the whole system of nonlinear stiff ODE is particularly demanding of computational resources. Above 40 species, more than 90% of the overall computational time is spent in solving the chemical source terms. This computational time becomes prohibitive, well before reaching the characteristic size of detailed mechanisms. The computational cost typically scales linearly with the number of reactions and quadratically with the number of species. The largest cost savings are therefore achieved by reducing the number of species. Moreover, this also reduces the number of transport equations solved by the CFD solver.

To reduce the computational cost of the combustion chemistry, various techniques have been developed (some of these methods are further

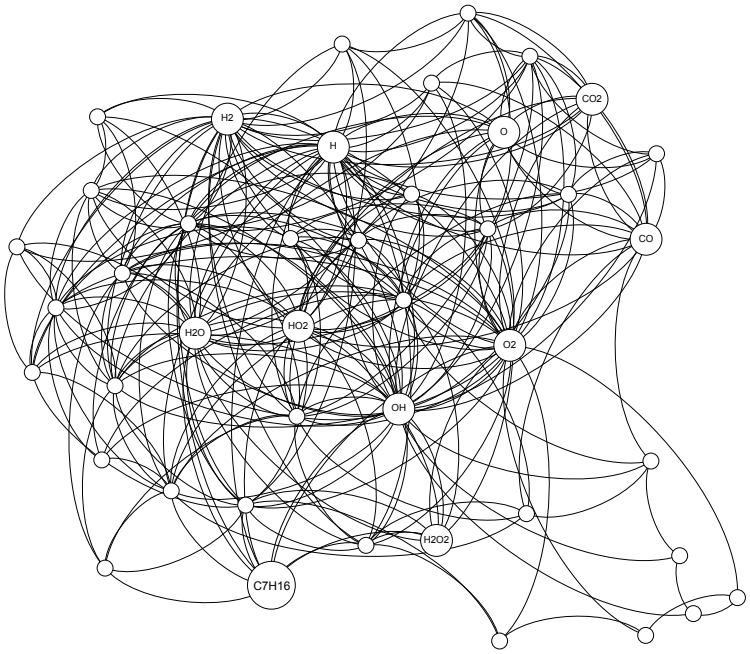

Figure 1.7: Network generated with Gephi [19] using the n-heptane mechanism from Liu et al. (44 species and 112 reactions)[20]

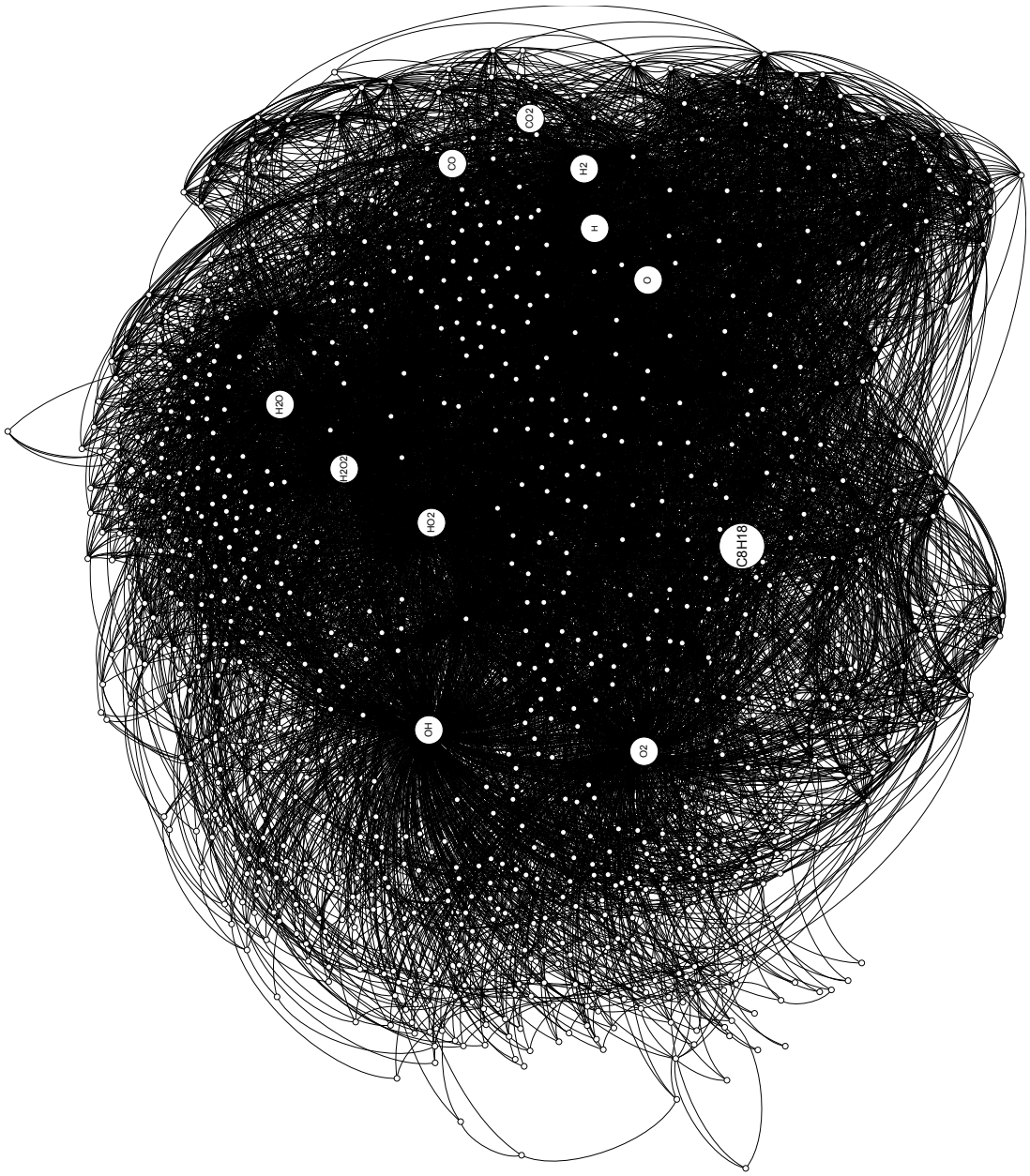

Figure 1.8: Network generated with Gephi [19] using the iso-octane mechanism from LLNL (874 species and 3796 reactions) [21, 22].

detailed in Chapters 5 and 6). Many of these techniques involve a preprocessing step that can be performed at two different levels: the reduction of the dimension of the system or the storage and subsequent retrieval of computed solutions. The first reduces the complexity of the system to be solved while the second reduces (or avoids) the use of the ODE solver during the simulations.

To reduce the size of the mechanism, several methods remove the species and the reactions that have a low connectivity to the phenomena of interest. These methods are based on the definition of the strength of the interactions between species. They remove species that are weakly connected to a set of important species. Examples of this approach based on different measures of the interactions are the directed relation graph (DRG) [17], the DRG with error propagation (DRGEP) [24], the path flux analysis (PFA) [25] and the simulation error minimization (SEM) [26]. The mechanism can also be reduced according to time-scale analysis. In this case, the methods analyze the Jacobian of the system and deduce which species are actively involved in the reactivity. While the results from these techniques are qualitatively better, the computational cost associated with the Jacobian analysis is considerable, when compared to the previous methods. Examples of this strategy are the sensitivity analysis [27], the computational singular perturbation (CSP) [28] and the quasi steady-state assumption [29]. Finally, the reduction can be achieved by lumping several species with similar properties together and solving one ODE for the entire group [30]. Some methods combine several of these techniques to maximize the reduction [18, 31, 32].

The solution storage and retrieval methods mainly consist of tabulated chemical source terms that require extra effort to be computed but are very fast to be retrieved. This can greatly reduce the overall computational time when they are frequently used. In these methods, tables are populated or "trained" with sample data from simplified cases and a mapping variable is devised to retrieve the stored information. The main methods are the look-up tabulation [33], repro-modeling [34], artificial neural network (ANN) [35] and tabulated kinetics for ignition (TKI) [36].

The preprocessing of the mechanism ensures the global comprehen-

siveness based on sample points. When the range of thermochemical conditions is large, like in ICE, the reduced mechanisms need to include more species and the tabulation is more difficult because it needs to include solutions for many different conditions and to map them to one or a few progress variables that make sense throughout the simulation. Therefore, several methods tailor the kinetic mechanism to each computational cell and ensure the local comprehensiveness by processing the mechanism at runtime; examples of these methods are the dynamic adaptive chemistry (DAC) [37] and the element flux analysis (EFA) [38].

Since several cells may be in the same state, multi-grid methods group similar cells and solve them together [39]. Similarly, previously computed results may be adequate for the current cell, therefore the in-situ adaptive tabulation (ISAT) method [40] and the piecewise reusable implementation of solution mapping (PRISM) [41] store previously computed results dynamically and retrieve them according to specific regions of accuracy.

Figure 1.9 illustrates the dynamic tabulation methods and the on-the-fly reduction of chemical mechanisms.

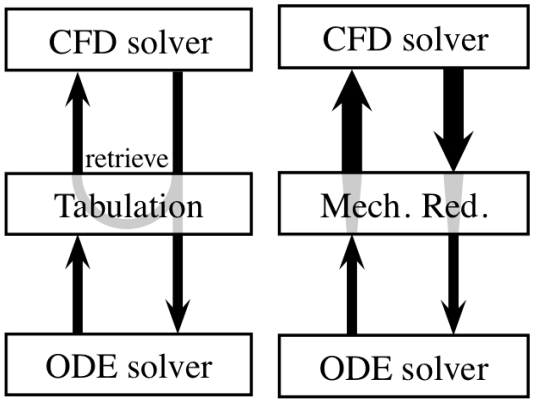

Figure 1.9: The tabulation methods (left) aim at retrieving stored results to avoid using the ODE solver. The mechanism reduction methods (right) aim at reducing the number of species to mitigate the computational cost of the ODE solver

Combining both dimension reduction and tabulation (or multi-grid)

is very effective because of the great synergy existing between these methods. It has been proposed as a preprocessing step with the intrinsic low dimensional manifold (ILDM) [42] further developed in flame prolongation of ILDM (FPI) [43]. It has also been proposed as dynamic methods, for example: ISAT and rate-controlled constrained equilibrium [44] or adaptive multi-grid chemistry and DAC (AMC-EDAC) [45]. The TDAC method, that has been developed in this thesis, consists of such a dynamic coupling. Its first implementation couples the DAC and ISAT methods (see Chapter 5). Further analysis of the reduction methods within this framework are also presented in Chapter 6.

The reduction techniques, used in engine CFD simulations and reported in the literature, reach speed-up around 50 using detailed mechanisms and complex geometries.

CHAPTER 2

Experimental investigation of ethyl acetate, ethyl propionate and ethyl butyrate in HCCI

This chapter is an updated version of the paper published in :
F. Contino, F. Foucher, C. Mounaïm-Rousselle, and H. Jeanmart. Experimental characterization of ethyl acetate, ethyl propionate, and ethyl butanoate in a homogeneous charge compression ignition engine. *Energy & Fuels*, 25(3):998–1003, 2011. doi: 10.1021/ef101602q

2.1 Introduction

The production of biofuels is constrained by the specific fuel characteristics required for spark ignition (SI) and compression ignition (CI) engines. Therefore, a great part of the biomass energy content is lost in the successive conversions steps, hence decreasing the overall energy balance, e.g. the production of ethanol from corn, sugar beet or wheat consume up to 85% of the ethanol energy output [46, 47].

The Homogeneous Charge Compression Ignition (HCCI) engine not only offers a great potential of efficiency improvement and emissions reduction (i.e. NO_x and soot) [3, 4, 48, 49] but it can also be run on any type of fuels given that the appropriate operating conditions are chosen [7, 50–52].

This flexibility allows the use of low-grade fuels as transportation fuels. It gives an opportunity to develop more simple and more efficient bioconversion processes, as illustrated by Mack et al. with the use of wet-ethanol [8].

Products resulting from acidogenic fermentation (acidogenesis) will be further discussed in this chapter. Acidogenesis is a natural step occurring when organic substrates degrade under anaerobic conditions. It can be exploited to convert biomass and biowastes to volatile fatty acids (including acetic, propionic, butyric). It has three main advantages compared to ethanol fermentation [9, 53]: source diversification, efficiency and easy implementation. Indeed, it can not only use sugar but also a wide range of fermentable organic substrates, including biowastes. Less treatment to hydrolyze biomass is required because acidogenic bacteria have a wide hydrolytic capacity while yeast does not. Moreover, acidogenic fermentation does not require a germ free environment.

Although the volatile fatty acids could be directly used in an engine, it is generally not considered due to materials resistance. Therefore, they can be partly combined with ethanol (produced during the first stages of the acidogenic fermentation) and the remaining part can be combined with glycerol, offering a market for this by-product of the biodiesel production [54–56]. This process leads to a large range of esters from ethyl acetate ($C_4H_8O_2$) to tributyrin ($C_{15}H_{26}O_6$).

Alternative fuels are an opportunity to widen the HCCI zone, i.e. the range of loads and speeds where HCCI combustion is possible [6]. The heat released is mainly controlled by the ignition timing and the combustion duration. It is, therefore, important to understand how these parameters are related to the particular fuel properties. We have studied numerically the HCCI running zone using ethyl acetate [57] (see also Chapter 4). Ethyl acetate has a running area similar to iso-octane but it is shifted towards upper loads. This indicates that ethyl acetate is more resistant to ignition than iso-octane.

In this chapter, three of the esters derived from acidogenesis are analyzed experimentally on a HCCI engine : ethyl acetate (EtAc), ethyl propionate (EtPr) and ethyl butyrate (EtBu). The objective is to understand their behavior under HCCI conditions. These results will also be used in Chapter 3 to characterize blends of these products and will suggest how to adjust the fermentation toward the optimal fuel blend composition.

Combustion of EtAc, EtPr and EtBu have already been investigated

in the context of biodiesel characterization [58–61]. These studies focused on a better understanding of the mechanism of oxygenates combustion to extend it to biodiesel, mainly composed of long chain fatty esters. EtAc combustion has also been studied in the context of thermal oxidizers for reducing the pollution of volatile organic compounds [62].

This chapter first describes the experimental setup. It then presents the results of the experiments for the three esters taking ethanol (EtOH) as the reference fuel. Finally, it discusses how the combustion characteristics alter the HCCI operating zone.

2.2 Experimental setup

2.2.1 Fuels characteristics

The fuels used in the experiments are esters resulting from the reaction of volatile fatty acids (acetic, propionic and butyric acids) with ethanol. Their properties are summarized in Table 2.1.

The three esters have similar ignition points (or autoignition temperature measured with the procedure described in the ASTM E659 and given in the material safety data sheet), around 450°C, which is 90°C above ethanol. Even if the method to determine this temperature is different from the HCCI conditions, it indicates that ethanol should ignite more rapidly. Moreover, among the esters, even if the ignition points are not significantly different, EtBu has probably a shorter ignition delay because of its longer chain.

The lower heating value (LHV) of all four fuels are significantly smaller than petroleum-based fuels due to their oxygenated nature. However, the air-fuel ratio of the stoichiometric mixtures (AFR_{stoich}) are also smaller, which results in similar energy content for the same equivalence ratio and therefore no loss of power for the engine.

The esters have an energy of vaporization that is significantly lower than that of ethanol and only slightly higher than those of gasoline and diesel. This would have a positive impact for the mixture preparation on a real engine. In the following experiments, the vaporization energy is,

Table 2.1: Fuel characteristics

	EtAc $C_4H_8O_2$	EtPr $C_5H_{10}O_2$	EtBu $C_6H_{12}O_2$	EtOH C_2H_6O
AFR_{stoich}	7.85	8.8	9.52	9.00
Density [kg/l]	0.897	0.891	0.886	0.789
LHV [MJ/kg]	23.79	26.53	28.64	27.75
LHV [MJ/l]	21.34	23.64	25.38	21.89
Ignition [°C]	460	440	463	362
Flash point [°C]	-4	12	26	12
Boiling temp. @1 atm. [°C]	77	99	120	78
Vapour pres. @20°C [hPa]	124	58	17	79
Δh_{vap} @25°C [kJ/kg]	404	368	367	837
Mm [kg/kmol]	88.1	102	116	46.1
Stoich. energy content [$kJ/kg_{mixture}$]	2689	2707	2741	2774

however, not relevant because the air-fuel mixture is prepared externally in a fuel vaporizer (see next section).

2.2.2 Engine details and data acquisition

The engine is based on the PSA DW10 model that has a displacement of 0.499 liters per cylinder. It is converted to single-cylinder operation and mounted on an electric motor that can maintain a constant revolution speed. The geometric compression ratio is 15.35 and the effective compression ratio, evaluated thermodynamically using the temperature-entropy diagram with the method described by Tazerout et al. [63], is 14.15. The specifications of the engine are listed in Table 2.2 and a schematic of the experimental setup is shown in Figure 2.1.

The intake air is supplied by an air compressor. It is dehumidified to a dew point of 4°C and electrically heated to the desired set point. Its flow rate is metered and controlled by a Brooks 5853S model to obtain

Table 2.2: Engine details

Bore [mm]	85
Stroke [mm]	88
Displacement [cm^3/cyl.]	499
Connecting rod length [mm]	145
Geometric Compression ratio	15.35
Effective Compression ratio [63]	14.15
Number of valves	4

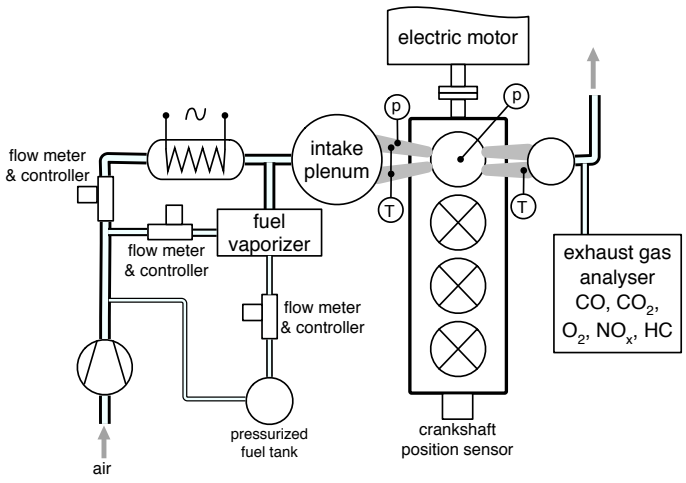

Figure 2.1: The engine is a PSA DW10 with a displacement of 499 cm^3/cyl converted to single-cylinder.

an intake pressure of 1.5 bar in the intake plenum.

The fuel flow from the pressurized tank is metered and controlled by a Bronkhorst M13 Coriolis flow sensor. Fuel is fully premixed with the intake air by supplying an air-fuel mixture from the heated fuel-vaporization chamber upstream of the intake plenum. This plenum is designed to minimize the pressure oscillations and to improve the mixture homogeneity.

The intake conditions are measured in the intake manifold by a Kistler 4075A piezoresistive absolute pressure sensor (±3 kPa) and by two K thermocouples (±2 K) in both intake ducts just above the inlet valves.

Cylinder pressure measurements are made with a Kistler 6043A piezoelectric transducer (±2% of the measured value) at 0.1 crank angle degrees (CAD) increments. The piezoelectric transducer offset is determined by the mean value of the absolute pressure in the intake manifold at the end of the intake stroke when the pressure is stabilized.

The temperatures of the cooling water and the lubricating oil were held constant during the experiments at a value of 93°C and 90°C respectively.

The emissions are measured by an Environnement S.A. exhaust gas analyzer. The overall precision is 1% of the full scale output (FSO). This analyzer is made up of the Topaze 32M model for NO_x measurements (FSO: 1%), the Graphite 52M (based on a FID) model for unburnt hydrocarbon (uHC, FSO: 1%) and CH_4 measurements (FSO: 1000ppm), and the Mir2M model for CO (separated high and low range, FSO: 10% and 2000ppm), CO_2 and O_2 (FSO : 25%) measurements.

2.2.3 Experimental procedure

As the main objective is to understand the behavior of each fuel and apply these results in future studies to characterize a fuel blend, the tested fuels are compared at the same intake conditions. The temperature at the heater output was set to 270°C and the pressure in the intake plenum at 1.5 bar. The operating regions were therefore not optimized for each fuel but the focus is on the impact of each fuel on the operating

zone. Due to heat transfer after the heater and mixing with the fuel (fuel vaporizer at 170°C), the temperature in the intake manifold decreases to around 230°C.

Two engine speeds have been investigated: 1000 and 1500 rpm. Due to small differences in heat transfer after the heater, the temperatures in the intake manifold were 230°C and 235°C at 1000 and 1500 rpm, respectively. Higher engine speeds were not used because the current engine setup was not able to provide the high fuel flow due to the low AFR of the ethyl esters.

Pressure data from 100 consecutive cycles were stored and analyzed by the data acquisition system when combustion was stabilized. A Buttleworth low pass band filter [64] is used to remove the high frequency noise. Among the parameters calculated on each cycle were: the maximum pressure (P_{max}), the crank angle at which P_{max} occured, the maximum pressure rise rate (MPRR) and the indicated mean effective pressure (IMEP). The mean values and standard deviations of these parameters based on 100 cycles were calculated online and used to determine stabilization and operating limits. These values were also used to compute the coefficient of variation of IMEP (CoV_{IMEP}), given by the standard deviation of IMEP divided by its mean.

We adjusted the fuel injection to modify the equivalence ratio until we went past one of the HCCI limits. These limits were defined for this work as a maximum MPRR of 7 bar/CAD for the upper or knock limit and a maximum CoV_{IMEP} of 5% for the lower or misfire limit.

The reported temperatures are averaged for the total mass inside the combustion chamber. They are computed using the ideal gas law with the measured pressure, the known cylinder volume and the temperature at bottom dead center (T_{BDC}). Several effects should be considered when computing T_{BDC}: mixing with residual exhaust gas, heat-transfer, gas dynamic effects and vaporization of directly injected liquid fuel [65]. However, the trapped residual exhaust gas was small due to the pressurized inlet and the atmospheric exhaust; the air-fuel mixture was prepared externally without any vaporization in the cylinder; and the gas dynamic effects were not considered since the two investigated engine speeds were small and close to each other. Therefore, we consid-

ered that T_{BDC} was equal to the temperature measured just before the inlet valves. This is a good approximation when comparing the fuels on the same engine with the same settings.

The heat release rate (HRR) was computed from the cylinder-pressure data and the cylinder volume:

$$\frac{dQ}{d\theta} = \frac{C_p}{R} p \frac{dV}{d\theta} + \frac{C_V}{R} V \frac{dp}{d\theta} + \frac{dQ_{\text{wall}}}{d\theta} \ , \tag{2.1}$$

where θ is the crank angle, C_p and C_V are the specific heats at constant pressure and constant volume respectively, R is the ideal gas constant, p is the pressure, V is the volume of the combustion chamber and $\frac{dQ_{\text{wall}}}{d\theta}$ is the wall heat release rate per crank angle. $\frac{dQ_{\text{wall}}}{d\theta}$ is given by

$$\frac{dQ_{\text{wall}}}{d\theta} = h_g \left[A_{\text{h}}(T - T_{\text{h}}) + A_{\text{p}}(T - T_{\text{p}}) + A_{\text{l}}(T - T_{\text{l}}) \right] \ , \tag{2.2}$$

where A is the wall surface, T is the temperature, h, p and l subscripts indicate head, piston, and liner, respectively, and h_g is the heat transfer coefficient. This coefficient is given by the Hohenberg correlation [66]:

$$h_g = \alpha_s V^{-0.06} p^{0.8} T^{-0.4} (\bar{s}_p + b)^{0.8} \tag{2.3}$$

where α_s and b are parameters evaluated by Hohenberg at 130 and 1.4, and $\bar{s}_p$ is the mean piston velocity. This correlation gives better results for HCCI engines than the Woschni correlation [67] because it does not include the term representing the combustion compression velocity required for SI engines but which overestimates the heat transfer rates during combustion and expansion for HCCI [68].

The specific heats were computed from the JANAF tables and include the change of composition due to the combustion with a two steps algorithm. First, they are arbitrarily modified at top dead center (TDC) from the composition of the air-fuel mixture to the composition of the complete combustion products. The cumulative heat release is then computed from the HRR obtained with Eq. (2.1). As this change of specific heats is arbitrary, a second step uses the cumulative heat release normalized by its maximum as a conversion factor between reactants and

products and a better approximation of the heat release rate is obtained.

To characterize the combustion, three parameters were calculated for each cycle: CA10, CA50 and CA90. They correspond to the crank angles where 10, 50 and 90% of the cumulative heat release was reached respectively. CA10 is a good indicator of the combustion start for single-stage fuels, as in this work. CA50 is often used to monitor the combustion and adjust the inlet conditions. The difference between CA90 and CA10 defines the combustion duration. The uncertainties on these parameters come from the uncertainty on HRR, which results from the precision of the pressure sensor, the error on the effective compression ratio and the assumptions of the heat transfer model. According to the slope of the cumulative heat released which increases with increasing equivalence ratio, the uncertainties have been evaluated between ± 1 CAD for an equivalence ratio of 0.08 and ± 0.2 CAD for an equivalence ratio of 0.4.

2.3 Results

This section first compares the impact of the combustion characteristics on the operating ranges of EtAc, EtPr, EtBu, and EtOH. It then presents the emissions and finally analyzes the ignition delays of these products.

2.3.1 Operating zone

As discussed in the previous section, the inlet conditions were kept constant. They were chosen so that most of the CA50 are in the narrow range where an HCCI engine can be operated [69]: -5 to 10 CAD ATDC as shown in Figure 2.2. In this figure, CA50 of EtAc at 1500 rpm and equivalence ratios 0.34 and 0.38 are above the other points due to a slightly lower inlet temperature (230°C instead of 235°C for the other points).

Under these conditions, the fuels exhibit quite different combustion characteristics (see Figure 2.3). These differences have a great impact

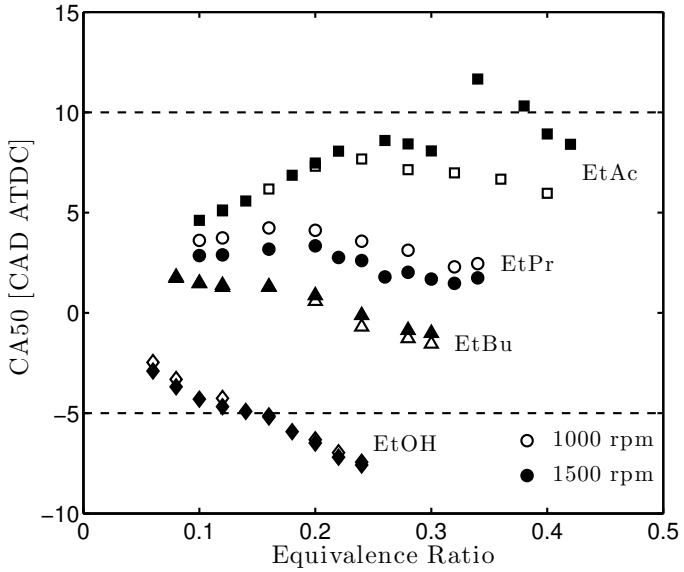

Figure 2.2: CA50 for the four fuels at 1000 rpm (empty symbols) and 1500 rpm (filled symbols). CA50 of EtAc at 1500 rpm and equivalence ratios 0.34 and 0.38 are above the other points due to a slightly lower inlet temperature

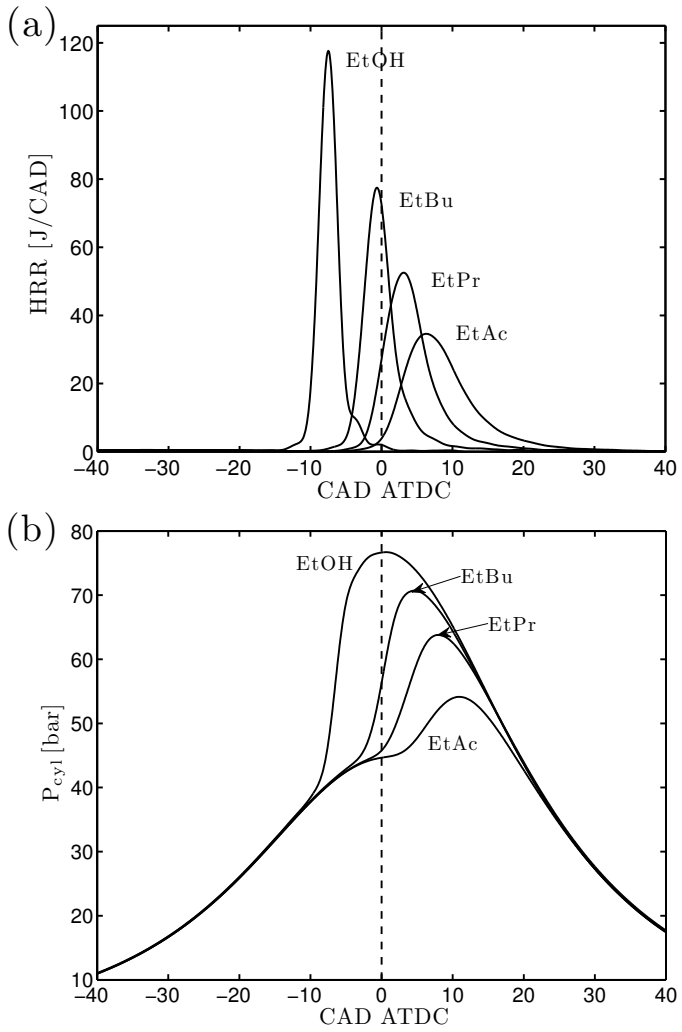

Figure 2.3: Heat release rate (a) and pressure traces (b) for the four fuels at 1000 rpm and at an equivalence ratio of 0.24.

on the operating zones (see Figure 2.4; the higher HCCI zone for EtAc at 1500 rpm is explained by the slightly lower inlet temperature, as mentioned above). EtOH ignites well before TDC and leads to very high MPRR at equivalence ratios above 0.20. EtAc ignites much later bringing issues for the instability at equivalence ratios below 0.20. EtPr ignites later than EtBu but both are in the region where a large range of equivalence ratios can be used without reaching a HCCI limit. Due to the early ignition of EtOH, the combustion is very stable reaching the lower limit at a very low equivalence ratio below 0.08. But the MPRR is increasing quickly with the equivalence ratio, reaching the upper limit at a IMEP around 3 bar. EtBu ignites more slowly which increases the upper limit but without changing the instability limit. For these settings, EtPr has a high upper limit around 5 bar while keeping a similar lower limit. The late ignition of EtAc leads to a smoother pressure rise rate. Consequently, the upper limit is around 6.5 bar. However, this also leads to more instability which increases the lower limit at around 2 bar.

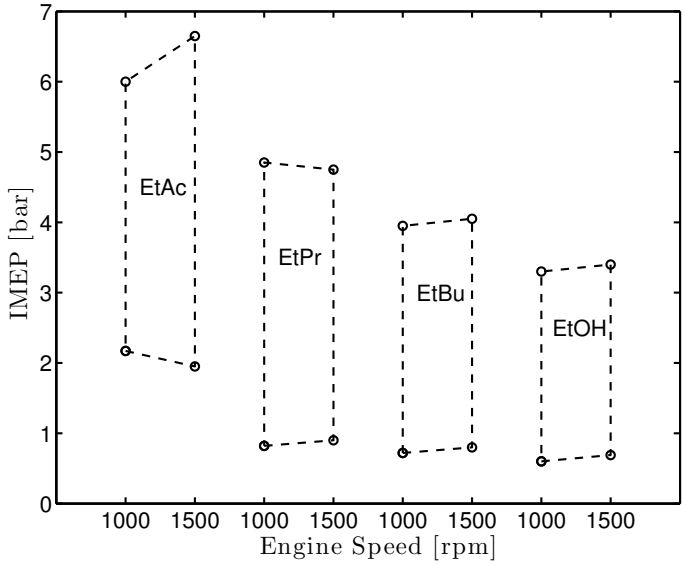

Figure 2.4: HCCI zones for the four fuels.

When reaching the misfire limit, the combustion is unstable and

products of incomplete combustion increase. The CO and uHC emissions are thus related to the position in the HCCI zone. They significantly increase with decreasing IMEP and reach a plateau near the misfire limit (see Figure 2.5). The results reported in Figure 2.5b only illustrate the comparative trends. The absolute value should not be considered here because : first, the uHC were measured with a flame ionization detector (FID) which is not completely suitable for oxygenated fuels; second, the high pressure difference between the intake (1.5 bar) and the exhaust (atmospheric) implies that part of the fuel directly escapes the combustion chamber during valve overlap.

The NO_x emissions correspond to the very low levels commonly obtained in HCCI engines [6], with a peak around 50 ppm for the highest IMEP achieved with EtAc.

2.3.2 Ignition delay and combustion duration

The products tested are single-stage fuels (see Figure 2.3). The difference of combustion characteristics is, therefore, mainly due to different ignition delays. These ignition delays were characterized by the CA10 computed for each cycle (see Figure 2.6). In the specified conditions, EtOH had the shortest ignition delay followed by EtBu, EtPr and EtAc.

The difference of ignition delay is not only due to the intrinsic ignition kinetics but also to the different temperature histories. These two effects are combined and both contribute to the difference between the fuels. The different ignition kinetics are due to the different reaction paths, whereas the temperature histories are modified by the ratio of specific heat of the air-fuel mixtures. For the same equivalence ratio, the ratio of specific heats is higher for EtOH and smaller for EtAc. As the inlet conditions were held constant, overall this leads to higher temperatures before ignition for EtOH and smaller for EtAc (see the temperature at 15 CAD BTDC in Figure 2.7; the experimental variations of the inlet conditions are included).

The effects of the reaction paths and the specific heats are also illus-

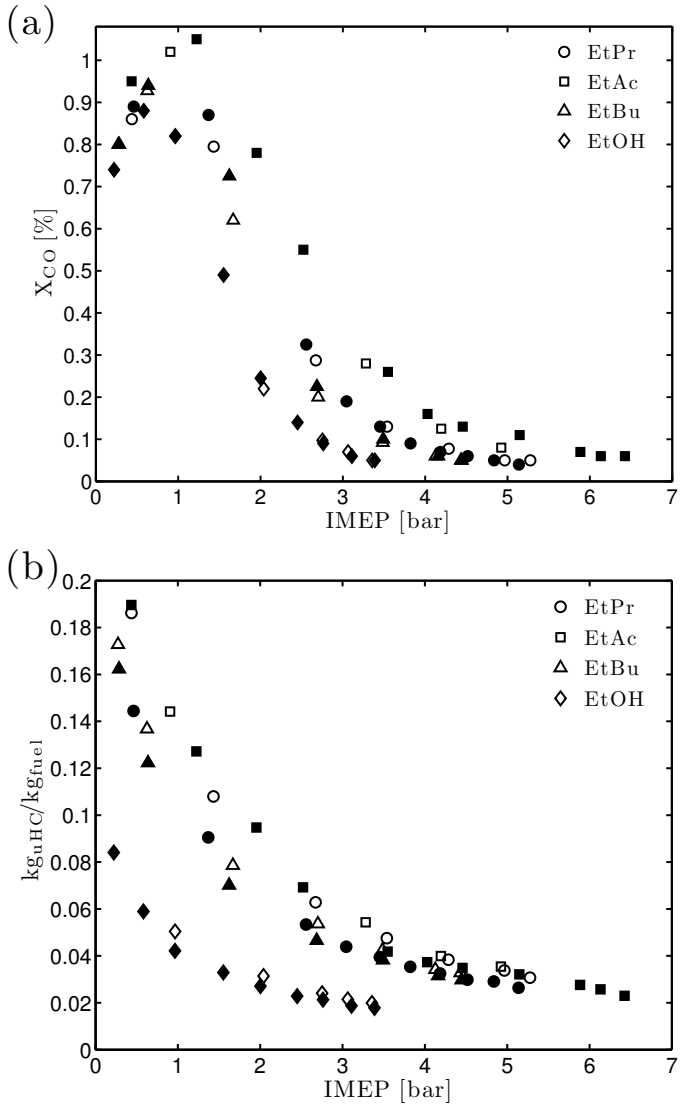

Figure 2.5: CO (a) and uHC (b) emissions for the fours fuels at 1000 rpm (empty symbols) and 1500 rpm (filled symbols).

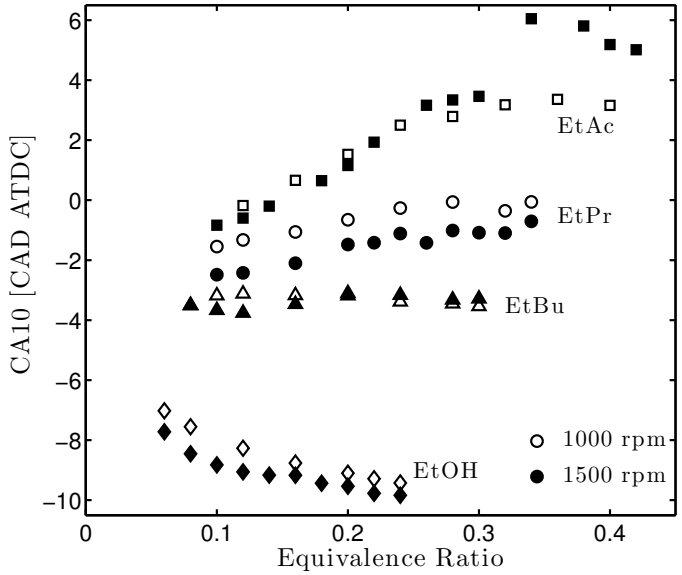

Figure 2.6: CA10 is used to estimate the ignition timing for the four fuels at 1000 rpm (empty symbols) and 1500 rpm (filled symbols).

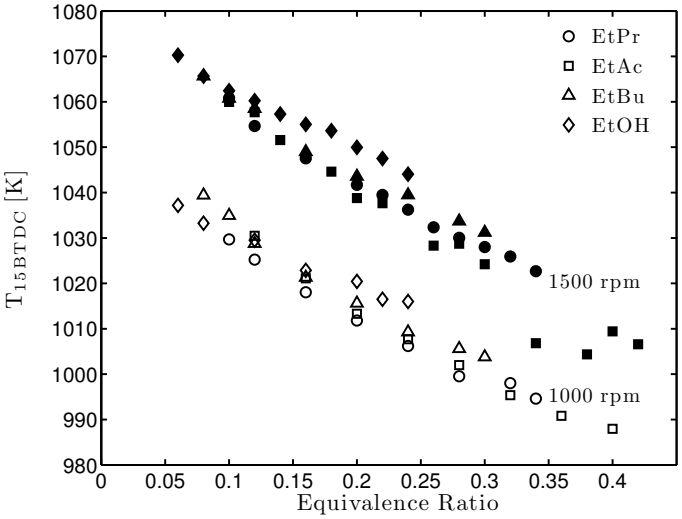

Figure 2.7: Mass-averaged temperature before ignition, here at 15 CAD BTDC for the four fuels at 1000 rpm (empty symbols) and 1500 rpm (filled symbols).

trated by the small change of ignition delay (or CA10) with equivalence ratio (see Figure 2.6). At low temperatures (below 1000 K) the alkylperoxyl radical isomerization reactions (see Reaction 1.7) control ignition and are faster for rich mixtures. Therefore for the same temperature, the ignition delay should decrease with increasing equivalence ratio. However, with more fuel in the mixture, the specific heats increase which reduce the ratio of specific heats and the resulting temperature before TDC (see Figure 2.7). In this case, the thermal effect balances the kinetics effect.

To isolate the thermal effect, we ran ignition delay simulations using the Cosilab software [70]. We used the ethanol mechanism developed by Saxena and Williams [71], the ethyl acetate mechanism of Gasnot et al. [62], the ethyl propionate mechanism of Metcalfe et al. [60] and the ethyl butyrate mechanism of Hakka et al. [61]. The ignition delay was computationally defined as the time before the maximum temperature rise rate in an adiabatic vessel with constant volume.

The simulations results confirm that for the same temperature (the temperature at 15 CAD BTDC for the lowest equivalence ratio of each fuel, see Figure 2.7), the ignition delay decreases with increasing equivalence ratio (see empty symbols in Figure 2.8). However, if the temperature is modified for each equivalence ratio according to the mass averaged temperature at 15 CAD BTDC (see Figure 2.7), the thermal effect balances the kinetics effect and the ignition delay remains approximately constant (see filled symbols in Figure 2.8).

The combustion durations are quite similar and constant for all fuels at low equivalence ratio (see Figure 2.9). They are around 13 CAD for equivalence ratios below 0.15. Above this value, they decrease to reach 5 CAD. For a given equivalence ratio, EtOH has the smallest duration and EtAc the longest. This smoothes the pressure rise rate of EtAc and explains the higher knock limit. The CA50 shown in Figure 2.2 are explained by the combined effects of the ignition delays and the combustion durations.

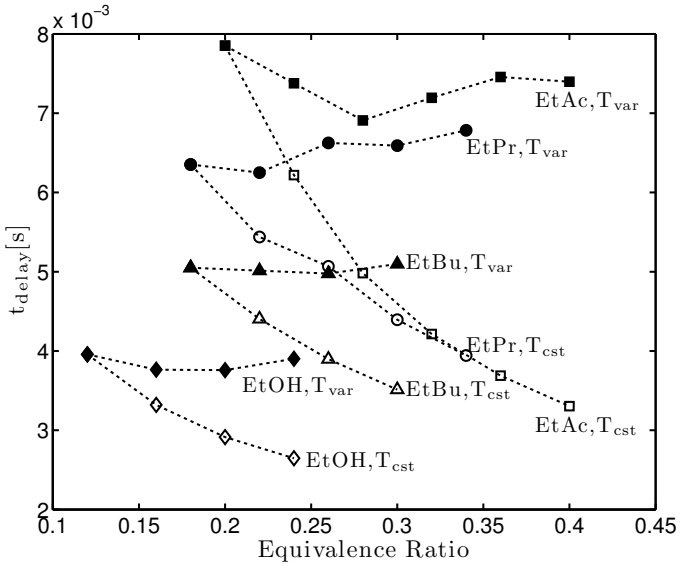

Figure 2.8: Ignition delays for temperatures not modified (empty symbols) or modified (filled symbols) with equivalence ratios and based on the computed mass-averaged temperature at 15 CAD BTDC.

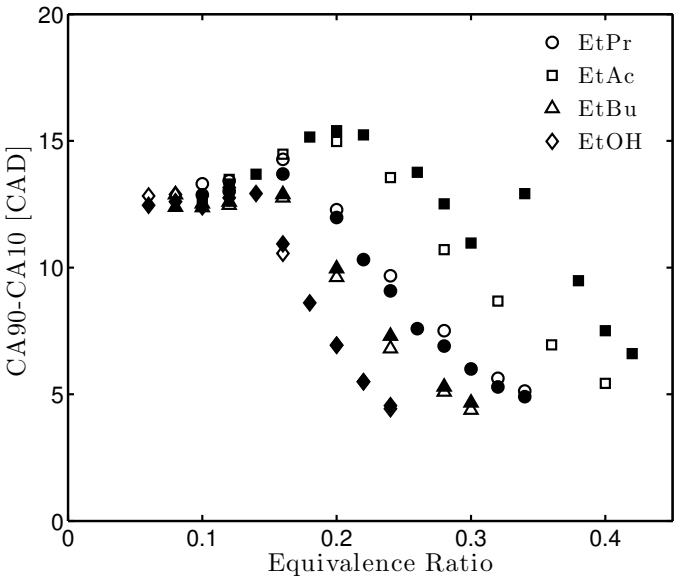

Figure 2.9: Combustion duration, calculated by CA90−CA10 for all fuels at 1000 rpm (empty symbols) and 1500 rpm (filled symbols).

2.4 Conclusion

Ethyl acetate, ethyl propionate and ethyl butyrate (products derived from acidogenic fermentation) can be used in a HCCI engine. They produce stable and smooth HCCI combustion for a large range of equivalence ratios. Compared with ethanol, these products ignite more slowly. For the given conditions, this increases the upper limit whereas the lower limit is unaffected for ethyl propionate and ethyl butyrate. For ethyl acetate, however, the lower limit is affected due to more instability.

The main objective of the acidogenic fermentation route is to produce transportation fuels from low-value biomass. It tries not only to reduce the number of conversion processes but also to minimize the energy-consuming separation processes. Therefore, the next chapter will focus on the differences of combustion characteristics of those products in fuel blends. Our results invite analyzing whether this fuel blend could take advantage of these differences to extend the HCCI zone by promoting the ignition with EtBu and smoothing it with EtAc.

CHAPTER 3

Experimental investigation of tri-component ethyl ester blends in HCCI

This chapter is an updated version of the paper published in :
F. Contino, F. Foucher, C. Mounaïm-Rousselle, and H. Jeanmart. Combustion characteristics of tri-component fuel blends of ethyl acetate, ethyl propionate and ethyl butyrate in HCCI. *Energy & Fuels*, 2011, in press. doi: 10.1021/ef200193q

3.1 Introduction

Biofuels need to comply with detailed physicochemical requirements to be used in common spark ignition or compression ignition engines. The efficiency of the whole biofuel production processes is, therefore, affected by the successive conversion steps; for example, according to the type of crops and the production route, first generation biofuels consume between 40 and 85% of the fuel energy output [46, 47].

The homogeneous charge compression ignition (HCCI) engine offers not only a great potential of efficiency improvement and emission reduction (i.e. NO_x and soot) [3, 4, 48, 49] but it can also be run on a large variety of fuels, including low-grade fuels, given that the appropriate operating conditions are chosen [7, 50–52]. Therefore, simpler and more efficient conversion processes can be used for biofuel production, as illustrated by Mack et al. with the use of wet-ethanol [8].

This chapter focuses on the products that can be derived from acidogenic fermentation (acidogenesis). Acidogenesis is part of the anaerobic

digestion that is commonly used to decrease negative ecological effects of polluting compounds [12]. This simple and efficient process produces volatile fatty acids (including acetic, propionic, and butyric acids) from low-value biomass wastes. Therefore, it has been identified as an attractive alternative for bioenergy or chemicals production [9–11, 13]. The volatile fatty acids are generally not used in internal combustion engines because of the resistance of materials. They can be combined with ethanol (also produced in small proportions during the first stages of the acidogenic fermentation) to produce ethyl acetate (EtAc), ethyl propionate (EtPr), and ethyl butyrate (EtBu).

The overall process produces a mixture of various esters in proportions that vary with the fermentation conditions and biomass sources [10–13]. Removing unwanted components or maintaining a precise formulation of the biofuel requires more energy-consuming separation processes. Therefore, to use the fuel blends directly in an engine, their effects on the combustion timing need to be characterized.

Alternative fuels are also foreseen as a solution to the limited HCCI zone, i.e. the range of loads and speeds where HCCI combustion is possible [6]. It is therefore important to understand how particular fuel properties have an impact on the ignition timing and combustion duration.

This chapter has two main objectives: first, to provide information to direct the fermentation process towards a portion of the mixture region that is the most suitable, and, second, to understand the impact of these esters to improve the control and the operating zone of the HCCI engine.

In the previous chapter, we characterized experimentally the ignition timing and the HCCI zones of EtAc, EtPr and EtBu, as compared to ethanol [72]. Results have shown that these fuels ignite more slowly than ethanol. For the given conditions, the upper load limit of the HCCI operating zone was increased while maintaining the lower limit for EtPr and EtBu. However, the ignition of EtAc was so delayed that the lower limit was modified because of more instability.

This chapter analyzes experimentally tri-component blends of EtAc, EtPr and EtBu in a HCCI engine. It proposes a generic model, including the effect of each component and their interactions. It then presents

the mixture design to estimate the parameters of this model. Finally, it discusses the contribution of these parameters and determines those controlling the ignition timing.

3.2 Fuel blends

3.2.1 Characteristics of the fuels

The main fuel characteristics of EtAc, EtPr and EtBu are summarized in Table 3.1. They are described in more details in the previous chapter.

Table 3.1: Fuel characteristics

	EtAc	EtPr	EtBu
	$C_4H_8O_2$	$C_5H_{10}O_2$	$C_6H_{12}O_2$
AFR_{stoich}	7.85	8.8	9.52
Density [kg/l]	0.897	0.891	0.886
LHV [MJ/kg]	23.79	26.53	28.64
LHV [MJ/l]	21.34	23.64	25.38
HCCI zone [bar] [72]	2–6	1–5	1–4
Mm [kg/kmol]	88.1	102	116
LHV stoich. mixture [$MJ/kg_{mixture}$]	2.689	2.707	2.741
Fermentation proportion range [$\%_{vol}$] [10–13]	15–87	5–50	7–78

Several studies discuss the acidogenesis production for various biomass feedstocks and processing units [10–13]. The range of volume fractions reported in these studies defines the domain in which fuel blends will be tested (see Figure 3.1). EtPr is generally produced in lower proportions (below 50%) because of the competition between butyrate type fermentation and propionate type fermentation [13].

The HCCI zones reported in Table 3.1 were obtained for given inlet conditions, i.e. the range of indicated mean effective pressure (IMEP) reached for each fuel has not been optimized. Nevertheless, these values are used to compare the relative ignitability of the fuels: a lower knock limit is observed when the fuel ignites earlier, due to higher maximum

pressure rise rate, and a higher misfire limit is observed when the fuel ignites later, because of more instability. The HCCI zones presented in Table 3.1 indicate that EtBu ignites first and that EtAc ignites last.

3.2.2 Mixture design

In the context of octane number (ON) experiments, a quadratic blending model is generally needed when the region of fuels proportions is large [73]. This leads to both synergistic and antagonistic effects [74].

HCCI experiments using blends of EtAc, EtPr and EtBu have not been reported. The order of interaction is therefore unknown and, as a conservative choice, we used a Scheffé cubic model to establish the mixture design in the region of interest. Any parameter of interest Y is then modeled by

$$\begin{aligned} Y = {} & \beta_1 X_{\mathrm{EtAc}} + \beta_2 X_{\mathrm{EtPr}} + \beta_3 X_{\mathrm{EtBu}} \\ & + \beta_{12} X_{\mathrm{EtAc}} X_{\mathrm{EtPr}} + \beta_{13} X_{\mathrm{EtAc}} X_{\mathrm{EtBu}} + \beta_{23} X_{\mathrm{EtPr}} X_{\mathrm{EtBu}} \\ & + \gamma_{12} X_{\mathrm{EtAc}} X_{\mathrm{EtPr}} (X_{\mathrm{EtAc}} - X_{\mathrm{EtPr}}) \\ & + \gamma_{13} X_{\mathrm{EtAc}} X_{\mathrm{EtBu}} (X_{\mathrm{EtAc}} - X_{\mathrm{EtBu}}) \\ & + \gamma_{23} X_{\mathrm{EtPr}} X_{\mathrm{EtBu}} (X_{\mathrm{EtPr}} - X_{\mathrm{EtBu}}) \\ & + \beta_{123} X_{\mathrm{EtAc}} X_{\mathrm{EtPr}} X_{\mathrm{EtBu}}. \end{aligned} \tag{3.1}$$

where X_{EtAc}, X_{EtPr}, and X_{EtBu} indicates the volumetric fraction of EtAc, EtPr, and EtBu, respectively. This model will be compared to the Scheffé quadratic model, i.e. $\gamma_{ij} = 0$ and $\beta_{ijk} = 0$.

The estimation of the 10 parameters in equation (3.1) requires at least 10 different blends. Two additional blends were added to have further information on the significance of these parameter estimates while maintaining a manageable number of experimental points. The 12 different blends (see Figure 3.1) were selected with a D-optimal criterion, i.e. minimizing the generalized variance of the estimates of these parameters for the specified model [75]. The main characteristics of the fuel blends are shown in Table 3.2.

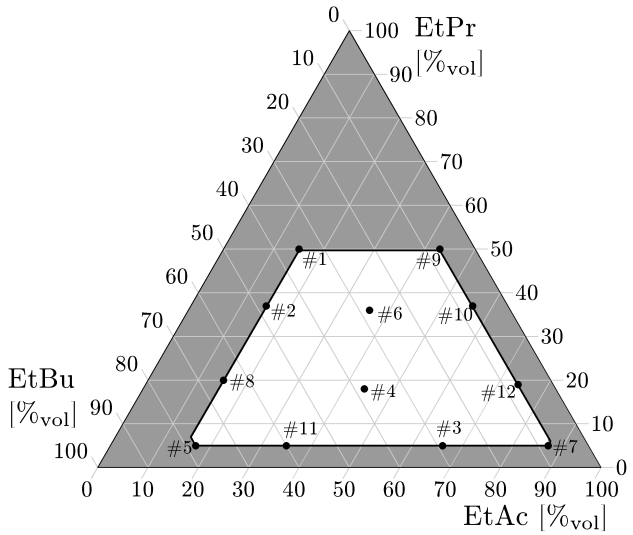

Figure 3.1: The twelve experimental points selected with a D-optimal criterion in the region of produced blends.

Table 3.2: Characteristics of the fuel blends

ID	EtAc [%vol]	EtPr [%vol]	EtBu [%vol]	LHV [MJ/kg]	AFR_{stoich}	LHV stoich. mix. [MJ/kg_{mix}]
#1	15	50	35	26.93	8.91	2.718
#2	15	37	48	27.22	9.01	2.720
#3	66	5	29	25.38	8.43	2.692
#4	44	18	38	26.19	8.70	2.701
#5	17	5	78	27.86	9.21	2.729
#6	36	36	28	26.18	8.68	2.704
#7	87	5	8	24.33	8.03	2.696
#8	15	20	65	27.60	9.13	2.725
#9	43	50	7	25.52	8.44	2.703
#10	56	37	7	25.16	8.32	2.699
#11	35	5	60	26.95	8.95	2.709
#12	74	19	7	24.67	8.15	2.697
min	15	5	7	24.33	8.03	2.692
max	87	50	78	27.86	9.21	2.729
mean	42	24	34	26.17	8.66	2.708
range [%]				13.5	13.7	1.4

3.3 Experimental setup

3.3.1 Engine details and data acquisition

The engine is based on the same engine as in the previous chapter. In these experiments, no exhaust gas analyzer was used (see Figure 3.2), another piston head was used which slightly modified the geometric compression ratio to 16.36 (the effective compression ratio is 15.35), and the temperatures of the cooling water and the lubricating oil were set at a value of 94°C and 85°C, respectively. The specifications of the engine are listed in Table 3.3.

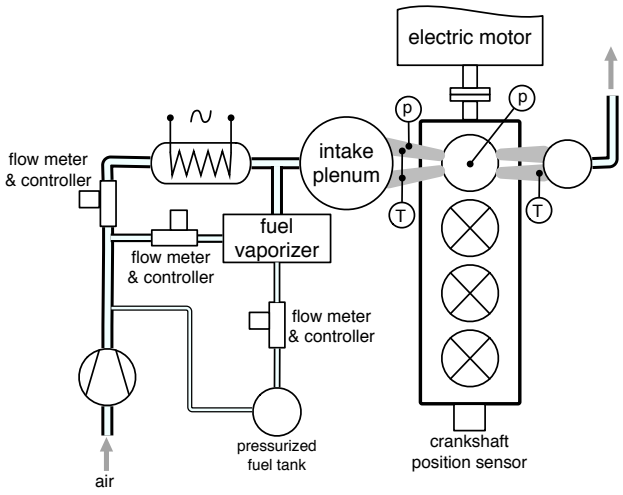

Figure 3.2: Schematic of the installation showing the flow of air and fuel entering the engine.

3.3.2 Experimental procedure

The main objective was to characterize the combustion timing for the twelve fuel blends. They were therefore compared at the same intake conditions. These conditions were measured in the intake manifold and set to 1.5 bar and 235°C. The inlet conditions were chosen so that most of the CA50 are in a narrow range around top dead center (TDC).

Table 3.3: Engine details

Bore [mm]	85
Stroke [mm]	88
Displacement [cm^3/cyl.]	499
Connecting rod length [mm]	145
Geometric Compression ratio	16.36
Effective Compression ratio [63]	15.35
Number of valves	4

The engine speed and equivalence ratio were selected to have a smooth functioning and a complete combustion. They were set to 1200 rpm and 0.3, respectively.

Pressure data from 100 consecutive cycles were stored and analyzed by the data acquisition system when combustion was stabilized. To evaluate the reproducibility, these measures were replicated randomly at least 4 times for each blend. Among the parameters calculated on each cycle were the maximum pressure ($P_{\max}$), the crank angle at which $P_{\max}$ occurred, the maximum pressure rise rate (MPRR), and the indicated mean effective pressure (IMEP). The mean values and standard deviations of these parameters based on 100 cycles were calculated online and used to determine stabilization.

The reported mass-averaged temperatures were computed using the ideal gas law in combination with the measured pressure, the known cylinder volume, and the temperature at bottom dead center (T_{BDC}). We considered that T_{BDC} was equal to the temperature measured just before the inlet valves. This is a good approximation when comparing the fuel blends on the same engine with the same settings [72].

The heat release rate (HRR) was computed using the two-step algorithm described in the previous chapter.

To characterize the combustion, three parameters were calculated for each cycle: CA10, CA50, and CA90. They correspond to the points where 10, 50 and 90% of the cumulative heat release is reached, respectively. CA10 is a good indicator of the combustion start for single-stage

fuels, as in this work. CA50 is often used to monitor the combustion and adjust the inlet conditions. The difference between CA90 and CA10 defines the combustion duration.

The fuel blends were prepared and supplied to the fuel tank with an error on the volume fraction of the components lower than 1%.

The emissions for the experiments on pure components were presented in the previous chapter. These emissions were quite similar for each component. Their modeling in the mixture region is therefore not included in this study.

3.4 Results

3.4.1 Auto-ignition timing

As shown in Table 3.2, the range of air-fuel ratio, is not negligible (14% of the mean value). In the region of fuel blends, the specific heats vary between 1122.7 and 1124.1 J/(kg·K) (computed using JANAF tables, here at 700 K for illustration) for blends number 5 and 7, respectively. The corresponding difference of temperature before ignition is approximately 5 K. While this difference is small, it has an important contribution to the onset of the combustion. It can be illustrated by the difference of ignition timing when the same fuel is used with two different inlet temperatures. For a difference of 2 K in the inlet mixture, which corresponds to the 5 K difference before ignition, the mean CA50 is delayed by nearly 1 CAD (see Figure 3.3).

In addition to the effect of temperature histories, each fuel has its own ignition kinetics. Both effects are very important for the ignition timing in HCCI [5]. The fuel blends had therefore different combustion characteristics according to their position in the mixture space. The start of ignition of all blends were located between the ignition of EtBu and EtAc (see Figure 3.4), as expected after the study on the three pure components [72].

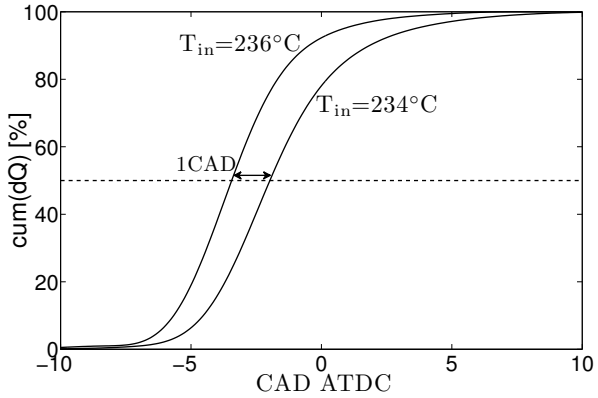

Figure 3.3: Difference of CA50 for pure EtBu corresponding to a 2K difference for the inlet temperature.

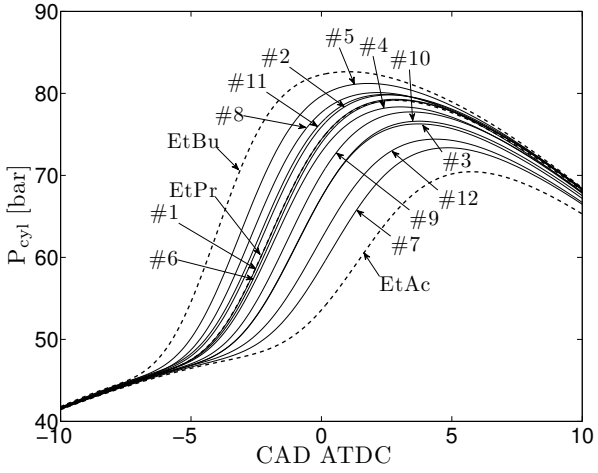

Figure 3.4: Cylinder pressure for the twelve blends (solid lines) along with the three pure components (dashed lines) for the engine setup used in this chapter.

3.4.2 Blending models

Table 3.4 shows the experimental results for all blends. The small standard deviations allows the use of the mean value to describe the effect of each component in the blending models.

Table 3.4: Mean value and standard deviation of all experimental results for the twelve fuel blends sorted by increasing value of CA50.

	CA50 [CAD]		max(dp/dθ) [bar/CAD]		CA10 [CAD]		CA90−CA10 [CAD]	
ID	mean	std	mean	std	mean	std	mean	std
#5	-2.68	0.18	8.20	0.55	-4.91	0.17	5.25	0.27
#8	-2.27	0.19	7.71	0.55	-4.59	0.20	5.57	0.29
#11	-1.88	0.19	7.43	0.53	-4.26	0.19	5.79	0.29
#2	-1.78	0.21	7.39	0.56	-4.16	0.21	5.86	0.32
#1	-1.37	0.21	7.34	0.53	-4.05	0.22	5.92	0.31
#6	-1.29	0.18	7.11	0.53	-3.73	0.20	6.09	0.29
#4	-1.26	0.19	7.08	0.60	-3.71	0.20	6.14	0.32
#9	-0.52	0.23	6.51	0.48	-3.10	0.24	6.58	0.29
#10	-0.24	0.22	6.33	0.55	-2.85	0.23	6.70	0.30
#3	-0.22	0.23	6.26	0.56	-2.84	0.21	6.75	0.31
#12	0.46	0.25	5.84	0.43	-2.25	0.27	7.05	0.29
#7	1.15	0.26	5.35	0.45	-1.68	0.26	7.39	0.30

The parameters of the cubic and of quadratic models of equation (3.1) are shown in Table 3.5. They were obtained by least-squares fitting. Both cubic and quadratic models were used to describe CA50, the start of ignition (CA10), the combustion duration (CA90−CA10) and the MPRR. The analysis of variance shows that the hypothesis of constant value for these variables in the whole range of blends is indeed rejected, i.e. most of the variance around the mean is explained by the models.

Both models fit the experimental results very well, and the adjusted R^2 does not change significantly between the quadratic and cubic models (see Table 3.5). This indicates that the cubic blending coefficients are not contributing to the quality of the fit. The quadratic models for

Table 3.5: Estimates of the parameters for the cubic and quadratic models, and fit quality indicators R^2 and R^2_{adj}.

	CA50 [CAD]		max(dp/dθ) [bar/CAD]		CA10 [CAD]		CA90−CA10 [CAD]	
ID	Cubic	Quadratic	Cubic	Quadratic	Cubic	Quadratic	Cubic	Quadratic
β_1	1.99	2.19	4.69	4.64	-0.99	-0.80	7.73	7.93
β_2	1.67	0.46	6.40	6.06	-1.12	-2.29	7.80	7.09
β_3	-3.67	-3.23	9.62	8.58	-5.64	-5.39	4.48	4.89
β_{12}	-7.77	-6.28	2.21	4.08	-6.88	-5.26	-3.67	-3.25
β_{13}	-1.31	-2.97	-1.20	1.69	-1.37	-2.52	0.56	-1.09
β_{23}	-1.44	-1.09	-3.57	0.20	-1.72	-0.91	0.05	-0.41
γ_{12}	2.53	-	0.79	-	2.56	-	1.34	-
γ_{13}	-0.18	-	1.64	-	0.11	-	0.29	-
γ_{23}	-2.89	-	4.02	-	-1.98	-	-3.05	-
β_{123}	-7.02	-	15.97	-	-4.54	-	-8.51	-
R^2	0.988	0.986	0.953	0.943	0.989	0.988	0.970	0.964
R^2_{adj}	0.985	0.985	0.943	0.937	0.987	0.986	0.965	0.960

CA50, CA10, CA90−CA10 and MPRR are presented in Figure 3.5. The major effects are due to the linear terms with a slight effect of the quadratic terms. The lack-of-fit test shows that the model is likely true, i.e. the hypothesis of adequate model cannot be rejected [75].

The major effects on the ignition timing are due to the proportions of EtAc and EtBu (see Figure 3.5). The combustion delay and combustion duration increase when the proportion of EtBu decreases or when the proportion of EtAc increases. These effects are not observed for proportions of EtAc above 75%, where the timing is constant for constant EtAc. The proportion of EtPr has a small direct effect on the combustion characteristics (see Figure 3.6). It has however an antagonistic effect on both EtBu and EtAc, i.e. for higher proportions of EtPr, the ignition timing is less modified for a given difference of proportions of EtAc and EtBu.

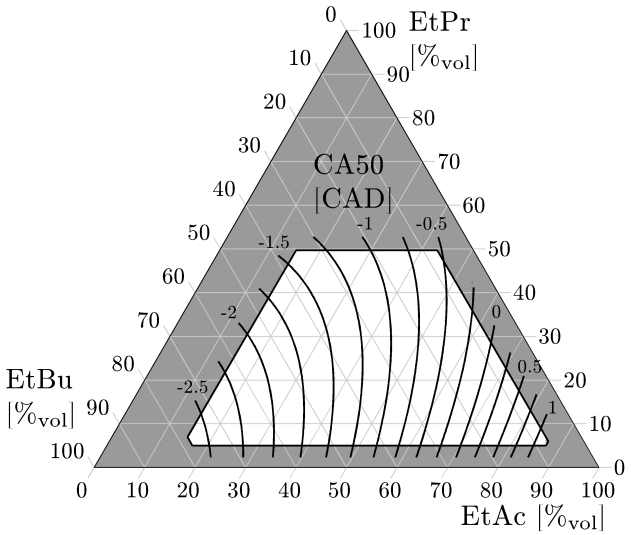

(a)

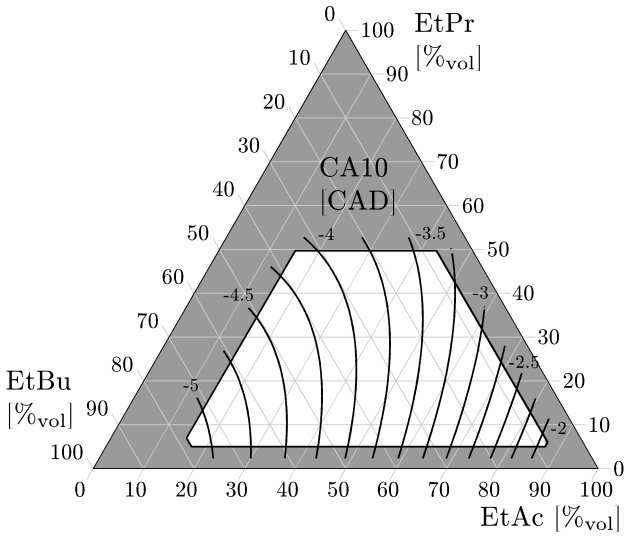

(b)

Figure 3.5: Ternary graph of : a) CA50 [CAD] and b) CA10 [CAD].

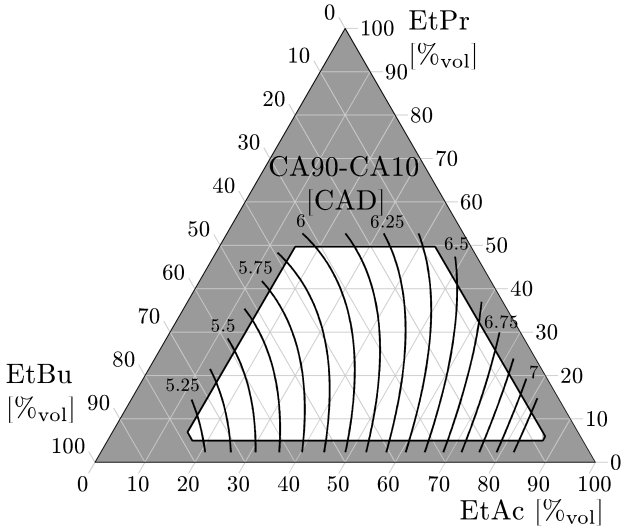

(c)

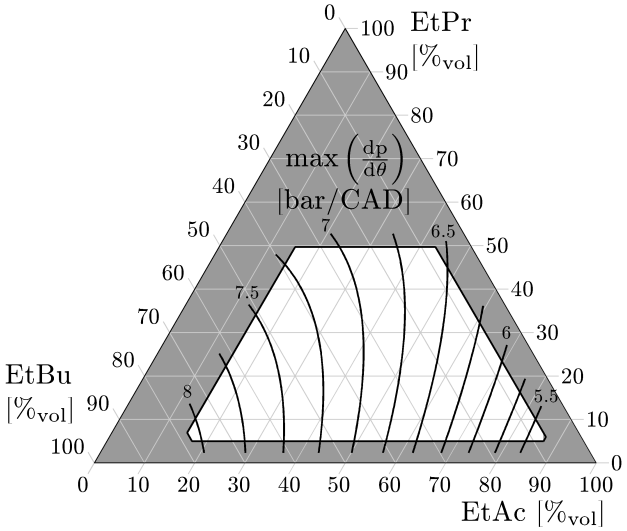

(d)

Figure 3.5: Ternary graph (cont'd) of : c) CA90−CA10 [CAD] and d) max(dp/dθ) [bar/CAD].

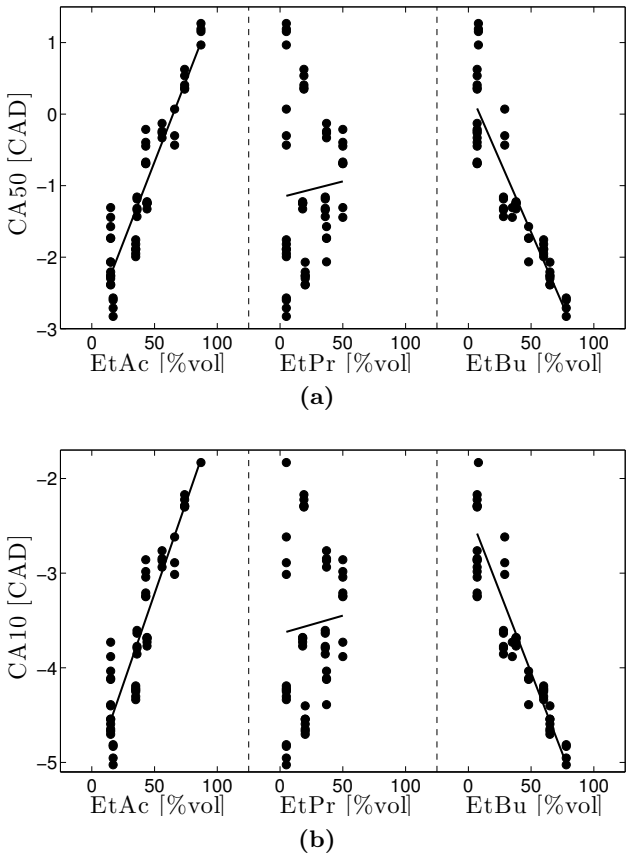

Figure 3.6: Effect of the volume fraction of EtAc, EtPr and EtBu on a) CA50 and b) CA10 (repetitions for each fuel blend are included).

As described in the previous section, the trends observed in Figure 3.5 are mainly determined by the intrinsic kinetics and the temperature history. Here, both effects are combined: EtBu has the shorter ignition delay, followed by EtPr and EtAc [72]; the temperature before ignition is higher near EtBu and lower near EtAc (difference of 5K).

The modeling of the experimental variance of CA50 and CA10 has shown that there is a trend of more instability when approaching EtAc. While the fit for these two parameters is not optimal (R^2 around 0.5), the analysis of variance and the lack-of-fit test clearly confirms the trend (see Figure 3.7 for the second-order fit). This is in good agreement with the results of the previous chapter, showing more instability when the

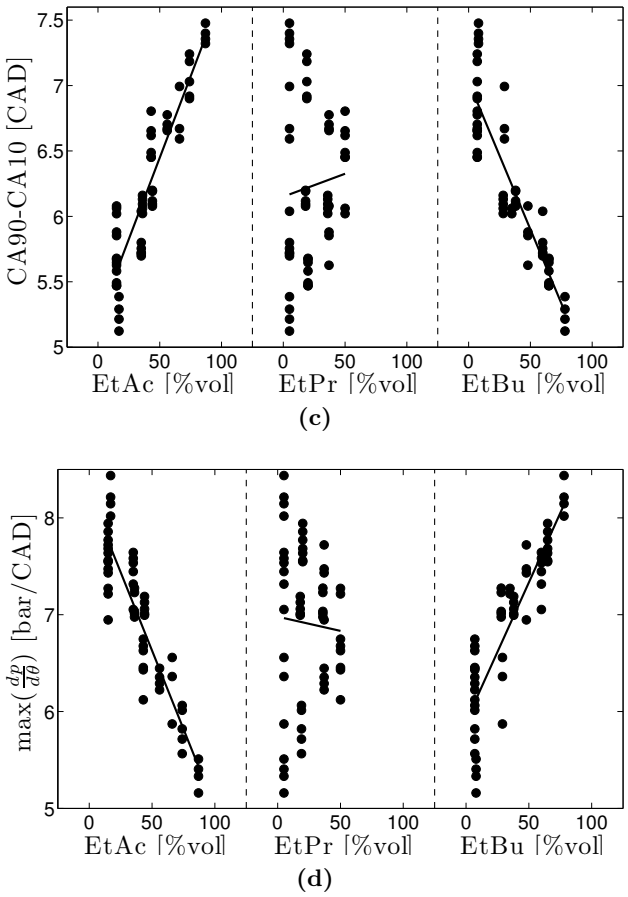

Figure 3.6: Effect of the volume fraction of EtAc, EtPr and EtBu (cont'd) on c) combustion duration and d) MPRR (repetitions for each fuel blend are included).

ignition is delayed.

When the ignition delay decreases, the start of ignition is faster and the combustion duration is smaller, hence increasing the MPRR (see Figure 3.5d). As it is physically obvious, the negative correlation between CA50 and the MPRR is well observed in the experiments (see Figure 3.8).

The analysis of variance shows that the mean value of IMEP is not constant in the region of the blends studied. It is slightly higher when

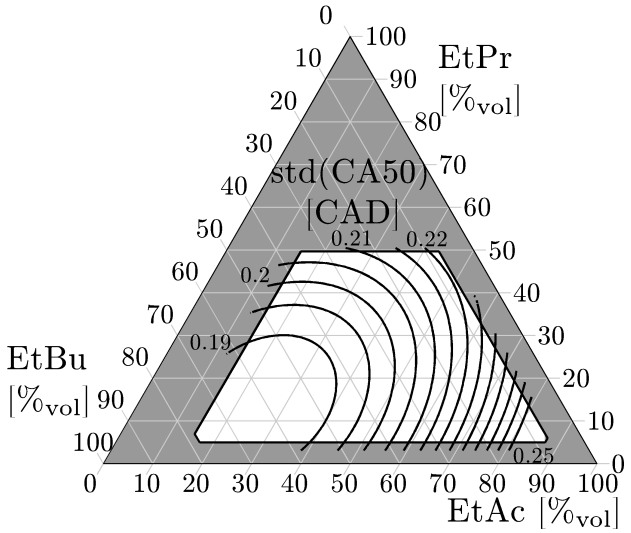

Figure 3.7: The modeling of the experimental variance of CA50. There is a trend of more instability near EtAc.

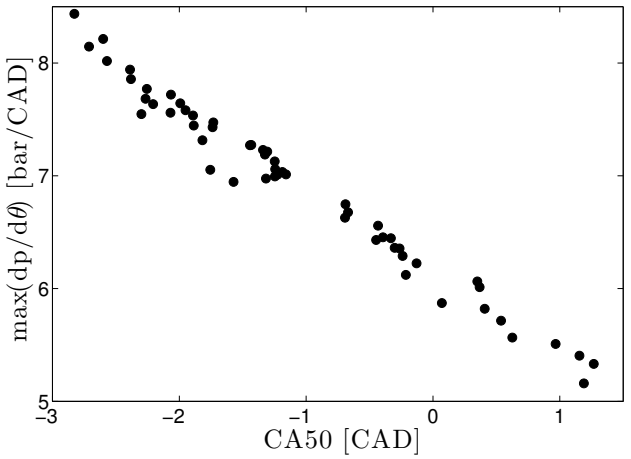

Figure 3.8: Negative correlation between CA50 and max(dp/dθ), repetitions for each fuel blend are included.

approaching EtPr and slightly lower when approaching EtAc. The difference is low (around 4% of the mean value) and is probably explained by the combined effect of a better ignition timing and a slight difference of the mixture LHV.

3.5 Conclusion

Fuel blends of various proportions of EtAc, EtPr, and EtBu are all exploitable in HCCI. The ignition delay is mainly determined by the proportions of EtBu and EtAc. It decreases when the proportion of EtBu increases or when the proportion of EtAc decreases. EtPr has nearly no direct effect on the ignition timing but has an antagonistic effect on the other components. It mitigates the impact of the proportion variability on the ignition timing.

These results suggest that, on one hand, the smaller ignition delay of EtBu could help reduce the inlet temperature and make the use of these esters as transportation fuels easier. However, on the other hand, the dilution effect of EtPr could maintain a prescribed timing, while the blend composition changes. Directing the fermentation process toward the optimal blend would therefore depend upon these two aspects but overall it should be in the region with low proportion of EtAc.

Moreover, as these esters have a long ignition delay compared to known references, their use in SI engines could be very effective, similarly to what is achieved with ethanol.

CHAPTER 4

Iterative method for the reduction of kinetic mechanisms

This chapter is an updated version of the paper published in:
F. Contino and H. Jeanmart. Study of the HCCI running zone using ethyl acetate. *SAE Technical Paper*, 2009-01-0297, 2009. doi: 10.4271/2009-01-0297

It is also based on the paper presented in:
F. Contino, V. Dias, and H. Jeanmart. Simplified kinetic mechanism of ethyl acetate oxidation for HCCI engines. In Sixth Mediterranean Combustion Symposium, Ajaccio, France, June 7-11, 2009

4.1 Introduction

The combustion characteristics of EtAc, EtPr and EtBu have been investigated in the two previous Chapters. To understand the underlying combustion mechanisms, an accurate modeling is required. CFD simulations including reaction kinetics is a very useful tool to further analyze the combustion in ICE. The computational time of using very detailed combustion mechanisms for this analysis is however prohibitive.

As a first step towards using detailed mechanisms, we have defined a reduction method based on an iterative preprocessing technique. The objective of this method is to identify redundant species through reaction rate analysis. A species is assumed to be redundant if the elimination of all its consuming reactions induces no significant error to the remaining species [17]. Preprocessing reduction methods generally use several

sample points to process the reduction. They then derive the simplified mechanism from the union of the sets of species generated for each of these sample points [76]. In this study, we used a 0D HCCI model instead of specific sample points to cover the entire range of thermochemical conditions encountered in a HCCI engine cycle. We applied this procedure to the reduction of the EtAc mechanism.

Table 4.1 presents some fuel properties of EtAc (see Section 1.3 in Chapter 1 for more details). EtAc is completely miscible with gasoline. It separates in presence of water, but, unlike ethanol, it is not hygroscopic and it will probably not separate due to contact with air moisture. Water absorption is 3% w/w and the distribution of EtAc in 2-phase gasoline/aqueous solution has still to be investigated.

Table 4.1: Fuel properties of EtAc.

Density [kg/l]	0.897
Viscosity [mm^2/s]	0.42
Flash point [°C]	-4
Autoignition point [°C]	460
LHV [kJ/kg]	23790
Boiling temperature [°C]	77
AFR_{stoich}	7.85

EtAc is the basic compound of other products that can be derived from the acidogenesis route. The results are therefore of great interest as a starting point to characterize the whole group of esters produced. In addition, as suggested in [6], another aspect of using alternative fuels in HCCI engines is to widen the HCCI operating zone. This zone is generally defined based on experimental limits. We have adapted the definition of these limits to compute them from simulation results.

This chapter has two main objectives: the development of a simple reduction method and the definition of the HCCI operating limits based on CFD simulations. It first presents the reduction methodology and applies it to EtAc. Then, it describes the CFD model that is used in

the later part to derive the operating zones of EtAc and iso-octane.

4.2 Reduction methodology

The simplification process is based on a 0D HCCI model that we have developed. This model first compute the volume V of the combustion chamber according to the engine specifications :

$$V = \frac{V_d}{\tau - 1}\left(1 + \frac{1}{2}(\tau - 1)\left(\beta + 1 - \cos\theta - \sqrt{\beta^2 - \sin^2\theta}\right)\right), \quad (4.1)$$

where V_d is the displacement volume, τ is the compression ratio, β is the ratio of connecting rod length to crank radius, and θ is the crank angle.

It then computes the pressure p by solving the following ODE :

$$\frac{C_V}{R} V \frac{dp}{d\theta} = \frac{dQ_{\text{fuel}}}{d\theta} - \frac{C_p}{R} p \frac{dV}{d\theta} - \frac{dQ_{\text{wall}}}{d\theta}, \quad (4.2)$$

where $\frac{dQ_{\text{fuel}}}{d\theta}$ is the heat source from the chemical reactions computed by Chemkin-II routines [77], C_p and C_V are the specific heats at constant pressure and constant volume, respectively, R is the ideal gas constant, and $\frac{dQ_{\text{wall}}}{d\theta}$ is the rate of wall heat transfer given by Hohenberg's correlation [68] (see Chapter 2). The temperature is computed by the ideal gas law.

The following set of ODE is also solved to compute the mass fraction of the species Y_i:

$$\frac{dY_i}{d\theta} = S(T, p, Y), \quad (4.3)$$

where S is a chemical source term computed by Chemkin-II routines, and with the constraint that

$$\sum_{\text{all species}} Y_i = 1. \quad (4.4)$$

The whole set of equations is integrated implicitly by a stiff ODE solver based the backward differentiation formulas [78].

This global model of the HCCI engine allows to compute the contribution of each reaction to the combustion process during the entire cycle. These contributions are analyzed at various equivalence ratios to identify the principal reaction paths in HCCI conditions. The reactions are then removed according to their net contribution, and species without reactions are subsequently removed. Some key reactions have a major impact on the onset of the combustion but a small overall contribution, e.g. initiation reactions (see Section 1.4 in Chapter 1). The removed reactions are therefore validated by comparing the heat release rate (HRR) of the simplified mechanism with the one of the complete mechanism. The whole process is iterated to reach a specified level of reduction. The outline of the method is given in Figure 4.1.

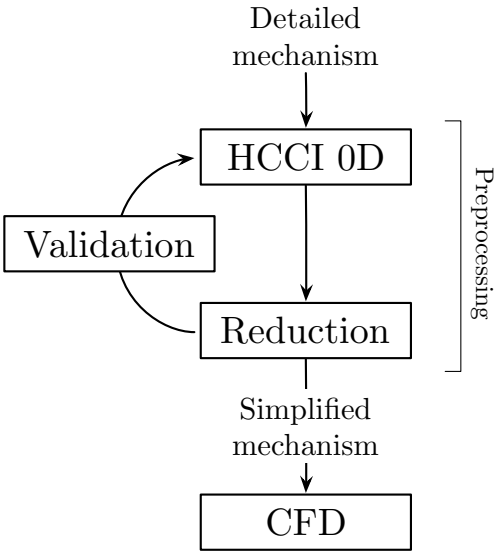

Figure 4.1: The method first uses the detailed mechanism in a preprocessing step where it is iteratively reduced by analyzing the reaction contribution computed during the whole engine cycle by the HCCI 0D model. The simplified mechanism is then used in the CFD simulation.

To apply this method to EtAc, we used the EtAc sub-mechanism from Gasnot et al. [62] and the small hydrocarbon combustion mechanism from Miller et al. [79]. The EtAc oxidation was investigated by

Gasnot et al. in a burner at low pressure (around 5 kPa) where laminar stoichiometric premixed methane-air flames were seeded with various proportions of EtAc (below 3%). The first decompositions steps include 23 chemical species and 142 elementary reactions. The small hydrocarbon part (C_1 to C_3) of Miller et al. involves 37 chemical species and 160 elementary reactions. The mechanism based on these two parts has 60 species and 302 reactions.

Using the iterative reduction procedure, the reactions with a contribution below 1% have been first removed. Species with no remaining consumption reactions were consequently removed. The discarded reactions and species are mainly part of the mechanism that is important only at high equivalence ratio. The reaction path containing the primary radical $CH_3COOCH_2\dot{C}H_2$ has also been removed since it does not play an important role in the conditions of HCCI combustion.

The simplified mechanism of EtAc includes 41 chemical species and 203 elementary reactions. Figure 4.2 shows the initial path of the reaction scheme. There is a slight difference with the one reported by Gas-

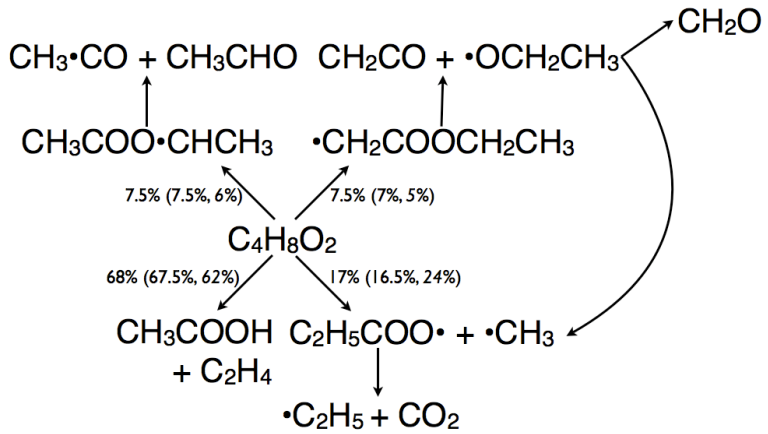

Figure 4.2: First oxidation steps of EtAc. The initial path of the simplified mechanism in engine conditions (outside the parentheses) is slightly different from the path reported by Gasnot et al. [62] in low pressure flame conditions (second value inside the parentheses). The values in engine conditions for the simplified and the detailed (first value inside the parentheses) mechanisms are in good agreement.

not et al. [62] but it can be explained by the different thermochemical conditions used in the HCCI simulations compared to the experiments reported by Gasnot et al.

Figure 4.3 presents the heat release rate and the total heat released of the detailed and the simplified mechanism of EtAc at three equivalence ratios. The error on the maximum values are below 10% and the shift between peaks of HRR is below 0.5 CAD for the lowest equivalence ratio.

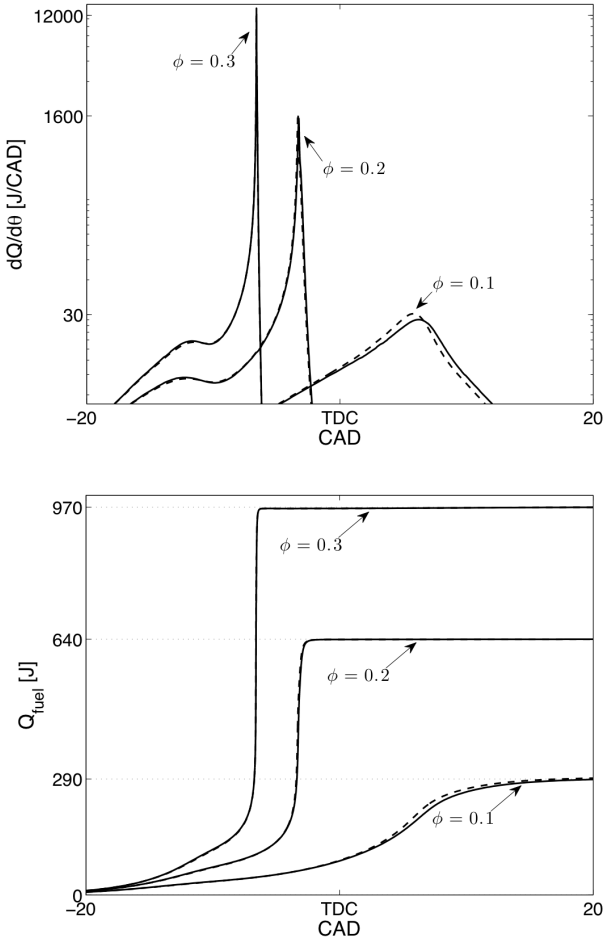

Figure 4.3: Heat release rate (above, log scale) and total heat released (below) for the simplified (solid) and the detailed mechanism (dashed) of EtAc at equivalence ratio $\phi = 0.1$, $\phi = 0.2$ and $\phi = 0.3$.

Because of the characteristic bulk reaction of 0D models, the HRR is very high for the highest equivalence ratios. While there is a small discrepancy for the lowest equivalence ratio, the results of the simplified and the detailed mechanisms are in very good agreement, in both timing and maximum value.

Even if the level of details obtained in the 0D simulations is far from what is obtained with CFD simulations, the range of thermochemical conditions is still very large. Therefore, the reduction procedure takes into account most of the conditions encountered in the following CFD simulations.

4.3 Computational setup

4.3.1 CFD model

The computational grid was generated with the commercial software GAMBIT [80] according to the geometry and requirements specified by Hessel et al. [81] (see Figure 4.4). In this study, Hessel et al. performed a grid resolution analysis to validate the choice of this level of refinement. This study also used a well characterized engine with extensive experimental data which was used to validate this CFD setup.

The simulations are performed on an axisymmetric mesh because the experimental setup was designed to mostly generate a swirl motion. The mesh consists of about 33000 quad cells at IVC. Different meshes were tested for the bowl part, the pave mesh gave a good compromise between the number of cells and the skew factor.

The simulations have been performed using the commercial CFD software Fluent [82]. The RNG k-ε turbulence model, which is modified to take into account the compressibility, has been adopted in this study. It has shown good results in the modeling of the heat transfer, which plays a great role in HCCI because auto-ignition phasing depends greatly on the pressure and temperature history during the compression phase [5] (see also Chapter 1). Laminar equations are used to compute the wall heat transfer because $y+$ is below 10 for the whole cycle which is

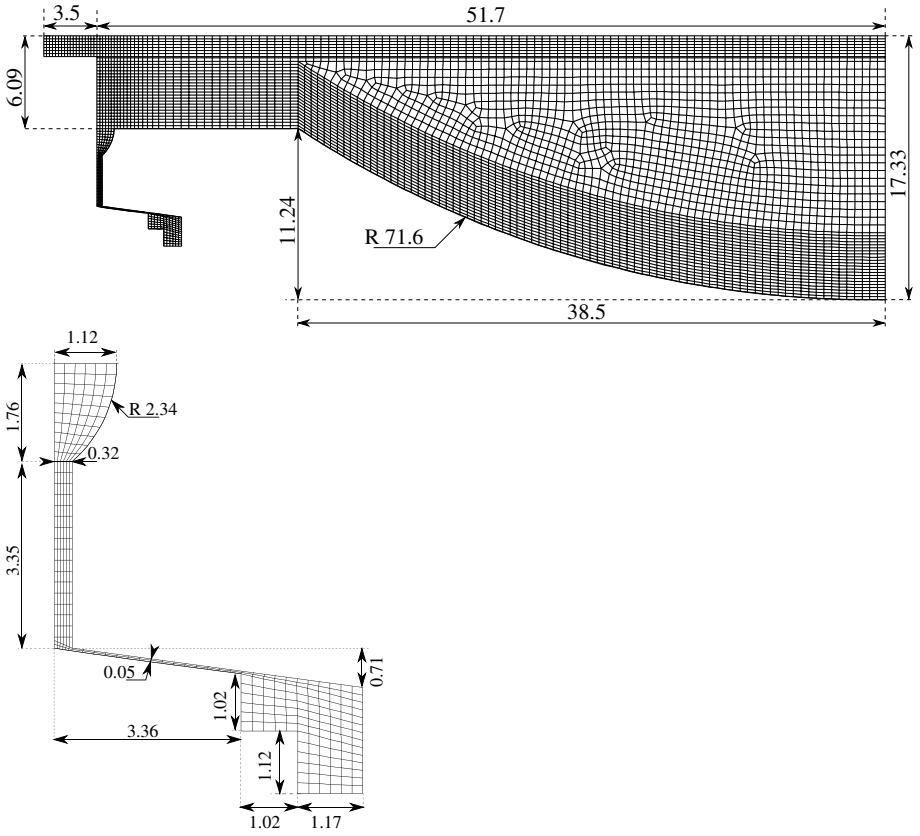

Figure 4.4: Mesh at TDC (above) and details of the crevices zone (below). Dimensions are in mm.

generally the limit accepted for engine simulations [83].

Transport equations are solved for each species at grid level but the eddy dissipation concept model (EDC) is also included to simulate molecular mixing at subgrid level. EDC accounts for the interactions between turbulence and chemistry. It computes reaction zones in the turbulent fine structures where combustion takes place [84, 85]. Reaction rates are integrated numerically and solutions are tabulated dynamically using the in situ adaptive tabulation (ISAT) method [40].

We have also included the swirl motion within the cylinder by implementing a user-defined function. This function uses the Bessel function of the first kind and first order (j_1) to define the tangential velocity v_s along the cylinder bore according to the swirl profile factor α [86] (see Figure 4.5):

$$v_s = C(R_s)\ j_1\left(\alpha \frac{2r}{\text{bore}}\right)\ , \tag{4.5}$$

where r is the radial position from the center of the cylinder, and C is a constant computed from another parameter: the swirl ratio R_s. The value chosen here for α is 3.11 which is the common value for engine applications [81]. Limit values for α are 0 for the solid-body profile and 3.83 when the velocity is zero at the wall. The swirl ratio R_s determines the intensity of the swirl motion. It is defined as the ratio between the solid-body angular velocity with the same angular momentum as the actual flow, and the crankshaft angular rotational speed [86, 87]. The swirl ratio is set to 0.9 in this study. During computation, the swirl initial velocity in the cells adjacent to the wall comply with the no-slip boundary condition.

The CFD configuration parameters are summarized in Table 4.2.

4.3.2 Model validation

The CFD model was validated using the iso-octane mechanism developed by Jia et al. [88]. This skeletal mechanism involves 38 species and 69 reactions (including global reactions) and was validated under HCCI conditions (i.e. low equivalence ratio and high pressure) for ignition

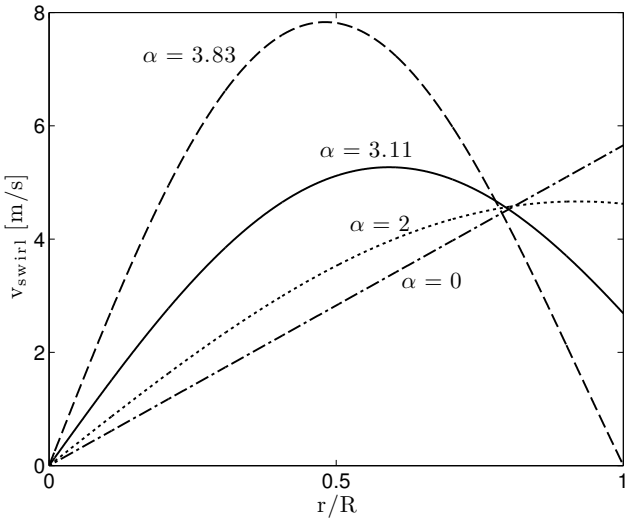

Figure 4.5: Tangential velocity along the cylinder bore for different swirl profile factors (α). In this study α is set to 3.11. $\alpha = 0$ is the solid-body profile and $\alpha = 3.83$ is the limit profile where the swirl velocity is zero at the wall.

Table 4.2: Model Configuration

Bore x Stroke	103.4 mm x 120 mm
Connecting rod length	192 mm
Compression ratio	13.3
Engine Speed	1200 rpm
IVC	160 CAD BTDC
EVO	120 CAD ATDC
Time step	0.1 CAD
Swirl ratio	0.9
Swirl profile factor	3.11

timing, burn durations, and pressure traces. Since the mechanism does not include all the intermediate radicals as in detailed mechanisms, it slightly overestimates the burn rates.

In the simulations, the value of the initial pressure is uniform throughout the domain and remains constant while the initial temperature (and mass at the same time) is adjusted to match the experimental pressure trace at $\phi = 0.2$. The selected initial temperature is 462 K which is 12 K less than in the model from Hessel et al. [81] but closer to the estimated BDC temperature from their experimental data (461 K). This indicates the consistency of our model with experiments. Our simulation results agree well with experimental and model data from Hessel et al. [81] (see Figure 4.6). Other test cases at different equivalence ratios are shown in Appendix B.

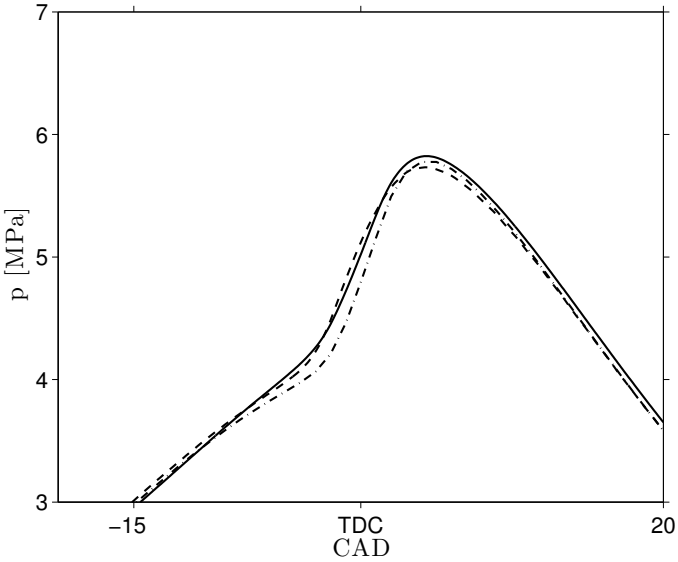

Figure 4.6: Pressure near TDC, $\phi = 0.2$. Dash-dotted and dashed: model and experiments from Hessel et al. [81]. Solid: Current study.

The concentrations of CO and CO_2 at EVO agree well with the numerical results from Hessel et al. and both agree very well with the experimental results (see Figures 4.7 and 4.8).

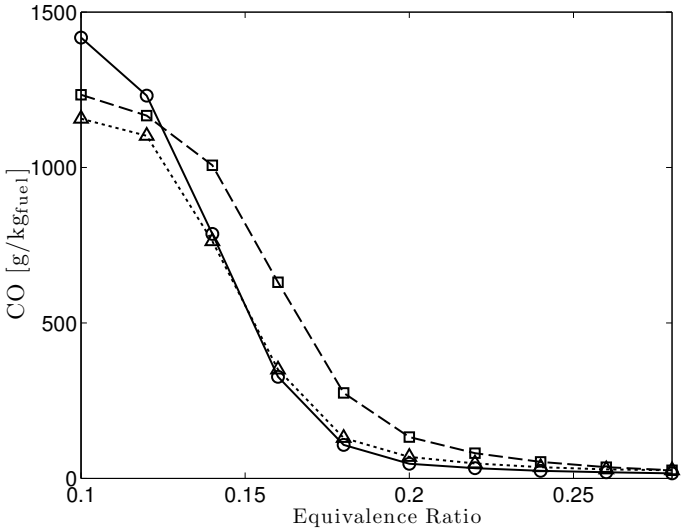

Figure 4.7: CO concentration at EVO. Dotted: Model from Hessel et al. [81]. Dashed: Experiments from Hessel et al. [81] Solid: Current study.

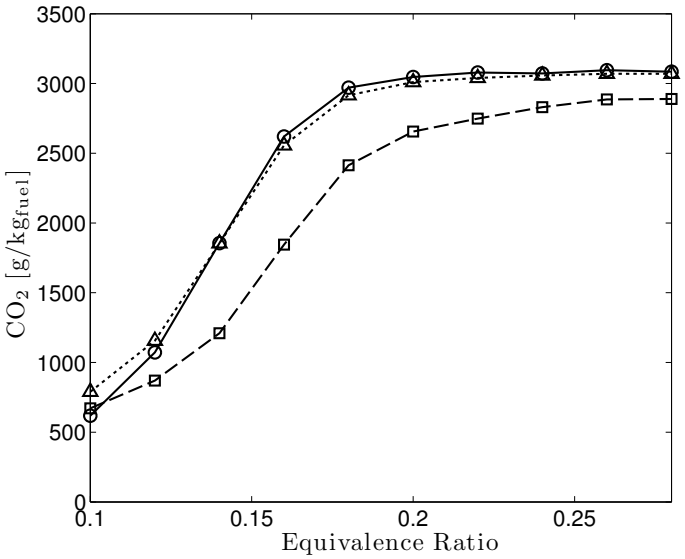

Figure 4.8: CO_2 concentration at EVO. Dotted: Model from Hessel et al. [81] Dashed: Experiments from Hessel et al. [81] Solid: Current study.

However, the unburned fuel mass fraction at EVO is underestimated (see Figure 4.9).

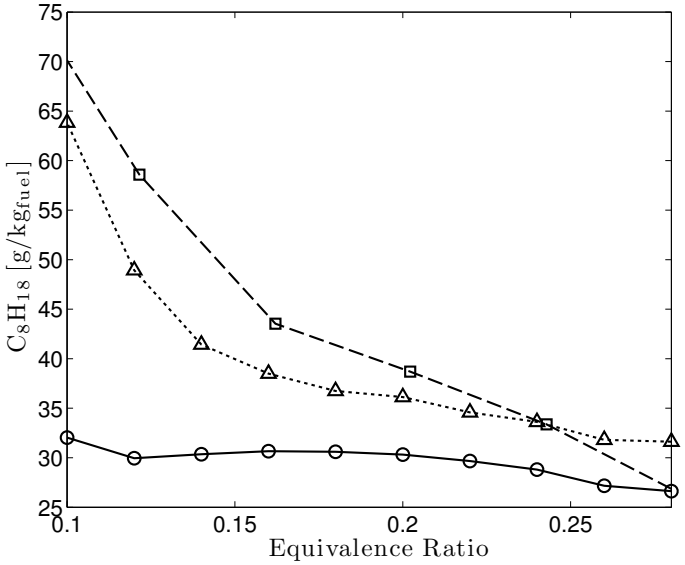

Figure 4.9: Fuel concentration at EVO. Dotted: Model from Hessel et al. [81]. Dashed: Experiments from Hessel et al. [81] Solid: Current study.

This underprediction is due to the low temperature chemistry and more particularly to the decomposition of large hydrocarbons that is extremely simplified. The low temperature kinetic of the mechanism leads to high conversion of C_8H_{18} into $OC_8H_{15}O$ and C_8H_{16} among which the later has the highest mass fraction. But the sum of the C_8H_{18} and C_8H_{16} mass fractions overestimates the experimental data (see Figures 4.9 and 4.10). Indeed, in order to limit the number of species, the mechanism does not totally include the conversion from large hydrocarbons to smaller hydrocarbons. The low temperature chemistry is only followed by three reactions to break the larger molecules into smaller ones. Therefore the reaction path is ended because of the high activation energy needed for these reactions. During the expansion phase, the major portion of C_8H_{16} is in the gasket or leaving the crevices (see Figure 4.11). It is therefore mostly located near the wall, where the low tem-

perature reactions did take place but where the thermal energy is too low to further decompose this species.

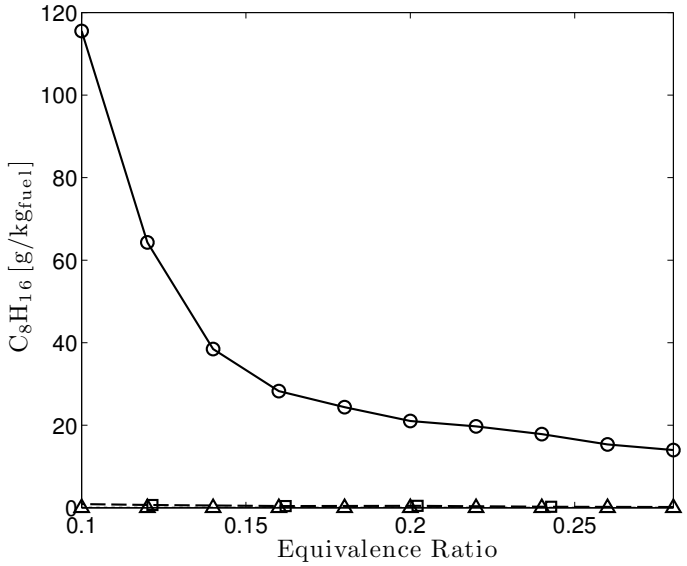

Figure 4.10: C_8H_{16} concentration at EVO. Model from Hessel et al. [81] is zero everywhere. Dashed: Experiments from Hessel et al. [81] Solid: Current study.

Even if the skeletal mechanism does not compute precisely the amount of unburned iso-octane, the total unburned hydrocarbons in the exhaust gas are in good agreement with experiments (see Figure 4.12).

4.4 Operating zone

4.4.1 Zone limits

Usually, the operating zone is determined according to experimental results. Cyclic variations leading to operating instability defines the lower limit, also called misfire limit. High combustion noise defines the upper limit, also called knock limit [5]. Both limits are experimental and depend on the engine design. While the upper limit can be linked to the

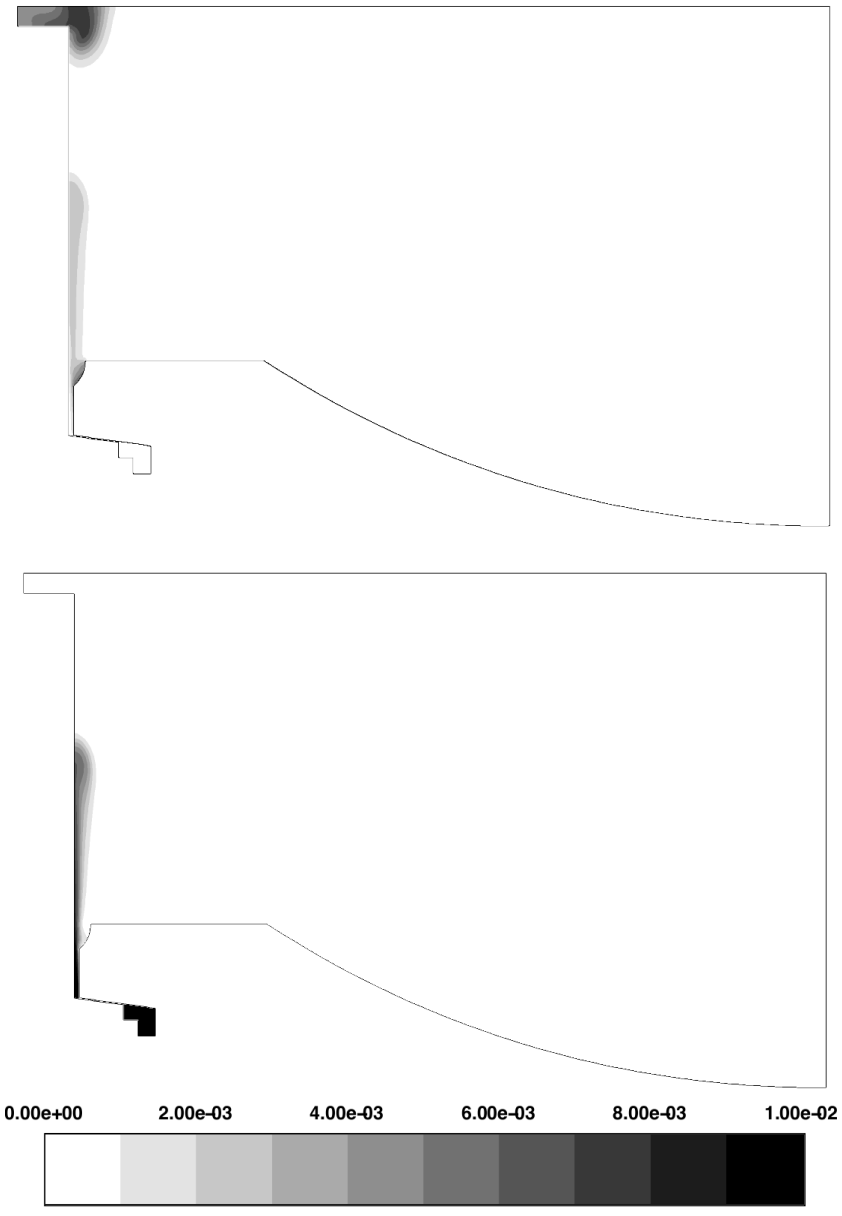

Figure 4.11: Top: C_8H_{16} mass fraction at 40°CAD ATDC. Bottom: C_8H_{18} mass fraction at 40°CAD ATDC. The mass fractions for the two compounds are mainly near the wall and remain there after the bulk combustion.

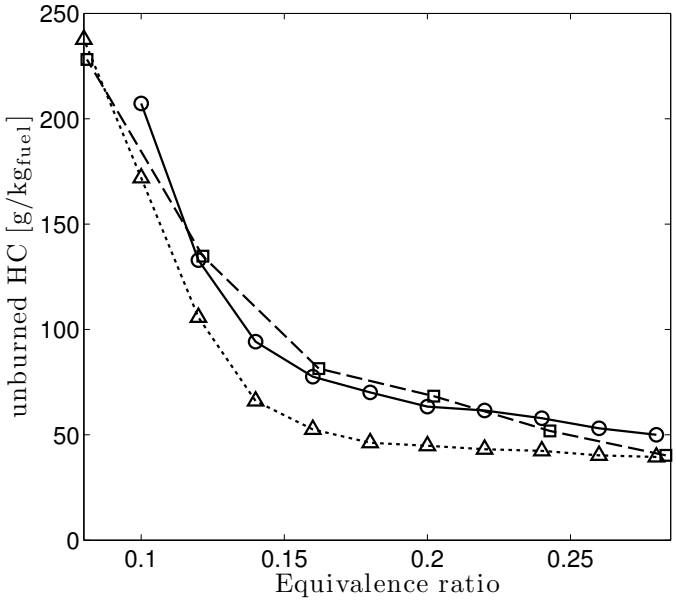

Figure 4.12: Total unburned hydrocarbon at EVO. Dotted: Model from Hessel et al. [81]. Dashed: Experiments from Hessel et al. [81] Solid: Current study.

maximum pressure rise rate (MPRR; set to 5 bar/CAD as in Kalghatgi et al. [69]) which can be easily computed from simulation results, the lower limit required several cycles to have a meaningful statistics on the instability which is not affordable with CFD simulations. We have therefore defined another criterion for this limit based on simulations results.

The cyclic variation is represented by the coefficient of variation (CoV) of the indicated mean effective pressure (IMEP). Kalghatgi et al. defined a correlation to relate an indicator of instability X to CA50 and ϕ [69] :

$$X = 1.55 \text{ CA50} - 52 \ \ \phi \,. \tag{4.6}$$

For low cyclic variations (CoV$<$ 10%), Kalghatgi et al. have shown that X should be negative. It is worth noting that this parameter was first defined for experiments with no exhaust gas recirculation (EGR) which is not the case here. When using EGR, ϕ in equation (4.6) should be replaced by the effective equivalence ratio ϕ^*:

$$\phi^* = \frac{\phi(1 - EGR)}{1 - \phi \ EGR} \,. \tag{4.7}$$

The use of the effective equivalence ratio takes into account the EGR even if it has not been originally included in the correlation.

Results using the axisymmetric model have shown that some cycles with $X < 0$ are clearly not in the operating zone. Therefore, we used additional criteria to fine tune this limit. At a given EGR and equivalence ratio, we ran several simulations with different initial temperatures. If this initial difference was amplified and led to a greater difference in the final temperature, it indicated that the simulation was near the misfire limit. To further check this limit, a second criterion was to monitor the CO emissions. As mentioned in Chapter 1, near the misfire limit, the thermal energy within the combustion chamber is too low to sustain the conversion from CO to CO_2. A significant increase in CO is therefore expected.

4.4.2 Results

Finding the suitable initial conditions for the simulations is one of the major challenges in computing the operating zones. In order to initiate the combustion, the engine model was run with exhaust gas trapped during negative valve overlap. During the experiments, the initial conditions for one cycle depend on the final conditions of the previous cycle in particular when using large amount of internal EGR. Achieving the same numerically, i.e. periodic engine cycles, would require to run many cycles until the initial conditions converge. This would extremely increase the computational time. To handle this problem, we used the 0D HCCI model described above to compute the converged initial conditions.

The 0D model considers that the charge is perfectly mixed, which leads to a higher pressure rise rate compared to experiments. In addition, the temperature is homogeneous, which does not allow the combustion to start in hotter region and globally delays it until the whole charge reaches the auto-ignition temperature. Although the shape of the pressure trace does not fully matches the simulation results, the thermochemical conditions at the end of the expansion stroke are similar. These conditions are then used to compute approximate initial values for the temperature and the mass fractions of fuel, air and exhaust gas. These initial values were considered uniform throughout the numerical domain and were also checked for compatibility after the simulations.

The wall temperatures are usually function of the heat released in the cylinder. But their evolution depends on the engine settings. To avoid further complexity, we kept the wall temperatures used in the validation process, at $\phi = 0.2$ ($T_{Head} = 407$ K, $T_{Liner} = 384$ K and $T_{Piston} = 440$ K) along with the same initial pressure.

The operating limits depend on the engine speed because this speed has an impact on the gas exchange efficiency, the heat transfer and the charge inhomogeneities (temperature and EGR/air/fuel mixture) [6]. In this study, the impact of the engine speed was only partially included: the closed part of the cycle was modeled with no inhomogeneities and the gas exchange phase was only included through the swirl motion. Therefore, we computed the zone limits at 1200 rpm, which was validated in

the previous section.

This method does not intend to give the absolute operating zone for the tested fuels. The operating zone depends on the engine design and settings. In addition, simplified or skeletal mechanisms can lack accuracy in some particular conditions. Therefore, the operating zone that we have obtained is used to compare qualitatively iso-octane and EtAc in the same conditions.

The work done by the engine during one cycle is represented by the gross IMEP ($IMEP_g$) which only takes into account the closed part of the cycle. The ranges of $IMEP_g$ for iso-octane and EtAc are quite similar (see Figure 4.13). EtAc is more resistant to auto-ignition and has a higher knock limit, as expected from the experiments presented in Chapter 2 and 3. On the other hand, its misfire limit is also higher. The operating zone for EtAc is thus shifted in the higher $IMEP_g$ compared to iso-octane.

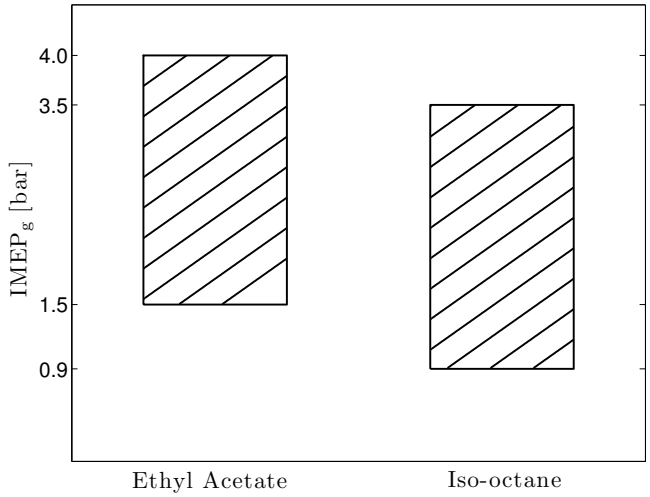

Figure 4.13: Running zone at 1200 rpm. The range of gross IMEP is the same but the limits are shifted upward for EtAc.

The computed misfire limits are low compared to real engine conditions. This can be explained by the particular definition of the lower

limit, which is less accurate than using $\mathrm{CoV}_{\mathrm{IMEP}}$ of experimental results. The comparison between the two fuels still remains relevant as we are using the same operating conditions.

The lower limit was detected by using the temperature criterion presented in the previous section. In conditions near the misfire limit, small differences in initial temperature led to great differences later in the cycle (see Figure 4.14). On the contrary, near the knock limit, the same differences in initial temperature led to a small offset in the combustion timing but it did not influence the temperature at the end of the cycle.

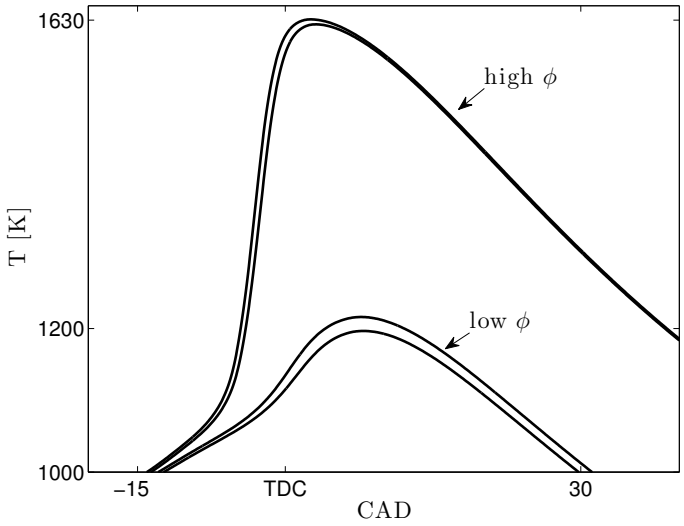

Figure 4.14: Near the misfire limit, a small difference in initial temperature has a great influence compared to high load cycles.

Using this criterion, the definition of X^* is modified for EtAc :

$$X^* = 1.55\,\mathrm{CA50} - 35\;\phi^*\,, \tag{4.8}$$

while for iso-octane this correlation becomes

$$X^* = 1.55\,\mathrm{CA50} - 23\;\phi^*\,. \tag{4.9}$$

The difference between (4.8), (4.9) and the parameter proposed by

Kalghatgi et al. is certainly due to the different and large amount of EGR used to obtain auto-ignition in our simulations.

Finally, it appeared that the CO mass fraction does not help to precisely establish the misfire limit because its evolution showed no dramatic change near the limit (see Figure 4.15). However it is interesting to note that, with the combustion mechanisms that we used, the CO emissions of EtAc were very low compared to that of iso-octane.

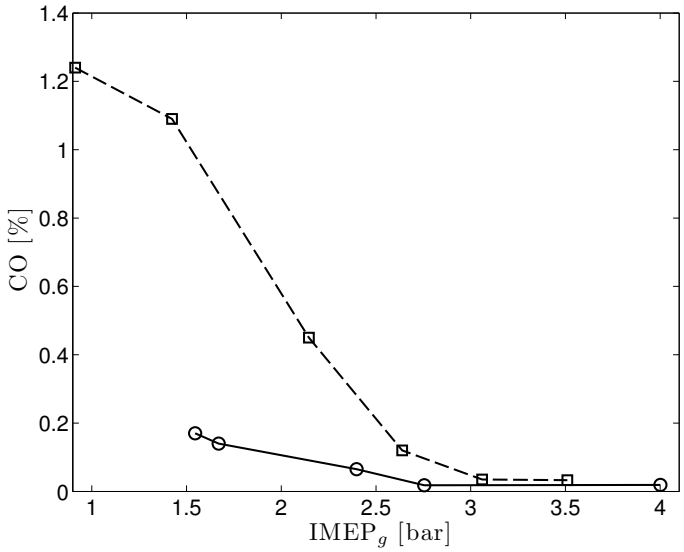

Figure 4.15: CO concentration at EVO. Dashed: Iso-octane. Solid: Ethyl acetate. Ethyl acetate has lower levels of CO for all loads.

4.5 Conclusion

In this chapter, we have presented a method to reduce the kinetic mechanism iteratively as a preprocessing step. The mechanism was then used in CFD simulations to compute the HCCI operating limits at a given engine speed.

We adopted a new definition of the HCCI operating limits based on the simulation results. The knock limit was defined by a specific value of the maximum pressure rise rate and the misfire limit was defined based

on a correlation that links an indicator of instability X to CA50 and ϕ. However, the effect of the large EGR rates on this correlation still requires further analysis.

This model was used to study the operating zone of EtAc and iso-octane. The comparison of the two zones has shown that EtAc has a load amplitude similar to iso-octane and that its operating zone is shifted toward higher loads.

The reduction method developed in this chapter is very simple to use but may be tedious when the number of species is higher than 100, because each removed species should be validated. Moreover, it is straightforward to identify and to eliminate the unimportant elementary reactions that contribute negligibly to the production rate of every species, but it is more complicated to identify and to eliminate the unimportant species because of the coupling between species.

Because of the large size of the kinetic mechanisms when modeling complex fuels, there is a need for developing reliable automatic reduction methods that require minimum user input. This is the objective of the next Chapter.

CHAPTER 5

Tabulation of Dynamic Adaptive Chemistry

This chapter is mainly an updated version of the paper published in:
F. Contino, H. Jeanmart, T. Lucchini, and G. D'Errico. Coupling of in situ adaptive tabulation and dynamic adaptive chemistry: An effective method for solving combustion in engine simulations. *Proceedings of the Combustion Institute*, 33(2):3057–3064, 2011. doi: 10.1016/j.proci.2010.08.002

5.1 Introduction

The use of detailed chemistry has become a fundamental prerequisite for realistic computational fluid dynamics (CFD) simulations of the combustion process in internal combustion engines (ICE). Thanks to the comprehensive mechanisms, it is possible to describe the combustion of surrogate fuel mixtures over a wide range of operating conditions, the formation of the main pollutant emissions (soot, NO_x and HC) and the heat release rate under conventional and innovative combustion modes such as PCCI or HCCI [89–91]. When complex chemical mechanisms are included in combustion models, the evolution of the chemical species in each computational cell is performed by an operator-splitting technique, where an ODE stiff solver takes the thermochemical conditions (temperature, pressure and species concentration) and integrates the chemical problem over the time-step, solving the species and the energy equations [23]. However, this technique implies the evaluation of the Jacobian of the chemical system which is computationally demanding when hundreds of species and thousands of reactions are involved,

hence limiting the application of detailed kinetics for practical ICE simulations. To reduce the computational efforts, different approaches exist (see Section 1.5 in Chapter 1). Basically, CPU time reduction can be performed by solution storage and retrieval techniques or by the reduction of the chemical schemes. Several tabulation methods have been developed including, in situ adaptive tabulation (ISAT) [40], piecewise reusable implementation of solution mapping (PRISM) [41] or intrinsic low-dimensional manifold (ILDM) [42], further developed in flame prolongation of ILDM (FPI) [43]. The reduction of the chemical schemes can be performed by skeletal reduction through elimination of species and reactions that have a small contribution to the overall activity of the system. These methods include sensitivity analysis [27], computational singular perturbation (CSP) [28], directed relation graph (DGR) [17], DRG with error propagation (DRGEP) [24] and dynamic adaptive chemistry (DAC) based on DRG and DRGEP [37]. Other techniques could further reduce the resulting skeletal mechanism such as lumping [30], chemistry-guided reduction [32] or quasi steady-state assumptions (QSSA) [29].

Within the framework of ICE simulations, ISAT and DAC have proved to be particularly effective. Their adaptive behavior does not require the preprocessing or pretabulation of sample points which is more effective when a large range of thermochemical conditions is accessed.

Although ISAT and DAC provide a significant reduction of the computational time, the achieved speed-up is still not satisfactory when only one of the two approaches is applied in the simulation of ICE. This is due both to mixture inhomogeneities and changes in the thermodynamic conditions during the simulation. The first reduces the number of retrievals that can be used by the ISAT method and the second requires to perform a high number of ODE integrations even if DAC is used. For this reason, we propose a new methodology called TDAC (tabulation of dynamic adaptive chemistry) that combines the advantages of ISAT and DAC to solve complex combustion chemistry problems. Because the current version of the commercial software Fluent® used in the previous chapter can only import mechanisms with less than 50 species, the proposed approach has been implemented by the authors into the Lib-ICE

code, which is a set of libraries and solvers for ICE simulations based on the OpenFOAM® technology [92–94]. The performances of TDAC were firstly evaluated on a simplified geometry using n-heptane mechanisms and, finally, the proposed methodology has been further validated with experimental data of a real HCCI engine.

5.2 Computational methods

This section first describes the DAC and ISAT methods. Presenting the limits of ISAT, it then proposes a modification to improve the algorithm in ICE conditions. Finally, it discusses the new TDAC method with details on the coupling of DAC and ISAT.

5.2.1 Dynamic adaptive chemistry

The DAC method computes reduced mechanisms that are valid for the local thermochemical conditions, i.e. it reduces continuously the mechanism instead of preprocessing it [37, 95]. In these previous works, DAC has only been applied to 0D models. In this work, DAC has been extended to full CFD meshes with wall heat transfer.

The reduction algorithm is executed before every call to the stiff solver in each computational cell. It is based on the directed relation graph (DRG) method developed by Lu et al. [96]. It first computes the matrix of the normalized contributions that represents the error on the production and the consumption of a species when another is removed from the mechanism. This matrix also represents the strength of the direct link between two species.

Then the algorithm computes the strength of the paths connecting all the species to a user-defined search initiating set of species. In the following simulations, $\{\text{fuel}, \text{CO}, \text{HO}_2\}$ is used as the search initiating set.

In the final step, the reduction scheme removes from the mechanism the species with a value of path strength below a user-defined threshold, ε_{DAC}, and all the reactions containing at least one disabled species. The ODE associated with these disabled species are not solved, however,

their concentration are still considered when evaluating the rate function of the remaining three-body and pressure-dependent reactions. Based on the analysis of Liang et al. [37], $\varepsilon_{\mathrm{DAC}}$ is set to 10^{-4} in the following simulations.

The search algorithm originally loops over all species in the mechanism when computing the strength of the paths. Since most of the species are only connected to few others, in the current implementation, it is slightly modified to only evaluate the initialized direct links between species as proposed by Lu et al. [96]. When computing the matrix of contributions, another matrix is then created to store the direct links for each species.

5.2.2 In situ adaptive tabulation

The ISAT algorithm intends to reuse computationally demanding results, e.g. the integration of large and stiff ODE systems, by storing those results and all the data needed to retrieve them.

A thermochemical state is defined by the composition

$$\psi = \{Y_1, Y_2, ..., Y_{\mathrm{Ns}}, T, p\},$$

where Y_i are the species mass fractions, $\mathrm{N_s}$ is the number of species, T is the temperature and p is the pressure. The integration of the reaction equations for a fixed time step Δt maps the initial composition $\psi^0 = \psi(t_0)$ to the reacted value $\psi(t_0 + \Delta t)$ which is a unique function of ψ^0 called the reaction mapping, $\mathbf{R}(\psi^0)$.

The ISAT method stores this reaction mapping for subsequent uses. During computation, given a query point, ψ^q, it computes a linear approximation of the mapping:

$$\mathbf{R}(\psi^q) \approx \mathbf{R}^l(\psi^q) = \mathbf{R}(\psi^0) + \delta\mathbf{R}^l \ , \tag{5.1}$$

where $\delta\mathbf{R}^l = \mathbf{A}(\psi^0)(\psi^q - \psi^0)$ and $\mathbf{A}$ is the mapping gradient matrix defined by

$$A_{ij}(\psi^0) \triangleq \frac{\partial R_i(\psi^0)}{\partial \psi_j} \ . \tag{5.2}$$

The matrix $\mathbf{A}$ is related to the first order sensitivity coefficients with respect to initial conditions defined by

$$C_{ij}(\psi^0, t) \triangleq \frac{\partial \psi_i(t)}{\partial \psi_j^0} \ , \tag{5.3}$$

with

$$\mathbf{A}(\psi^0) = \mathbf{C}(\psi^0, t_0 + \Delta t) \ . \tag{5.4}$$

To compute $\mathbf{A}$, the following linear system of ODE is integrated implicitly from t_0 to $t_0 + \Delta t$:

$$\frac{\mathrm{d}}{\mathrm{dt}}\mathbf{C}(\psi^0, t) = \mathbf{J}(\psi(\mathbf{t}))\mathbf{C}(\psi^0, t) \ , \tag{5.5}$$

where $\mathbf{J}$ is the Jacobian and the initial condition is $\mathbf{C}(\psi^0, t_0) = \mathbf{I}$.

The linear approximation defined by equation (5.1) is valid in the region of accuracy (ROA) which is the connected region containing ψ^0 and all the ψ^q respecting the condition on the local error, $\varepsilon_{\text{local}}$:

$$\varepsilon_{\text{local}} = |\mathbf{R}(\psi^q) - \mathbf{R}^l(\psi^q)| = |\delta\mathbf{R} - \delta\mathbf{R}^l| \leq \varepsilon_{\text{ISAT}} \ , \tag{5.6}$$

where $\varepsilon_{\text{ISAT}}$ is a user-specified tolerance and $\delta\mathbf{R} = \mathbf{R}(\psi^q) - \mathbf{R}(\psi^0)$. Usually, the ROA is not computed according to this definition but is more conveniently approximated by a conservative hyper-ellipsoid in the composition space called ellipsoid of accuracy (EOA):

$$EOA \triangleq \delta\psi^T \tilde{\mathbf{A}}^T \mathbf{B}^T \mathbf{B} \tilde{\mathbf{A}} \delta\psi \leq \varepsilon_{\text{ISAT}}^2 \ , \tag{5.7}$$

where $\mathbf{B}$ is an optional scaling matrix, $\tilde{\mathbf{A}}$ is the modified $\mathbf{A}$ matrix and $\delta\psi = \psi^q - \psi^0$. $\mathbf{B}$ is used to manually modify the shape of the hyper-ellipsoid which allows to modify the retrieval tolerance for specific species (e.g. when the precision on a species of interest should be increased). $\tilde{\mathbf{A}}$ is obtained by limiting the smallest singular values to prevent them from generating very large principal axes (see [40, 97]) .

During the calculation, the table is built up according to the received queries. It consists of a binary tree with leafs and nodes. The leafs store ψ, $\mathbf{R}(\psi)$, $\mathbf{A}(\psi)$ and the EOA description. The nodes stores the

hyperplanes in the composition space that allow to scan the binary tree and to retrieve the closest stored composition. For each query, one of the following three operations is performed: retrieving, growing or adding. If ψ^q is in the EOA, ISAT retrieves the reaction mapping of ψ^q using equation (5.1). If ψ^q is not in the EOA, the stiff solver is called to compute the direct integration of the reaction equations and ISAT checks the local error using equation (5.6). If this error is less than $\varepsilon_{\mathrm{ISAT}}$, the current approximation of the ROA is too conservative and the EOA is grown to include ψ^q. Otherwise a new leaf is added to the binary tree to store $\mathbf{R}(\psi^q)$. Further details about ISAT can be found in [40].

The current implementation of ISAT also includes some new features introduced by Lu and Pope [97]. The definition of the EOA becomes

$$EOA \triangleq \delta\psi^T \mathbf{L}\mathbf{L}^T \delta\psi \leq 1 \ , \tag{5.8}$$

where $\mathbf{L}$ is the Cholesky factorization of $\tilde{\mathbf{A}}^T\mathbf{B}^T\mathbf{B}\tilde{\mathbf{A}}/\varepsilon^2_{\mathrm{ISAT}}$. Taking advantage of this EOA formulation, $\mathbf{L}$ is readily computed from the QR decomposition of $\mathbf{B}\tilde{\mathbf{A}}/\varepsilon_{\mathrm{ISAT}}$. The use of this matrix is computationally more efficient because the simple triangular matrix-vector multiplication $||\mathbf{L}^T\delta\psi|| \leq 1$ is used to check if a query point lies in the EOA. In addition, the growth process can be done by the rank-one modification algorithm [98] which allows to update the QR decomposition with only $O(\mathrm{N_s^2})$ operations instead of $O(\mathrm{N_s^3})$ [99].

5.2.3 Modification of ISAT

ISAT was originally developed for constant-pressure and high-temperature chemistry flows and it achieved a particularly good speed-up factor (around 10^3) in the context of particle based probability density function methods for chemically reacting turbulent flows. When a large range of thermochemical conditions is encountered in combustion simulations (ICE, gas turbine burners, ...), the number of queries resulting in retrieving is smaller and much time is spent in addition and growth with a consequent reduction of the speed-up factor to around 10 [40, 100]. Therefore, we adapted the ISAT algorithm for this kind of applications by regularly updating the binary tree. These modifications are illus-

trated here for the ICE case, but they are also valid for the simulation of other combustion systems.

The modification is similar to the periodical clean-up proposed in DOLFA (Database for on-line function approximation [101]). In the present implementation, a stored point is removed from the binary tree according to two user-specified parameters: a number of time steps N_{ms} and a number of growths N_{mg}.

For a moderate value of ε_{ISAT}, the use of N_{ms} allows to compute more accurately the reaction rate in the pre-ignition phase. Given that a new point is added to the binary tree according to ε_{ISAT}, a very small value is required to represent the first steps of the combustion. To avoid unnecessary severe tolerance for the main combustion, leading to a substantial increase in the computational time, the stored point is replaced when deemed too old, i.e. after N_{ms} time steps or crank angle degrees (CAD).

The growth process is limited by N_{mg} to decrease the total number of growths. In ICE simulations, before and during ignition, the queries are moving toward compositions with high pressure and temperature. This usually leads to distorted EOA where the queries are still within the tolerance, ε_{ISAT}, but relatively far from the center ψ^0 of the EOA (the stored composition). To illustrate this aspect, Figure 5.1 shows the EOA after a growth to include the query point ψ^q. Even if part of the following queries are in the EOA, part of them require additional growths as shown by the square and circle symbols in Figure 5.1. In this case, replacing the stored composition centered at ψ^0 by the one centered at ψ^q is more efficient. However, because of the conservative description of the EOA, very small values of N_{mg} stop reducing the total number of growths, but increase it dramatically. When the EOA is created, it is usually grown to include many other close points. But if it is replaced more often, many points included after few growths are then excluded. This is illustrated by the cross symbols in Figure 5.1.

Values for N_{ms} and N_{mg} in the context of HCCI simulations are given in the results section along with a sensitivity analysis.

As the stored points are useless after a few time-steps, the total size of

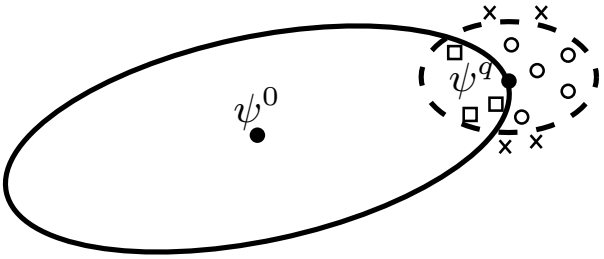

Figure 5.1: Instead of distorting the EOA by growing it with ψ^q, the number of retrievals increases when the EOA is replaced after N_{mg} growths by the one centered in ψ^q (square symbols and circle symbols). Very small values of N_{mg}, however, exclude close points in subsequent growths (cross symbols), hence leading to a higher total number of growths.

the binary tree can be strongly limited (around 1000 leafs) without any loss of efficiency. Furthermore, this limited size allows faster retrievals and avoids memory issues when using very large mechanisms. Once the maximal number of points is reached, the tree is cleared and repopulated with the use of a most recently used list.

In ICE simulations, the constant pressure assumption is not valid, therefore, the current implementation also stores the pressure.

5.2.4 TDAC: coupling of ISAT and DAC

The number of operations required for solving the chemical kinetics in CFD simulations depends on the number of cells in the mesh and the size of the oxidation mechanism. The number of cells gives the number of times the ODE system will be integrated. The size of the mechanism defines the level of complexity to integrate the system of stiff nonlinear ODE. Reduction of the computational effort for these separated aspects is achieved by the TDAC method, coupling ISAT and DAC. The ISAT algorithm intends to reuse previously computed results, hence decreasing the effect of the number of cells, whereas the DAC method finds a skeletal mechanism at runtime, hence reducing the effect of the mechanism size (see Figure 5.2).

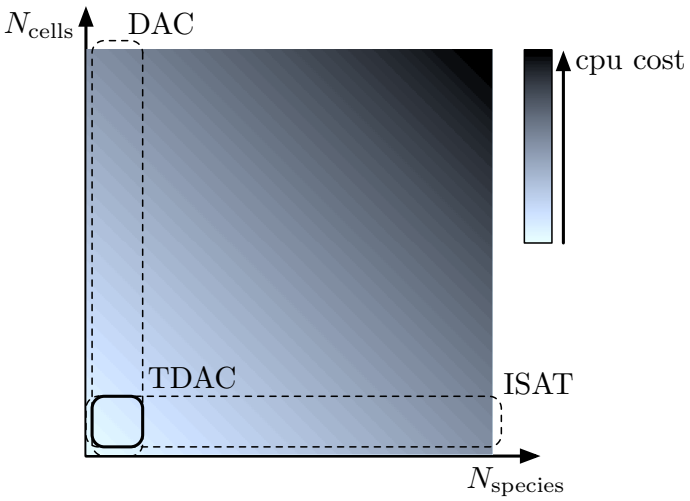

Figure 5.2: The TDAC method combines the best features of the ISAT and DAC methods and takes advantage of the synergy between these methods to significantly reduce the computational cost.

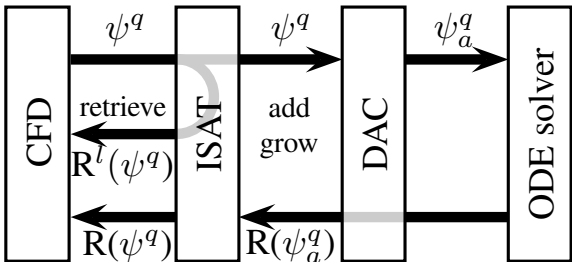

Figure 5.3: In the TDAC method, the ISAT algorithm tries to retrieve the mapping $\mathrm{R}^l(\psi^q)$ of the query composition ψ^q. In case of additions and growths, DAC simplifies the mechanism at runtime before providing the composition with active species ψ^q_a to the stiff ODE solver, which computes the mapping $\mathrm{R}(\psi^q_a)$. This mapping is then extended by ISAT to the full composition space $\mathrm{R}(\psi^q)$.

The coupling can be visualized as successive layers (see Figure 5.3): when ISAT receives a query ψ^q that needs to integrate the ODE set (growth and addition operations), it provides ψ^q to the DAC algorithm, which then finds the reduced mechanism for the local thermochemical conditions and provides the reduced set of active species ψ_a^q to the stiff ODE solver. This solver computes the reaction mapping for the reduced set $\mathrm{R}(\psi_a^q)$ that is used by ISAT to build the reaction mapping $\mathrm{R}(\psi^q)$ in the full composition space. Using simplification methods at distinct levels combines their effects and allows a significant reduction of the computational cost as shown in the next section.

The coupling with the DAC method requires ISAT to manipulate and store chemical points in a composition space with variable dimensions, i.e. with variable active species. Therefore, ISAT stores the mapping of the active species but new variables are introduced to extend the mapping to the full composition space when retrieving or growing points.

It may not be necessary to add new points to the binary tree when the number of active species changes. Therefore, the EOA needs to be checked and grown in the full composition space. Because $\mathbf{A}$ is computed through the Jacobian, when the number of species is reduced, it only takes active species into account and is more compact. To include inactive species in the definition of the EOA, the method uses an extended $\mathbf{A}$. This matrix includes the lines of the identity matrix corresponding to the inactive species index as if the reaction mapping was computed with equation (5.1) in the full composition space.

5.3 Results

This section first analyses the performance of TDAC compared to direct integration, ISAT, and DAC in simplified 2D HCCI cases using n-heptane mechanisms. Then, the method is validated in a real HCCI engine case using a detailed 857-species iso-octane mechanism.

5.3.1 Performance of TDAC

The performance of TDAC has been evaluated on a simplified 2D geometry to get direct integration results of the full HCCI cycle in workable time. The solver used to integrate the system of ODE is based on the semi-implicit mid-point rule developed by Bader and Deuflhard [102]. Four meshes with numbers of cells ranging from 63 to 374 at bottom dead center (BDC) have been used (the total number of cells changes during simulations because the dynamic mesh layering technique is used). To analyze the effect of the mechanism size, four n-heptane mechanisms with increasing number of species have been used: the 44-species skeletal mechanism of Liu et al. [20], the 159- and 282-species reduced mechanism of Seiser et al. [103] and the 561-species detailed mechanism of Curran et al. [104, 105].

The results of TDAC and direct integrations are in very good agreement as shown in Figures 5.4a and 5.4b.

The achieved speed-up factors are illustrated in Table 5.1 as a function of the number of mesh cells and chemical species when ISAT, DAC, or TDAC are used.

Table 5.1: Speed-up factor obtained for the simplified 2D HCCI cases.

		N_{cell} =	63	154	252	374
N_s =*44*	TDAC		5.5	8.4	9.1	9.6
	ISAT		5.7	9.0	9.1	12
	DAC		1.1	1.2	1.1	1.0
N_s =*159*	TDAC		15	19	24	28
	ISAT		12	13	16	16
	DAC		2.9	2.9	2.8	3.2
N_s =*282*	TDAC		27	37	40	56
	ISAT		13	17	19	28
	DAC		5.3	4.9	4.8	5.0
N_s =*561*	TDAC		50	105	110	150
	ISAT		6.5	9.0	8.7	13
	DAC		29	32	28	26

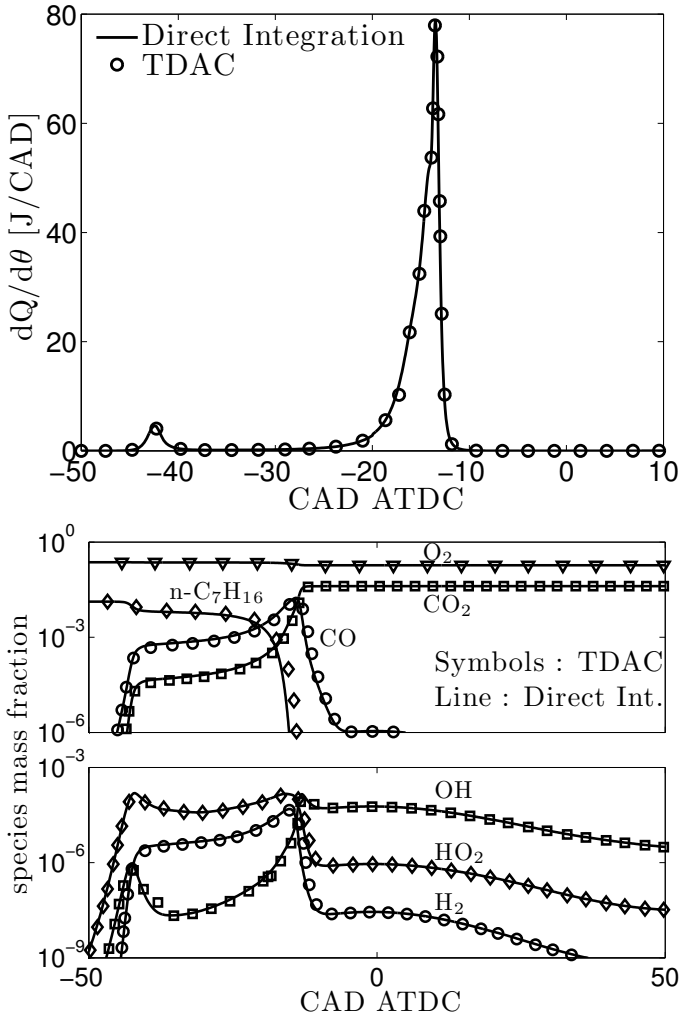

Figure 5.4: (a) Heat release rate and (b) species mass fraction for direct integration (line) and TDAC (symbols) on the HCCI simplified geometry with 374 cells using the 159-species mechanism.

The efficiency of ISAT depends on the level of inhomogeneity and the range of thermochemical conditions. For homogeneous thermochemical conditions, most of the queries are retrieved by ISAT, which requires $O(1)$ direct integrations. When completely inhomogeneous and unsteady, most of the queries result in additions or growths, hence requiring $O(\mathrm{N_{cell}})$ direct integrations. In the HCCI test case, the system is unsteady but rather homogeneous, which explains that, compared to direct integrations performed in every cells, the speed-up obtained with TDAC is a linear function of the number of cells (see Figure 5.5 where the values for the four mechanisms are normalized by the data of the mesh with 63 cells).

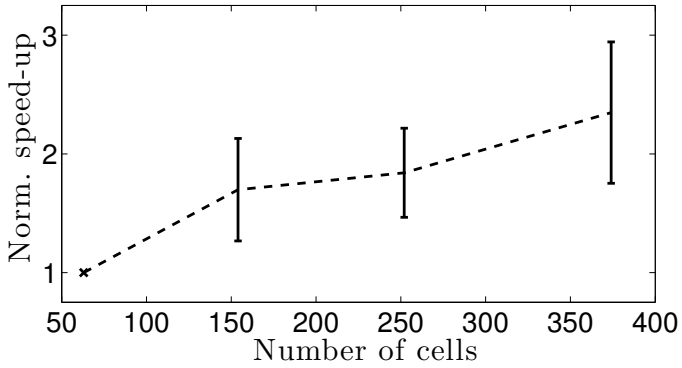

Figure 5.5: Range of speed-up for the four mechanisms normalized by the results obtained on the mesh with 63 cells. In these low inhomogeneity cases, the speed-up using TDAC is proportional to the number of cells.

The contribution of DAC is highlighted by the use of various mechanisms. In one cell, the direct integration of the reaction equations requires $O(\mathrm{N_s^2})$ operations. On the other hand, DAC requires $O(\mathrm{N_r})$ operations [96]. As the number of reactions is proportional to the number of species [106], the speed-up of the TDAC method is then proportional to $\mathrm{N_s}$ as shown in Figure 5.6. On this figure, the values are normalized by the results obtained on each mesh using the 44-species mechanism.

When ISAT and DAC are combined in TDAC, the achieved speed-

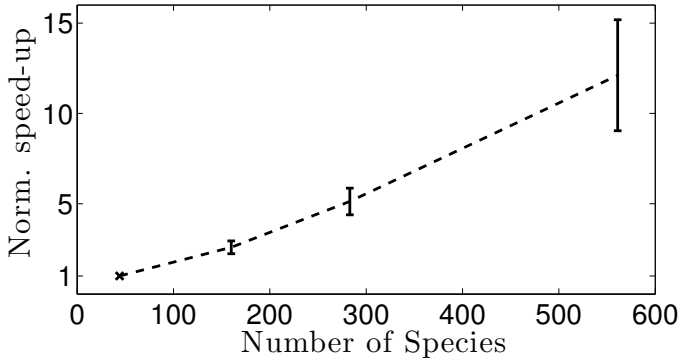

Figure 5.6: Range of speed-up for the four meshes normalized by the results obtained using the 44-species mechanism. The direct integration requires $O(N_s^2)$ operations while only $O(N_s)$ operations are needed by DAC. Accordingly, the speed-up factor of TDAC increases linearly with the number of species.

up factor is determined by the total number of retrievals, the number of species to be considered for each cell and the computational overheads required to dynamically reduce the chemical mechanism. This explains the similar performances between ISAT and TDAC when a low number of cells is used and the very high speed-up factors of TDAC with refined meshes and very complex mechanisms as it can be seen for the mesh with 374 cells, where the speed-up factor ranges from 9.6 with 44 species to 150 with 561 species (see Table 5.1).

In most HCCI cases, a value of $\mathrm{N_{ms}}$ between 0.5 and 1.0 crank angle degree (CAD) is sufficient to properly match the pressure trace computed with direct integration. Below these values, there is a very small impact on the error ε_p defined by:

$$\varepsilon_p = \frac{1}{K p_{max}} \sum_{i=1}^{K} |p_{i,\mathrm{TDAC}} - p_{i,\mathrm{DI}}| \ , \tag{5.9}$$

where K is the number of time steps, the pressures p are volume averaged over the whole domain and the subscript "max" denotes the maximum pressure during the whole simulation (see Figure 5.7a).

As described in the previous section, the use of $\mathrm{N_{mg}}$ reduces the total

number of growths. The optimal value for this configuration is around 20 where the total number of growths is reduced below 3000 compared to 5000 without N_{mg}. Very small values, however, dramatically increase the total number of growths (see Figure 5.7b). As the EOA is distorted either by growth from inhomogeneities in the same time-step or from rather homogeneous successive time-steps, the optimal value for N_{mg} mainly depends on the type of application. In HCCI simulations, this value is around 5% of the total number of cells.

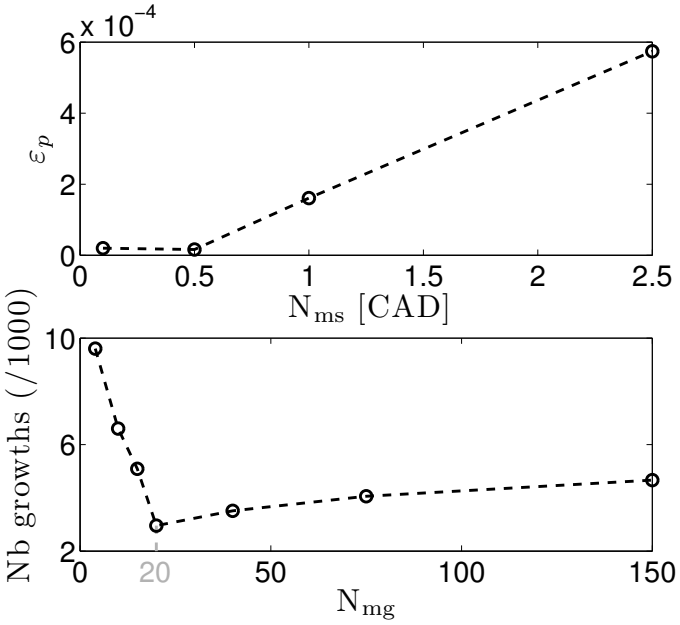

Figure 5.7: For the mesh with 374 cells and the 159-species mechanism, (a) mean error on the pressure ε_p as a function of N_{ms} and (b) total number of growths as a function of N_{mg}.

5.3.2 Experimental validation

The experimental validation has been performed with the extensive data on low load HCCI combustion obtained on a medium-duty diesel engine (displacement of 0.98 liters/cylinder) by Hessel et al. [81]. The mesh follows the specifications given by the authors: axi-symmetric with a

flat cylinder head, without valves, with a gasket and a crevice zone. The simulations use the detailed 857-species iso-octane mechanism of Curran et al. [104]. They are performed from inlet valve closing to exhaust valve opening. The temperature wall function of Han and Reitz [83] is used to compute the wall heat transfer and the RNG k-ε model modified by Han and Reitz [107] is used for the turbulence. Initial and boundary conditions for different equivalence ratios ϕ can be found in Table 5.2.

Table 5.2: Initial pressure, temperature, species mass fractions, and boundary temperature based on [81] for different equivalence ratios ϕ.

ϕ	0.12	0.16	0.20	0.24	0.28
p [bar]	1.367	1.361	1.378	1.377	1.371
T_{gas} [K]	467.8	468.6	464.1	465.0	463.2
T_{liner} [K]	381.4	382.4	383.5	384.4	385.3
T_{head} [K]	399.8	403.0	406.5	409.6	412.5
T_{piston} [K]	426.6	433.0	440.0	446.2	451.9
iC_8H_{18}	0.00759	0.01012	0.01265	0.01519	0.01774
O_2	0.22932	0.22824	0.22723	0.22633	0.22547
CO_2	0.00097	0.00157	0.00220	0.00250	0.00274
H_2O	0.00060	0.00073	0.00082	0.00092	0.00102
CO	0.00053	0.00034	0.00008	0.00003	0.00002

Compared to the previous chapter, the temperature wall function allows to reduce the number of cell to around 12000 at BDC (see the mesh in Figure 5.8).

The simulations were performed with a time-step of 0.05 CAD during the compression and expansion stroke and 0.025 CAD from -20 to 20 ATDC. The Courant number was below 0.1 for most of the cycle and peaked at 0.2 during combustion. The main requirement on the time-step is to precisely capture the combustion process which takes place within a few CAD.

For all simulated conditions, the agreement between the computed and experimental results are very good for both the auto-ignition time and the maximum cylinder pressure (see Figure 5.9).

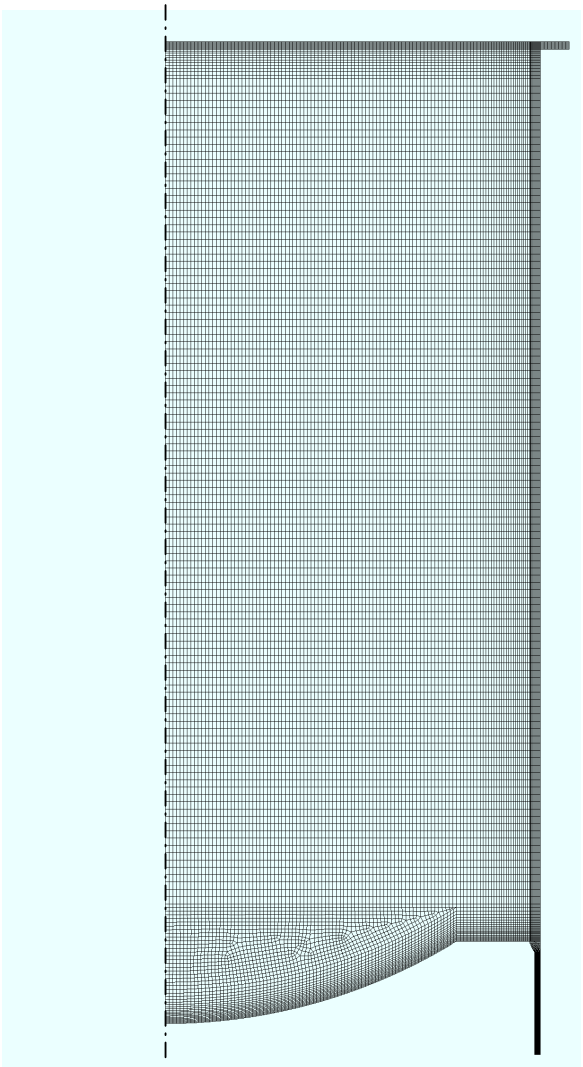

Figure 5.8: The engine geometry is represented by an axisymmetric mesh consisting of around 12000 cells at BDC.

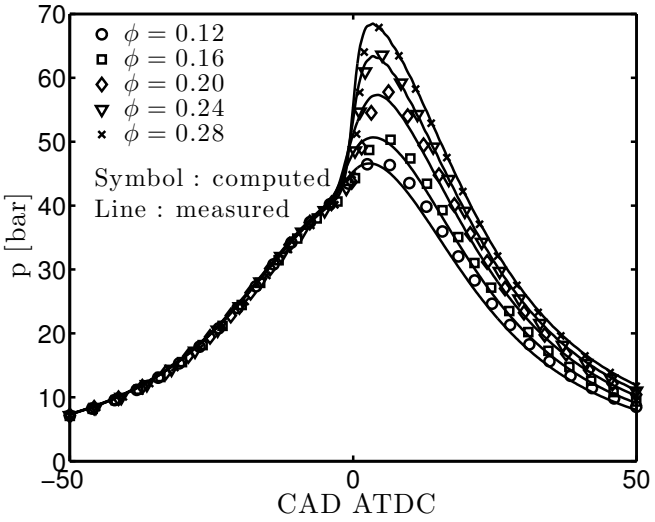

Figure 5.9: Pressure traces for computed (symbols) and measured (lines) [81] data of the HCCI engine cycle.

A rather good agreement is observed for the predicted emissions which slightly overestimates the unburned fuel and the CO to CO_2 conversion (see Figures 5.10a and 5.10b) while maintaining correct trends. The mechanism used for iso-octane oxidation kinetics has been extensively validated for a large range of combustion conditions. We have shown in the previous section that TDAC and direct integration of the system are in good agreement. These discrepancies are thus mainly due to the uncertainties on the wall temperature and the model assumptions for the crevices and the gasket regions (heat transfer, turbulence model, mesh refinements, ...) which are the main source of unburned hydrocarbons [108].

For single adiabatic cells, Liang et al. observed that, after the main combustion stage, the number of active species dropped to a value around 30, for the burned gas reactions [37]. In the present case, due to wall heat transfer, the conversion to burned gas is not complete near the wall and the algorithm retains more active species (around 250).

A higher number of cells, especially near the wall, corresponds to

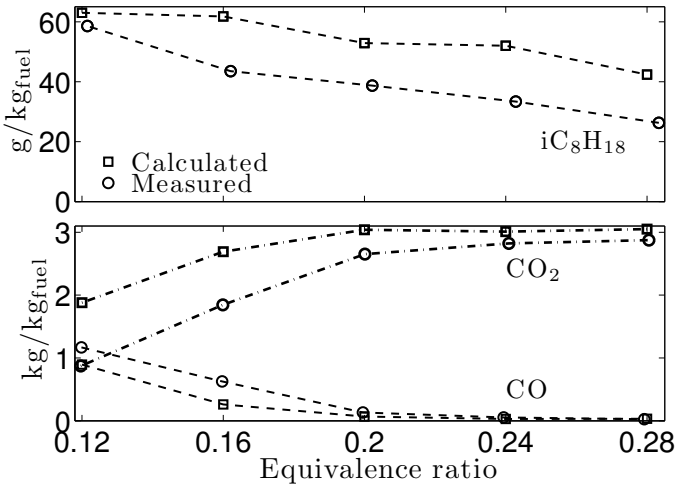

Figure 5.10: Engine emissions [81] data : (a) unburned fuel, and (b) CO_2 and CO as a function of the equivalence ratio.

an increase of the level of inhomogeneity, hence a more severe tolerance $\varepsilon_{\text{ISAT}}$ is required. A value of 10^{-4} is commonly used but lower values (around 10^{-5}) are required for more inhomogeneous cases. On practical meshes, the inhomogeneity is increased because of the required level of details, i.e. to model the heat transfer near the walls. Therefore, the efficiency of the ISAT algorithm is below what could be expected by extrapolating the results of Table 5.1.

The value of the speed-up factor for the real engine case, reported in the experimental validation, cannot be directly computed. It is approximated according to the average computational time required by direct integration for one cell, multiplied by the number of queries the solver would receive in the course of the simulation. For 4×10^7 queries and an average time of 2.4 s on a single CPU, the direct integration would require more than three years compared to 86 hours using TDAC. This approximation yields a more than 300-fold computational time reduction. This factor is well above what was previously reported for HCCI simulations using ISAT (up to 10 see [100]) and for single-cell simulations using DAC (between 15 to 70 depending on the mechanism [37, 95]).

5.4 Conclusion

A new method termed tabulation of dynamic adaptive chemistry (TDAC) which combines the advantages of ISAT and DAC has been developed. The principle of TDAC is to apply simplification methods on separate steps of the combustion calculation. These methods allow the speed-up to grow linearly with the number of species and the number of cells in the mesh. Even if the inhomogeneity observed in practical cases limits the speed-up due to less retrievals of the ISAT algorithm, a significant speed-up factor of about 300 is achieved compared to direct integration in the context of HCCI engine simulations. For this reason, TDAC represents a promising solution for CFD simulations including detailed mechanisms that are inconceivable using direct integration. The methodology can also be applied to the simulation of other combustion systems such as Diesel engines and gas turbine combustors.

CHAPTER 6

Comparative analysis of reduction methods within the TDAC framework

6.1 Introduction

The TDAC method has been introduced in the previous chapter. It consists of the coupling between a mechanism reduction method and a tabulation method. While the concept can be implemented with any of these methods, it has been first developed with the in-situ adaptive tabulation (ISAT) [40] and the dynamic adaptive chemistry (DAC) [37], which perform very well in engine applications [95, 100].

TDAC has been developed in the context of HCCI engines but it can be applied to other combustion systems, e.g. D'Errico et al. used it in CI engine simulations [109]. To further adapt this method to other combustion devices, an in-depth analysis of its inner mechanism is required.

This chapter presents the first step of this analysis by comparing different reduction methods within the TDAC framework. We selected five methods: directed relation graph (DRG) [17, 96], directed relation graph with error propagation (DRGEP) [24], path flux analysis (PFA) [25], dynamic adaptive chemistry (DAC) [37, 45], and element flux analysis (EFA) [38, 110]. Only EFA and DAC were specifically developed for the on-the-fly reduction. We have adapted the other methods to perform the mechanism reduction at runtime. These methods were selected because of their small computational overhead compared to more accurate methods based on Jacobian analysis (see Section 1.5). As in the previous chapter, the tabulation layer uses the ISAT method [40]. The

structure of the TDAC method is shown in Figure 6.1. We have implemented all methods into the Lib-ICE code based on the OpenFOAM® technology [92–94].

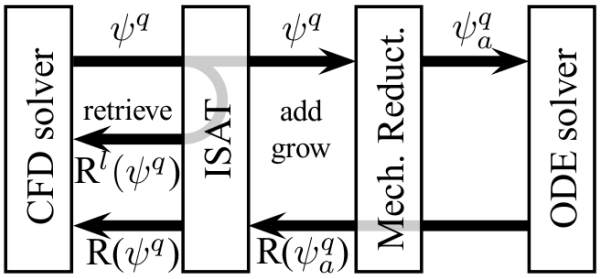

Figure 6.1: The TDAC method couples the ISAT method with one of the five selected mechanism reduction methods.

The objective of this chapter is to evaluate the efficiency of the five methods, and to identify key features that may benefit or penalize certain methods. While this study focuses on the reduction methods, their impact on the performance of ISAT is also evaluated.

6.2 Reduction methods

6.2.1 Directed Relation Graph

In the DRG method, Lu and Law are among the first to introduce a quantitative variable for the degree of coupling between two species in a mechanism [17]. This coupling is characterized by the impact of removing one species on the production rate of another species from the mechanism. The DRG method abstracts the couplings by constructing a graph with each node representing a species and each edge representing a strong coupling. Therefore, if an edge links species A to species B, the removal of species B induces a significant error on the production rate of species A.

To quantify the strength of the coupling, DRG uses the normalized contribution of species B to the production rate of species A:

$$r_{AB}^{\mathrm{DRG}} \triangleq \frac{\sum_{i=1}^{N_r} |\nu_{A,i}\omega_i\delta_{Bi}|}{\sum_{i=1}^{N_r} |\nu_{A,i}\omega_i|} , \tag{6.1}$$

$$\delta_{Bi} = \begin{cases} 1 & \text{if the } i\text{th elementary} \\ & \text{reaction involves species B,} \\ 0 & \text{otherwise,} \end{cases}$$

where N_r is the number of reversible elementary reactions, the subscript i designates the ith elementary reaction, $\nu_{A,i}$ is the net stoichiometric coefficient of species A in reaction i, and ω_i is the net production rate of reaction i

$$\omega_i = \omega_{fi} - \omega_{bi} . \tag{6.2}$$

In equation (6.2), ω_{fi} and ω_{bi} are the forward and backward reaction rates of reaction i given by

$$\omega_{fi} = k_{fi} \prod_{j=1}^{N_s} C_j^{\nu'_{ij}} , \tag{6.3}$$

$$\omega_{bi} = k_{bi} \prod_{j=1}^{N_s} C_j^{\nu''_{ij}} , \tag{6.4}$$

where the subscript j designates the jth species, N_s is the number of species, ν'_{ij} and ν''_{ij} are the forward and backward stoichiometric coefficients, respectively, C_j is the molar concentration, k_{fi} and k_{bi} are the forward and backward rate constants of reaction i. These rate constants are computed with the Arrhenius formulation:

$$k_{fi} = \left(A_i T^{n_i} e^{\frac{-E_i}{RT}} \right) F_i , \tag{6.5}$$

$$k_{bi} = \frac{k_{fi}}{K_{ci}} , \tag{6.6}$$

where A_i is the frequency factor, T is the temperature (with n_i the temperature exponent), E_i is the activation energy, F_i is a correction

term that includes the concentrations of the third body species, fall-off effects, and other special correction terms, and K_{ci} is the equilibrium constant. These parameters are provided in the kinetic mechanism.

The expression of the net production rate of a species A in the mechanism is given by

$$\dot{A} = \sum_{i=1}^{N_r} \nu_{A,i}\omega_i \ , \tag{6.7}$$

which is different from the production rate used in r_{AB}.

A large value of r_{AB}^{DRG} indicates that the removal of B induces significant error to the production rate of species A. Conversely, if r_{AB}^{DRG} is smaller than a user-defined tolerance ε, the coupling is deemed negligible and there is no edge from A to B.

Figure 6.2 shows a portion of an illustration graph constructed by the DRG method.

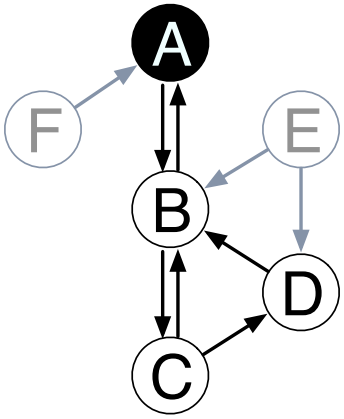

Figure 6.2: Given a starting species A, the species B, C and D are kept in the mechanism while E and F are removed.

The direction of the edges indicates the dependence of one species on another. For a starting species A that has to be kept, species B is also kept because of the strong dependence of A on B. Species C is also kept because of the interaction with B. Finally, species D is also included through the dependence of C on D. Even if species E and F are connected to at least one of the previous species, none of the species

kept have a strong dependence on them. They are therefore discarded.

The DRG method has been validated in many configurations such as autoignition in a constant volume, perfectly stirred reactor and jet-stirred reactor [17, 96]. This method has also been tested in the particular cases of partial equilibrium reactions, quasi steady state species and dormant mode.

We adapted the DRG method to reduce the mechanism at runtime instead of reducing it in a preprocessing step. It implies that when a species is deemed not important at a given time, it is not totally discarded but rather disabled. If a species is disabled since the beginning of the computation and has zero initial mass fraction, it is kept in the definition of the mechanism for subsequent reduction where it might be active, but neither its chemical source term nor its transport term is solved. If a species is disabled but has a non-zero mass fraction (this also includes inert species), only its transport term is solved. The disabled species still contribute to the reaction rates of active species through "third-body" reactions (see Section 1.4 in Chapter 1).

The reduction procedure derives a locally comprehensive mechanism by first computing the contribution coefficients r_{AB}^{DRG} using equation (6.1). Then it uses a set of initial species and recursively includes the group of dependent species using a depth-first search algorithm to traverse the graph. The starting set usually consists of the fuel, CO and HO_2, which play primary roles in the three major combustion processes of hydrocarbon fuels: fuel decomposition, CO oxidation and H_2/O_2 reactions, respectively. Finally, it disables the reactions that involves disabled species, except if these species are only used as a "third-body" in the reaction.

If processed by an exhaustive search, the computation of r_{AB}^{DRG} for every pairs of species would require N_s^2 evaluations of equation (6.1). Each of these evaluations contains $O(N_r)$ multiplications, which would overall involves $O(N_s^2 N_r)$ operations. Since $N_r \approx \alpha N_s$, with α generally around 5 (see Figure 1.6 in Chapter 1), this leads to a $O(N_s^3)$ complexity, which is more expensive than the computation of the Jacobian. However, another procedure allows to compute the r_{AB}^{DRG} more efficiently [96]. It takes advantage of the sparsity of the stoichiometric coefficient

matrices, i.e. each elementary reaction only involves a small number of species (typically below 6), and most of the species are only connected to few others. The procedure therefore loops through all reactions and evaluates the contribution to the coefficients of each species pair involved in each reaction. The number of operations is therefore $O(N_r)$ which corresponds to $O(N_s)$.

The pseudo code of the modified DRG method is presented in Appendix C.

6.2.2 Directed Relation Graph with Error Propagation

The directed relation graph with error propagation (DRGEP) method is based on the DRG method, but Pepiot-Desjardins and Pitsch introduced a finer selection of the species by considering that the influence of a species is damped as it propagates along the graph to reach another species [24].

The DRGEP method postulates that a species that is far from the search initiating set has a smaller effect. Therefore, the strength of the path from species B to species A of the search initial set is given by

$$R_{AB}^{\mathrm{DRGEP}} = \max_{\text{all paths p}} r_{AB,p}^{\mathrm{DRGEP}} \ , \tag{6.8}$$

where

$$r_{AB,p}^{\mathrm{DRGEP}} = \prod_{i=1}^{n-1} r_{S_i S_{i+1}}^{\mathrm{DRGEP}} \ , \tag{6.9}$$

with $S_1 = A$ and $S_n = B$. In the DRGEP method, the definition of the contribution coefficients is similar to DRG but is modified to solve some of the issues introduced by the error propagation, e.g. quasi steady state species (see [24] for more details and other examples):

$$r_{AB}^{\mathrm{DRGEP}} \triangleq \frac{\left| \sum_{i=1}^{N_r} \nu_{A,i} \omega_i \delta_{Bi} \right|}{\max(P_A, C_A)} \ , \tag{6.10}$$

where the production rate P_A and the consumption rate C_A of species

A are given by

$$P_A = \sum_{i=1}^{N_r} \max(0, \nu_{A,i}\omega_i) \ , \tag{6.11}$$

$$C_A = \sum_{i=1}^{N_r} \max(0, -\nu_{A,i}\omega_i) \ . \tag{6.12}$$

In equation (6.10), only the net contribution of species B to species A is considered, it indicates how the removal of species B modifies the net production rate of species A. It is also based on the observation that removing a species that contributes only to the consumption or the production of species A has not the same effect as removing a species that contributes similarly to the consumption and production of A. For the same value of r_{AB}^{DRG}, the error on the net production rate of A in the first case is more important than in the second case, because the production rate is compensated when removing a similar term in the consumption and production sides.

Figure 6.3 shows a portion of an illustration mechanism where the values of the r_{AB}^{DRGEP} are indicated on the arrows. Two paths are leading from species A to species B but the path through species M_1 has the greater strength and is used in equation (6.8).

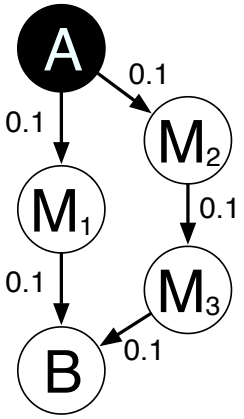

Figure 6.3: Portion of an illustration mechanism with the values of r_{AB}^{DRGEP} indicated on the edges. Given a starting species A, the connection to species B is characterized by the stronger path through M_1.

The selection procedure of DRG can be reformulated to compare it to DRGEP. It can be seen as removing a species B from the mechanism when the strength of the path leading to the search initiating set of species is below a user-defined tolerance. This strength is defined as

$$R_{AB}^{\mathrm{DRG}} = \max_{\text{all paths p}} r_{AB,p}^{\mathrm{DRG}} \ , \tag{6.13}$$

where

$$r_{AB,p}^{\mathrm{DRG}} = \min_{i=1}^{n-1} r_{S_i S_{i+1}} \ , \tag{6.14}$$

This definition illustrates that the DRG method characterizes the path strength by its weakest link, equation (6.14), instead of the damping introduced by the DRGEP method, equation (6.9).

Pepiot-Desjardins and Pitsch also introduced the group-based contribution coefficients. This concept includes the impact of the removed species on the subsequent removal. Equation (6.10) becomes

$$r_{AB,\{S\}}^{\mathrm{DRGEP}} \triangleq \frac{\left| \sum_{i=1}^{N_r} \nu_{A,i} \omega_i \delta_{Bi,\{S\}} \right|}{\max(P_A, C_A)} \ , \tag{6.15}$$

where $\{S\}$ is the set of species already removed and $\delta_{Bi,\{S\}}$ is unity if the ith reaction involves B or any species in subset $\{S\}$, and 0 otherwise (see [24] for illustration of this concept).

This method has been thoroughly validated in various configurations [24]. We have adapted it to reduce the mechanism at runtime. Similarly to the DRG method, it first computes r_{AB}^{DRGEP} using equation (6.10). Starting from the initial species, it inspects recursively the other species with a depth-first search algorithm and computes R_{AB}^{DRGEP} using equation (6.8). Among the species that should be disabled, i.e. with $R_{AB}^{\mathrm{DRGEP}} < \varepsilon$, where ε is a user-defined tolerance, it sorts the R_{AB}^{DRGEP} and removes a portion of these species with the lowest values. Then, it reevaluates the contribution coefficients using equation (6.15) and iteratively removes another portion of the remaining species with the lowest R_{AB}^{DRGEP}. In this study, the r_{AB}^{DRGEP} were reevaluated every 100 removals

to mitigate the impact on the overhead. Finally, as in the DRG method, the reactions that involve disabled species are removed.

Instead of performing the complete sorting of the R_{AB}^{DRGEP}, which requires at least $O(N_s \log(N_s))$ operations, we have also modified the method to perform a partial sort based on the heapsort algorithm [99], which requires $O(N_s \log(M))$ to sort the M species with lowest values.

As in DRG, the starting set usually consists of the fuel, CO and HO_2. However, in the original DRGEP method, unlike the DRG method, the species in the initial set are selected according to the combustion status. The processes, that involve the initial species, occur at different combustion stages. Including all initial species throughout the simulation could increase the computational time by including other species that have a minor effect at this stage. For example, during the post-ignition stage at high temperature, a major part of the fuel has been decomposed into smaller molecules and only CO oxidation and H_2/O_2 reactions dominate the overall reactivity. Keeping all initial species would lead to non-optimal skeletal mechanisms. Moreover, when the chemical system has shifted to produce CO_2 and H_2O, none of these species are optimal. Because in DRGEP, the set of initial species is selected dynamically, CO_2 and H_2O are also included as potential candidates. To identify the conditions where a specific initial species is meaningful, the contribution of each initial species to the system reactivity is quantified. The contribution of species S is then evaluated by

$$\alpha_{a,S} = \max_{\text{all atoms a}} \frac{N_{a,S}|P_S - C_S|}{P_a} \ . \tag{6.16}$$

where P_a is the atom production rate given by

$$P_a = \sum_{j=1}^{N_s} N_{a,S_j} \max(0, P_{S_j} - C_{S_j}) \ , \tag{6.17}$$

a is an element of the system (here C, H, O and N are considered), N_{a,S_j} is the number of atoms a in species S_j, and P_{S_j} and C_{S_j} are the production and consumption rate of species S_j given by equations (6.11) and (6.12), respectively. The conservation of elements imposes that the corresponding consumption rate of atom a is equal to P_a.

If $\alpha_{a,S}$ is below a user-defined tolerance, the species is removed from the set of initiating species. This is a modified definition of the one introduced in the original DRGEP method, because of the dynamic reduction formulation. In the original definition, $\alpha_{a,S}$ is normalized by its maximal value over all sample points and is used as a scaling factor for R_{AB}^{DRGEP}. Here, as the reduction is performed at runtime, $\alpha_{a,S}$ is only used to keep or discard species from the initial set. If $\alpha_{a,S}$ is below the tolerance for all initial species, only the species with the highest $\alpha_{a,S}$ is used.

More advanced reduction methods are also used in the original DRGEP method [24]. However, they involve the use of additional reduction layers, which are beyond the scope of this study (see Chapter 7).

The pseudo code of the modified DRGEP method is presented in Appendix C.

6.2.3 Path Flux Analysis

The path flux analysis (PFA) method [25] is based on the DRG method but, unlike DRG and DRGEP, it has been developed to take into account the production and the consumption fluxes instead of the level of interactions between species.

While, the total production and consumption fluxes of a species are calculated by (6.11) and (6.12), the flux of species A related with species B can be calculated as:

$$P_{AB} = \sum_{i=1}^{N_r} \max(\nu_{A,i}\omega_i\delta_{Bi}, 0) \ , \tag{6.18}$$

$$C_{AB} = \sum_{i=1}^{N_r} \max(-\nu_{A,i}\omega_i\delta_{Bi}, 0) \ . \tag{6.19}$$

To introduce the flux information Sun et al. defined a new contribution coefficient that includes both direct links (first generation) and indirect links through a third species (second generation) [25]. These links could be extended to any number of generations, but the computational cost increases exponentially with this number. Therefore, above two generations, this method induces too much overhead to be used at

runtime.

The contribution coefficients of first generation for production and consumption of species A via species B are defined as:

$$r_{AB}^{P-1st} = \frac{P_{AB}}{\max(P_A, C_A)} \ , \tag{6.20}$$

$$r_{AB}^{C-1st} = \frac{C_{AB}}{\max(P_A, C_A)} \ . \tag{6.21}$$

By using the production and consumption fluxes of the first generation, the contribution coefficients of second generation which are the measures of flux ratios between A and B via a third reactant M_i are defined as:

$$r_{AB}^{P-2nd} = \sum_{M_i \neq A,B} \left(r_{AM_i}^{P-1st} r_{M_iB}^{P-1st} \right) \ , \tag{6.22}$$

$$r_{AB}^{C-2nd} = \sum_{M_i \neq A,B} \left(r_{AM_i}^{C-1st} r_{M_iB}^{C-1st} \right) \ . \tag{6.23}$$

As suggested by Sun et al., these coefficients are aggregated in

$$r_{AB}^{\mathrm{PFA}} \triangleq r_{AB}^{P-1st} + r_{AB}^{C-1st} + r_{AB}^{P-2nd} + r_{AB}^{C-2nd} \ , \tag{6.24}$$

and compared to a user-defined threshold similarly to DRG and DRGEP.

To illustrate this aspect, Figure 6.4 shows a portion of a mechanism where the value of the species flux is indicated on the arrows. For the initial species A, the PFA method first selects species M_1, M_2, M_3, and B because of the species flux between A and B, whereas the DRG and DRGEP methods first select species C because of the link strength.

On one hand, the PFA method is more accurate than DRG and DRGEP because it reproduces the reaction path flux and thereby the overall combustion. On the other hand, the second generation significantly increases the computational cost. This implies that for a given error, the PFA method has to derive a smaller mechanism to balance the computational overhead of the reduction method.

This method has been validated for ignition delay, flame structure

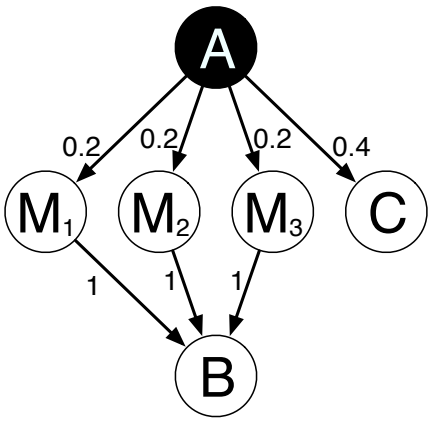

Figure 6.4: The PFA method reduces the mechanism based on species flux (indicated on the edges). Given an initial species A, it rather selects species M_i and B, whereas DRG and DRGEP prefer species C because of the link strength.

and propagation, and has been adapted to reduce the mechanism at runtime. It proceeds similarly to the previous methods by looping through all reactions to compute the contribution coefficients of first and second generations. Then, it starts from a search initiating set of species (same as in DRG) and recursively includes the species with r_{AB}^{PFA} above a user-defined tolerance. Finally, it discards the reactions that involve disabled species.

The pseudo code of the modified PFA method is presented in Appendix C.

6.2.4 Dynamic Adaptive Chemistry

This method has been described in the previous chapter and follows the same reduction procedure. However, new developments regarding the selection of initial species have been added to the method based on the work of Shi et al. [45].

In the original DAC scheme [37], fuel, CO, and HO_2 were selected to initiate the selection procedure. As described in the DRGEP method, these species do not equally contribute to the system reactivity throughout the simulation. Unlike the DRGEP method, the selection of the

initial species is based on two progress variables to quantify the combustion status. The first variable is the progress equivalence ratio that has been extensively used in multi-grid approach to group cells with similar combustion characteristics [39]:

$$\phi = \frac{(2-z')\sum\limits_{j=1,N_s}^{S_j\neq \mathrm{CO_2}} Y_{S_j} N_{C,S_j} + \frac{1}{2}\sum\limits_{j=1,N_s}^{S_j\neq \mathrm{H_2O}} Y_{S_j} N_{H,S_j}}{\sum\limits_{j=1,N_s}^{S_j\neq \mathrm{CO_2},\mathrm{H_2O}} Y_{S_j} N_{O,S_j} - z' \sum\limits_{j=1,N_s}^{S_j\neq \mathrm{CO_2}} Y_{S_j} N_{C,S_j}}\,, \tag{6.25}$$

where Y_{S_j} is the mass fraction of species S_j, N_{C,S_j}, N_{H,S_j}, and N_{O,S_j} denotes the number of atoms C, H, and O, in species S_j, and z' defines the proportion of fuel oxygen to fuel carbon (z' is zero for hydrocarbon fuels without oxygen). The definition of the progress equivalence ratio excludes the combustion products CO_2 and H_2O, as indicated by the superscripts of the sum in ϕ.

This equivalence ratio gives no information on the degree of fuel decomposition. Therefore, another variable is introduced by Shi et al.:

$$\phi_l = \frac{2\sum\limits_{j=1,N_s}^{N_{C,S_j}\geqslant 3} Y_{S_j} N_{C,S_j} + \frac{1}{2}\sum\limits_{j=1,N_s}^{N_{C,S_j}\geqslant 3} Y_{S_j} N_{H,S_j}}{\sum\limits_{j=1,N_s}^{N_{C,S_j}\geqslant 3} Y_{S_j} N_{O,S_j} + 2\,Y_{\mathrm{O_2}}}\,, \tag{6.26}$$

where subscript l represents all large hydrocarbons (more than 3 carbon atoms), and O_2 is the only oxidizer considered. As the combustion proceeds, the fuel decomposes and ϕ_l always decreases no matter what initial conditions are specified, which is not the case for ϕ (see [45] for illustration of these variables).

Shi et al. have shown that for both rich and lean conditions, when ϕ_l is below 0.001, the fuel can be removed from the search initiating set. At this threshold value, the combustion has already shifted from fuel decomposition to the oxidation of small hydrocarbons and H_2-CO.

When both ϕ_l and ϕ are below 0.001, the combustion process is

nearly completed and the initial set only includes CO_2 and H_2O.

This improved method has been applied by Shi et al. to a 2D HCCI engine case. The reported speed-up factor was around 9 using a detailed mechanism for n-heptane (543 species and 2538 reactions) [45].

The pseudo code of this version of the DAC method is presented in Appendix C.

6.2.5 Element Flux Analysis

The element flux analysis (EFA) method [38, 110] is based on the atomic fluxes between species. The reduction procedure only includes the species, considered as sources or sinks, that have a major contribution to the overall flux of elements. It is based on the observation that a small portion of the source-sink pairs can capture most of the element fluxes and thereby the system reactivity. In many conditions, less than 10% of the source-sink pairs are required to capture 99% of the element fluxes [110].

To quantify these fluxes, the EFA method uses the instantaneous elemental flux of atom a between species A and B through reaction i, which has been defined by Revel et al. [111], and further improved by He et al. [110] to solve issues with quasi-steady state species:

$$\dot{a}_{AB,i} = (|\omega_{fi}| + |\omega_{bi}|)\frac{N_{a,A}N_{a,B}}{N_{a,i}} \ , \tag{6.27}$$

where ω_{fi} and ω_{bi} are the forward and backward reaction rates given by equations (6.3) and (6.4)[1], $N_{a,A}$ and $N_{a,B}$ is the number of atoms a in species A and species B, respectively, and $N_{a,i}$ is the total number of atoms a in reaction i.

The total instantaneous flux between A and B is then defined by

$$\dot{a}_{AB} = \sum_{i=1}^{N_r} \dot{a}_{AB,i}\delta_{AB,i} \ , \tag{6.28}$$

[1] In the original EFA method, the reaction rates are given in (mol/s). To be consistent with the previous methods, we use here the reaction rates in mol/(cm^3.s).

$$\delta_{AB,i} = \begin{cases} 1 & \text{if the } i\text{th elementary reaction} \\ & \text{involves the source-sink pair A-B,} \\ 0 & \text{otherwise.} \end{cases}$$

Instead of identifying active species like in the previous methods, the EFA method identifies active source-sink pairs by sorting their atomic fluxes and keeping pairs up to a user-defined cutoff proportion of the overall element flux. The union set of species in the retained source-sink pairs composes the skeletal mechanism. Reactions are removed in the same way as for the other methods.

The original EFA method has been developed to reduce the mechanism at runtime. We have however modified the procedure by considering not only the carbon flux but the fluxes of all other elements (H, O and N). Preliminary tests have shown that using carbon flux does not allow to keep primary radicals such as OH and HO_2, which would require additional arbitrary selection. Moreover, the cutoff value has to be respected for all elements separately. Tests have shown that, when aggregated, the flux for all elements does not allow to select the major species and simulation errors are large even when the cutoff value is increased to include more flux. Because a small portion of the source-sink pairs contribute greatly to the system, we have also modified the sorting step by recursively applying a partial sort of 5% of these pairs, instead of a complete sort.

The pseudo code of the modified EFA method is presented in Appendix C.

6.3 Computational setup

The methods described in the previous section were compared on a simplified test case. It consists of a simple engine geometry with 85 mm bore and 88 mm stroke (displacement volume $V_d = 499$ cm^3). This geometry is represented by an axisymmetric mesh with 1350 cells (see Figure 6.5). The mesh topology is not modified during the simulation. As can be seen in Figure 6.5, the mesh is fairly coarse because the objective of this chapter is not to capture the details of the fluid dynamics but rather

to have a simple and representative test case so that the methods can also be compared to the results obtained by the direct integration of the ODE system. In this case, to get the results in a workable time, the simulations were performed on 16 central processing units (CPU). The cells were distributed among the CPU with the Metis algorithm to minimize communication between processors [112]. Tests for this configuration gives a scale-up factor of 12.5 compared to the simulation on a single CPU.

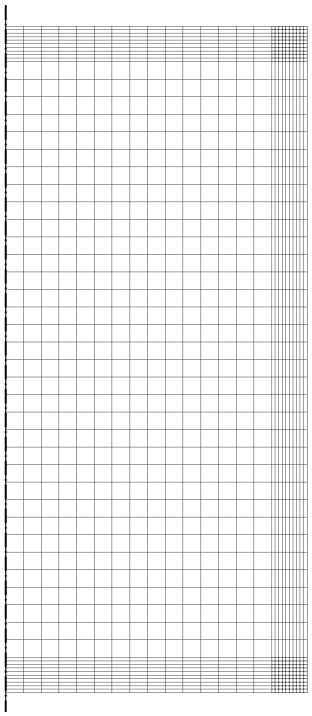

Figure 6.5: The simplified geometry of the engine combustion chamber (V_d=499 cm^3) is represented by an axisymmetric mesh consisting of 1350 cells.

In addition to the inhomogeneity introduced in the previous chapter by the wall heat transfer, we used artificially inhomogeneous initial conditions for the equivalence ratio and the temperature (see Figure 6.6). The use of these conditions increases the computational cost. As a comparison, it is five times slower than an adiabatic case with homoge-

neous initial conditions (with lower initial temperature to have the same ignition timing) and 10% more expensive than initial homogeneous conditions with wall heat transfer. Using an inhomogeneous case with wall heat transfer is thus the most critical case to analyze the performance of the method.

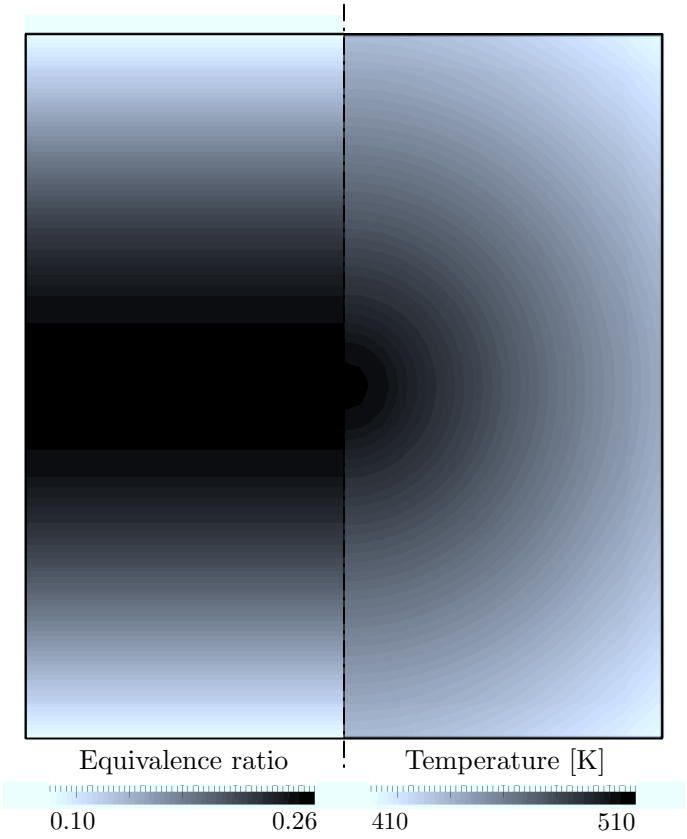

Figure 6.6: Inhomogeneous initial conditions were specified for the equivalence ratio (from 0.10 to 0.26) and the temperature (410 to 510 K).

The ISAT method was configured with a tolerance of 10^{-4}, $N_{ms} = 1$, $N_{mg} = 400$, and the maximum number of leafs stored in the tree was limited to 500.

The fuel used in the simulations was iso-octane and its combustion was modeled by the third version of the mechanism from Lawrence Liv-

ermore National Laboratory, which includes 874 chemical species and 3796 elementary reactions [21, 22].

The simulations were performed for the whole compression and expansion stroke (from -180 to 180 CAD ATDC).

As in the previous chapter, the solver used to integrate the system of ODE is based on the semi-implicit mid-point rule developed by Bader and Deuflhard [102].

6.4 Results

The computational time using direct integration on 16 CPU is 270 hours. Based on the scale-up tests, this corresponds to 140 days if performed on one CPU. The speed-up factors presented in the following results are the ratios of this computational time and the computational times of TDAC using each reduction method. The results are also compared with those using only ISAT on the full mechanism. This simulation took 220 hours on one CPU. The speed-up factor is thus 15 compared to the direct integration.

Depending on the number of active species, the memory size of the leafs stored in the ISAT binary tree and the other processing variables required between 1.5 GB and 4 GB.

The test case has been solved using the five reduction methods over a large range of tolerance. The mean number of species retained in the mechanism monotonically decreases when the tolerance increases, until not enough species are included in the mechanism to properly model the combustion. In this case, significant error and aberrant results were observed.

To compare the reduction methods to the direct integration, we have computed the impact of changing the tolerance of these methods on the error of various parameters. Because the tolerance of each method is not based on the same definition, we have used the mean number of species kept in the mechanism during the entire cycle as a common measure of this tolerance. We first focus on the pressure and the overall reaction rates. Then, we analyze the error on the mass fraction of the major species.

There are complex interactions with ISAT, which lead to variability in the results but also to some artifacts (e.g. increasing the number of species may increase the error for very small level of error). In the following figures, the variability is represented by confidence intervals illustrated by grey rectangles.

The error $err(Z)$ on $p_{\max}$, $\mathrm{HRR}_{\max}$ and MPRR, where Z is one of these three parameters, is defined by

$$err(Z) = \frac{|Z - Z_{\mathrm{ref}}|}{Z_{\mathrm{ref}}}, \tag{6.29}$$

where Z_{ref} is the corresponding reference value obtained by direct integration.

Because CA50 is a crank angle position, which is a relative value, it cannot be compared to the reference CA50 in the same way as equation (6.29). Therefore, the error on CA50 is defined as

$$err(\mathrm{CA50}) = \frac{|\mathrm{CA50} - \mathrm{CA50}_{\mathrm{ref}}|}{\mathrm{CA90}_{\mathrm{ref}} - \mathrm{CA10}_{\mathrm{ref}}}, \tag{6.30}$$

where CA90 and CA10 are the crank angles where 10 and 90% of the heat is released and CA90−CA10 is a measure of the combustion duration.

The errors on MPRR, $p_{\max}$, $\mathrm{HRR}_{\max}$, and CA50 are illustrated in Figures 6.7, 6.8, 6.9, and 6.10 by using arbitrarily the PFA, DRGEP, DRG, and EFA methods, respectively (the other results are presented in Appendix D). The maximum error selected for this illustration is 5% for CA50, $\mathrm{HRR}_{\max}$ and MPRR, whereas for $p_{\max}$ it has been set to 0.5%.

The range of speed-up factors and of the mean number of active species corresponding to these levels of error are presented in Table 6.1 for the five methods. The errors generally remain small when the mean number of species is above 100. Below this value, they greatly increase until the simulations are no longer possible because of meaningless results. This increase is exponential except for CA50 (see Figure 6.9). CA50 is mainly determined by the ignition timing and the combustion

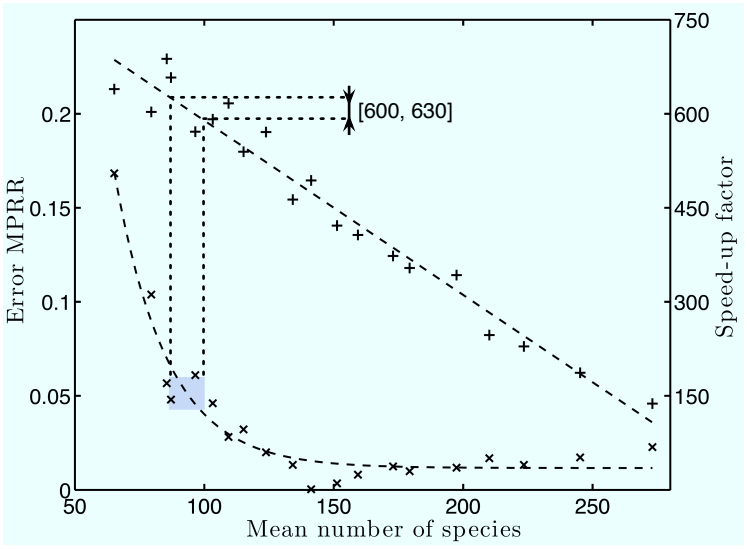

Figure 6.7: Error (left axis) on MPRR and speed-up (right axis) for the PFA method.

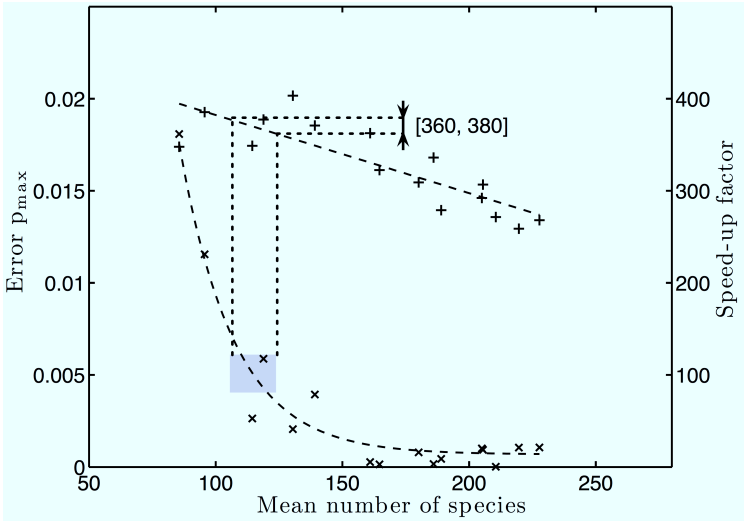

Figure 6.8: Error (left axis) on p_{max} and speed-up (right axis) for the DRGEP method.

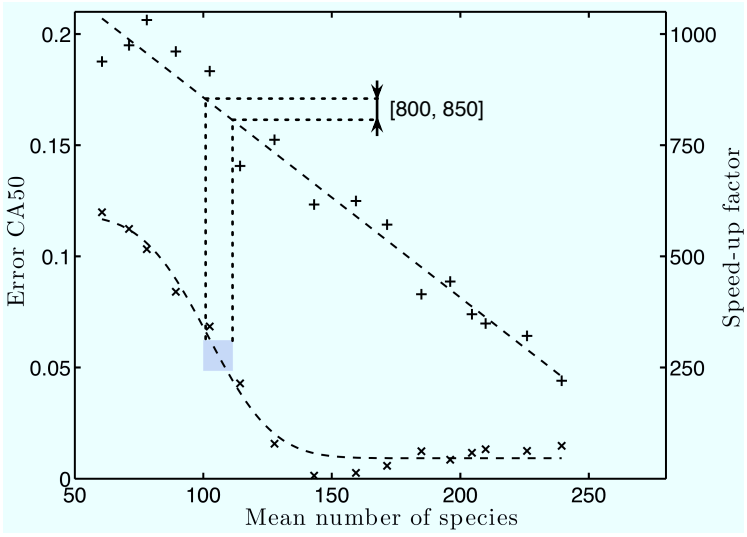

Figure 6.9: Error (left axis) on CA50 and speed-up (right axis) for the DRG method.

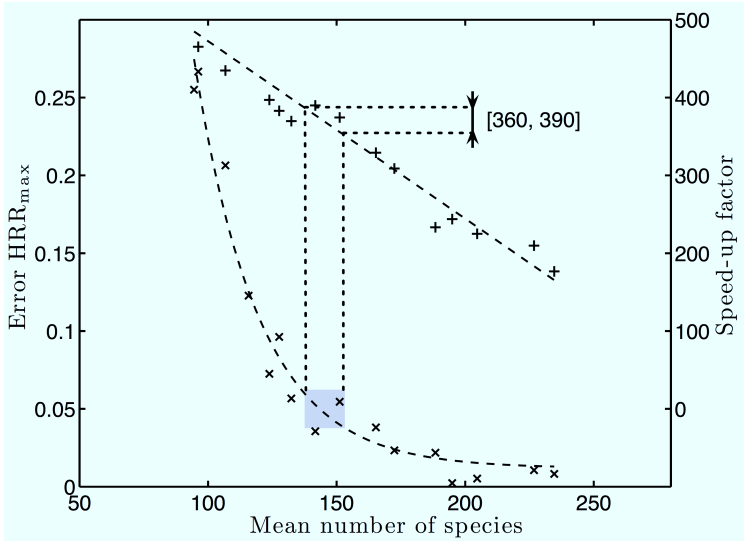

Figure 6.10: Error (left axis) on HRR_{max} and speed-up (right axis) for the EFA method.

duration. The non-linear dependence of both characteristics on the temperature and the pressure varies according to the active species. This implies that, at the highest errors, given an incremental error on the other parameters, the effect on CA50 is damped. In other words, the effect of a difference in CA50 on the other combustion parameters increases exponentially.

Table 6.1: Ranges of mean number of active species and speed-up for the five reduction methods with given error requirements on MPRR, p_{max} HRR_{max} and CA50.

		MPRR, 5% error	p_{max}, 0.5% error	HRR_{max}, 5% error	CA50, 5% error
mean active species	DRG	[90, 105]	[100, 110]	[85, 100]	[100, 115]
	DRGEP	[95, 110]	[105, 125]	[85, 95]	85[a]
	PFA	[90, 95]	[95, 105]	[85, 95]	[85, 95]
	DAC	70[b]	[95, 105]	70[b]	[105, 115]
	EFA	[135, 150]	[150, 160]	[135, 150]	[115, 125]
speed-up	DRG	[835, 895]	[815, 850]	[850, 915]	[800, 850]
	DRGEP	[375, 385]	[360, 380]	[385, 395]	395[a]
	PFA	[600, 620]	[575, 600]	[600, 630]	[600, 630]
	DAC	870[b]	[750, 775]	870[b]	[705, 755]
	EFA	[360, 390]	[330, 350]	[360, 390]	[420, 440]

[a] There is no clear trend for the error on CA50 using the DRGEP method, however the errors are mostly below 5%.

[b] The error on MPRR and HRR_{max} for the DAC method is always smaller than the given error, the maximum speed-up and the minimum mean number of active species are therefore indicated.

As mentioned in Chapter 3, there is a negative correlation between MPRR and CA50. Similarly, HRR_{max} and p_{max} are partly determined by CA50. The same correlations are not observed for the errors on these parameters, because they can compensate each other, e.g. a shorter ignition delay can be compensated by a longer combustion duration.

The DAC and DRG methods perform very well for MPRR and HRR_{max} while they require slightly more species to meet the error requirements on p_{max} and CA50. They both give the best speed-up factor, 915 and 870, respectively.

The EFA method requires on average more species for a given error. The definition of this method includes too many species during the main combustion and not enough before and after this event (see Figure 6.11). Therefore, because the auto-ignition strongly depends on the pre-ignition reaction steps, a higher mean number of species is required to reach the critical number of species before ignition. In addition to this effect, the speed-up of this method is significantly smaller than that of DRG and DAC because the EFA method changes the number of species more than the other methods, which has a detrimental effect on the performance of ISAT (see Figure 6.12). To retrieve a stored solution, the ISAT method relies on region of accuracy. In TDAC, this method has been implemented so that the dimension of these regions can increase to include other species. However, when the difference of species is too large, the chance of being out of the region increases, which decreases the proportion of retrievals and increases the proportion of growths.

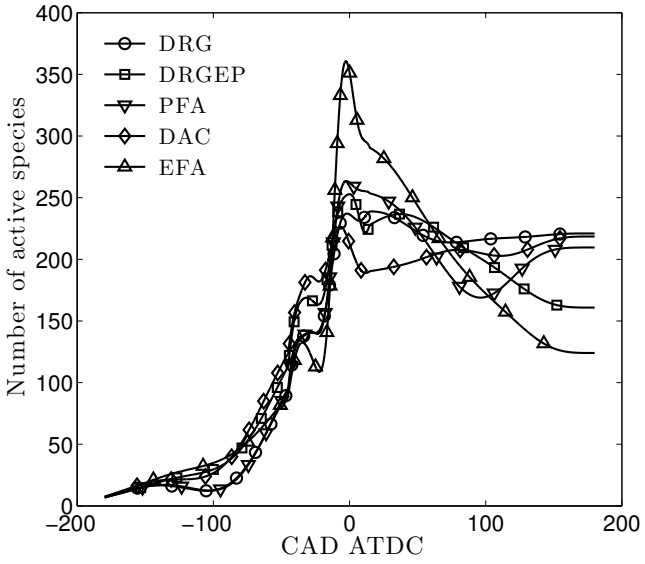

Figure 6.11: Evolution of the number of species for a given mean value of the number of species kept in the mechanism. The numbers of species is smoothed with a Butterworth low pass band filter for clarity.

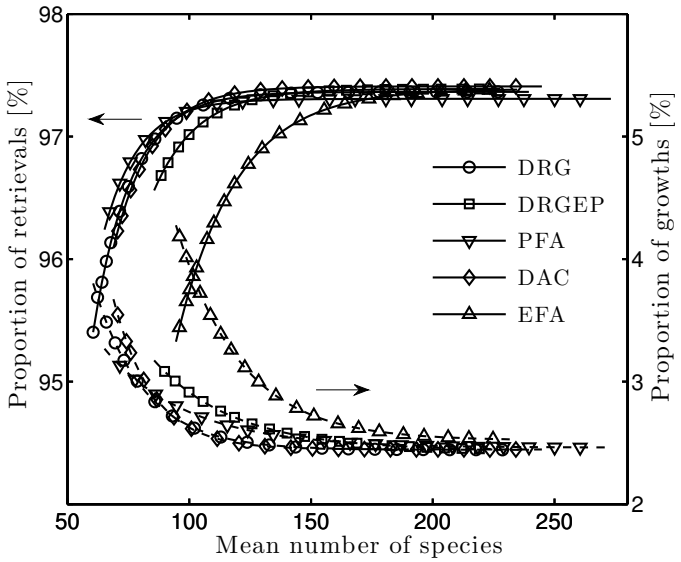

Figure 6.12: Proportion of retrieval and growth as a function of the mean number of active species for the five methods.

In Figure 6.12, it can also be seen that the definition of the DRGEP method has also a detrimental effect on the performance of ISAT, which added to the overhead of this method, that includes the group-based approach, explains its lower speed-up factor.

While the PFA method requires on average less species than the other methods, it has a slightly lower speed-up, around 600. This can be explained by the higher overhead of this method but also by the slightly higher number of species included during the main combustion (see Figure 6.11).

Figure 6.13 shows the corresponding pressure and rate of heat release around TDC using TDAC with the DRGEP method (the other methods perform similarly for the given errors). TDAC is in very good agreement with the results using the direct integration and ISAT.

The errors on the species mass fractions have been evaluated on three major species: iC_8H_{18} (the fuel), CO_2, and H_2O. Compared to the previous parameters, the error $\mathrm{err}(Y_S)$ on the mass fraction Y_S of species S is here integrated on a portion of the cycle:

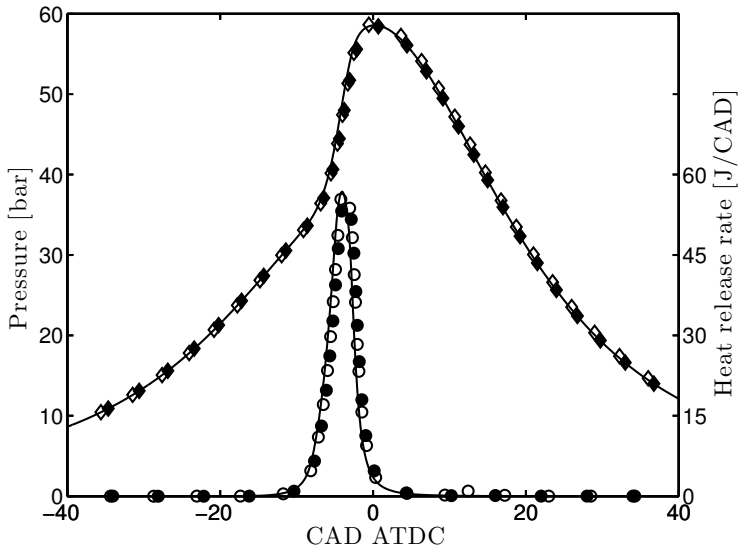

Figure 6.13: Pressure (circles) and rate of heat release (diamonds) for direct integration (solid lines), ISAT (filled symbols) and TDAC using the DRGEP method (empty symbols; mean number of species around 100).

$$\mathrm{err}(Y_S) = \sqrt{\frac{1}{\Delta\theta}\int_{\theta_1}^{\theta_2}\left(\frac{Y_{S,\mathrm{ref}}(\theta) - Y_S(\theta')}{\bar{Y}_{S,\mathrm{ref}}}\right)^2 \mathrm{d}\theta}\ , \tag{6.31}$$

where θ is the crank angle, $\theta_1 = -15$, $\theta_2 = 10$ CAD ATDC and $\Delta\theta = 25$ CAD are set to include the portion of cycle where there is a significant change in these species, $Y_{S,\mathrm{ref}}$ is the reference mass fraction of species S and $\bar{Y}_{S,\mathrm{ref}}$ is the mean reference mass fraction in the interval between θ_1 and θ_2. In this definition, Y_S is evaluated in $\theta' = \theta - \theta_{\mathrm{shift}}$, where θ_{shift} is the crank angle difference between the peaks of heat release rate, instead of θ to avoid including the error on the ignition time. This definition is a modified version of the one introduced in [113].

The errors on iC_8H_{18}, H_2O, and CO_2 are illustrated in Figures 6.14, 6.15 and 6.16 by using arbitrarily the DAC, PFA, and EFA methods, respectively (the other results are presented in Appendix D). The maximum value selected for this illustration is 5% for CO_2 and H_2O, whereas for the fuel it has been set to 2%.

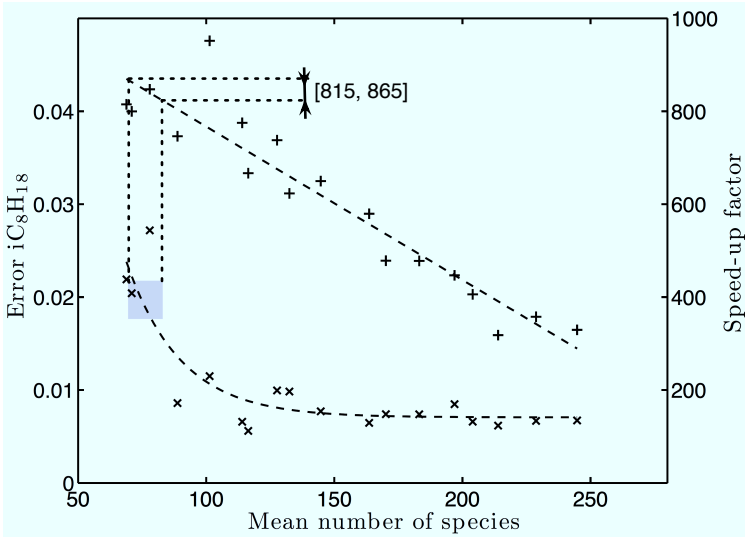

Figure 6.14: Error (left axis) on the fuel (iC_8H_{18}) mass fraction based on equation (6.31) and speed-up (right axis) for the DAC method.

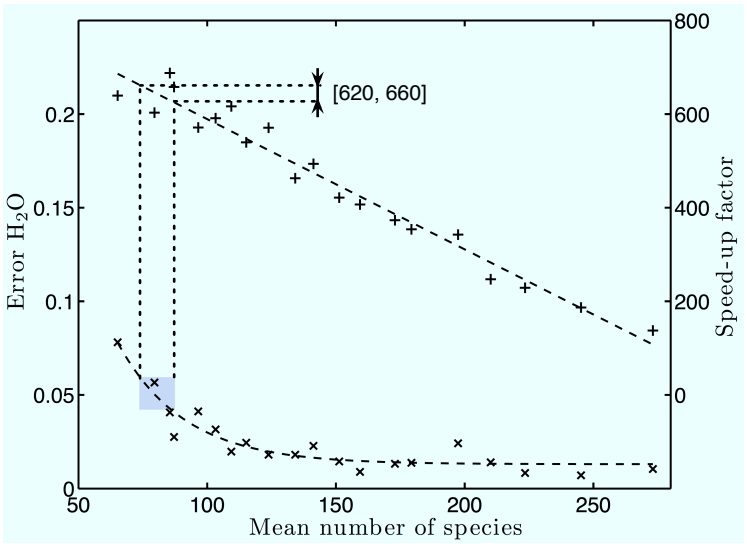

Figure 6.15: Error (left axis) on H_2O mass fraction based on equation (6.31) and speed-up (right axis) for the PFA method.

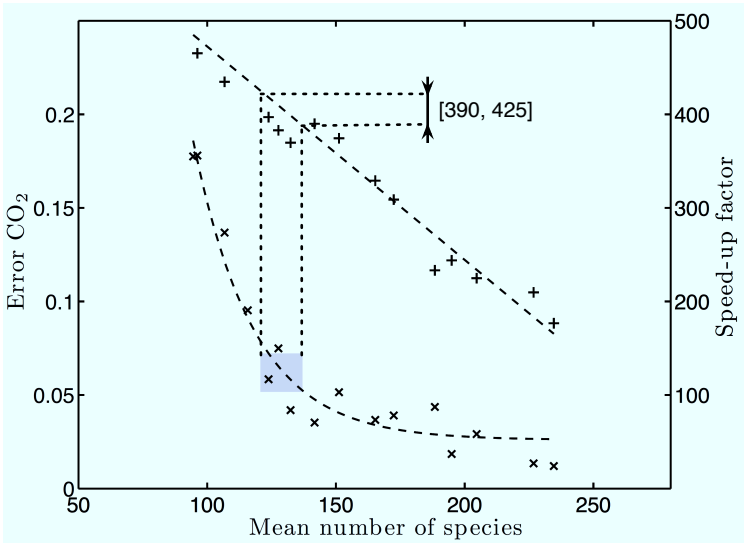

Figure 6.16: Error (left axis) on CO_2 mass fraction based on equation (6.31) and speed-up (right axis) for the EFA method.

The range of speed-up corresponding to the given errors on these major species is shown in Table 6.2 for the five methods.

Table 6.2: Ranges of mean number of active species and speed-up for the five reduction methods with given error requirements on the mass fractions of iC_8H_{18}, CO_2 and H_2O.

		iC_8H_{18}, 2% error	CO_2, 5% error	H_2O, 5% error
mean active species	DRG	[125, 135]	[85, 95]	[85, 95]
	DRGEP	[90, 100]	[110, 120]	[110, 120]
	PFA	[120, 130]	[90, 105]	[85, 100]
	DAC	[70, 85]	[90, 100]	[95, 110]
	EFA	[150, 175]	[120, 135]	[120, 135]
speed-up	DRG	[700, 750]	[870, 920]	[875, 925]
	DRGEP	[380, 390]	[365, 375]	[365, 375]
	PFA	[505, 540]	[580, 610]	[590, 625]
	DAC	[815, 865]	[760, 800]	[740, 780]
	EFA	[300, 360]	[390, 425]	[390, 425]

For each method, the observed errors on H_2O and CO_2 have similar trends, which confirms that both combustion products are handled similarly even if they belong to different part of the mechanism. This can be explained by the choice of initial species that includes both parts, for the DRG, DRGEP, PFA, and DAC methods. For EFA, which does not rely on an initial set of species, this illustrates that a strong element flux goes to these species.

The error requirement for the fuel is more difficult to meet for the PFA, DRG and EFA methods, while it is near its maximal speed-up value for the DRGEP and DAC methods. This can be explained by the error propagation formulation of these two methods which keeps the stronger path connecting the fuel, present in the initial set, to the other species. This is also illustrated in Figure 6.11, where DRGEP and DAC include on average 20-25% more species during the pre-ignition for a given mean number of species on the full cycle. This higher number of species allows to describe more accurately the decomposition of the fuel.

Like for the previous parameters, the DRG method performed better on average than the other methods with a speed-up factor around 900. For the fuel, the DAC method outperformed DRG with a speed-up factor of 850 while for DRG, it falls to 725.

The species evolution around TDC is illustrated in Figure 6.17. This figure compares the results using the direct integration, ISAT and TDAC. The results of TDAC are obtained by using the DAC method with settings so that the error limit is respected for every species, i.e. mean number of species is slightly below 100. They are in very good agreement with the reference data. The other reduction methods performed equally well for the given errors. While the error analysis focused on the major species, Figure 6.17 also shows that the minor or intermediate species (OH, HO_2 and CO) are in very good agreement with the reference, without the need to further reduce the tolerance. The small discrepancy observed for CO after the main combustion is mainly due to the ISAT settings.

Figure 6.18 shows the number of active species as a function of the

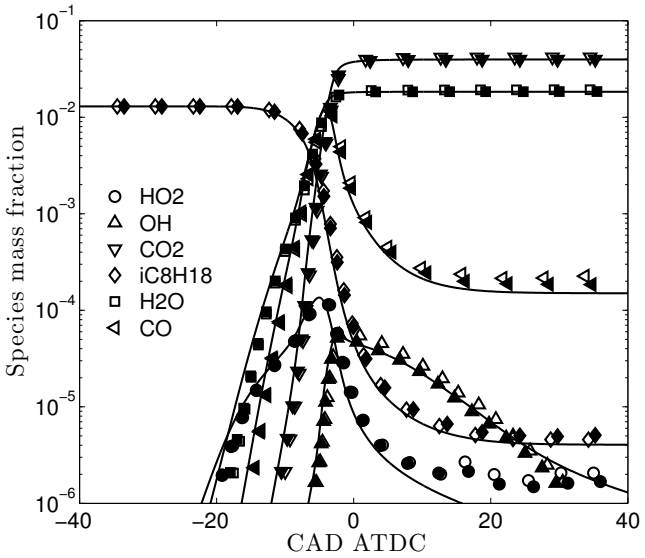

Figure 6.17: Species mass fraction for direct integration (solid lines), ISAT (filled symbols) and TDAC using the DAC method (empty symbols; mean number of species around 100).

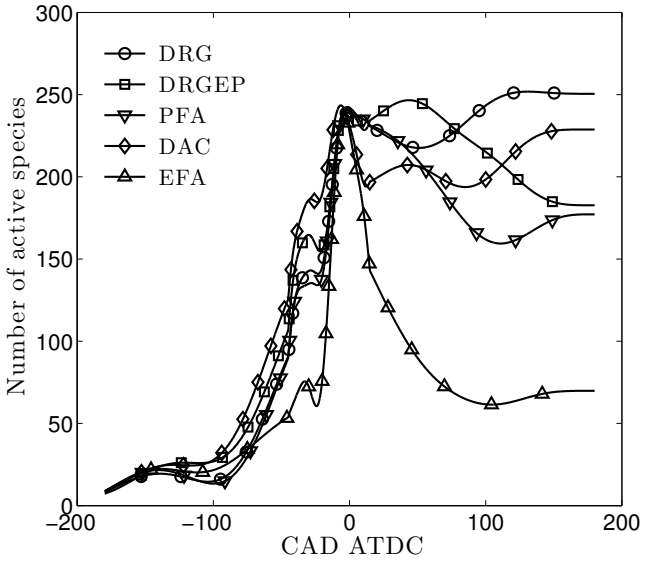

Figure 6.18: Evolution of the number of species for a given maximum value of the number of species kept in the mechanism during the entire cycle. The numbers of species is smoothed with a Butterworth low pass band filter for clarity.

crank angle for the five methods. The tolerances of these methods have been selected so that the maximum number of species during the main combustion step are similar. As can be seen in this figure, the definition of the EFA methods strongly affects the evolution of the number of species included in the mechanism compared to the other methods. This number remains lower than that of the other methods during the whole pre-ignition process and decreases rapidly after the main ignition. As mentioned above, the lower number in the pre-ignition explains the larger error on the fuel. However, the lower number after the main ignition may be beneficial to the computational time since the reactivity strongly decreases after this event, thereby less species should be included. In the other methods, it can be seen that this number remains high. This is due to their definition based on a search initiating set which include a bigger number of species even if the overall reactivity of the system decreases.

For the EFA method, the lowest mean number of species before meaningless results is higher than the other methods. Issues mainly arise after the main ignition step, which indicates that, for a given mean value, the number of species at the end of the combustion, when the reactivity strongly decreases, is too low to properly describe the system. Therefore, this important decrease may also be detrimental because it requires to decrease the tolerance in order to maintain a critical number of species after the main ignition.

The two main differences between DAC and DRGEP is the selection of the initial species and the group-based approach. The selection approach of DRGEP greatly decreases the mean number of species at the end of the cycle because only one of the species remains, whereas DAC shifts from HO_2 and CO to H_2O and CO_2, which still connects a greater number of species and explains the slight increase at the end of the cycle. The group-based formulation increases the overhead of the DRGEP method without contributing to the quality of the results. As mentioned above, the combination of both aspects in DRGEP has a negative impact on the performance of ISAT.

While the complexity of the semi-implicit ODE solver is $O(N_s^2)$, the speed-up factor observed in the previous figures decreases linearly with

the mean number of species because the tabulation layer mostly determines the computational time by retrieving previously computed solutions. The tabulation has a $O(N_s)$ complexity, which explains this trend. However, for the highest tolerances, leading to the lowest mean numbers of species, the speed-up generally stops increasing at the same rate. This can be explained by the lower proportion of retrievals and the higher proportion of growths in ISAT (see Figure 6.12). This trend is observed for every method, even if, as mentioned above, the EFA method only reaches the same level as the others for the lowest tolerances.

6.5 Conclusion

The DRG and DAC methods globally perform very well with low errors and speed-up factors around 900 and 800, respectively. This is significantly higher than the speed-up of ISAT alone or those reported by any other method used to include detailed mechanisms in internal combustion engine simulations.

The definitions of the EFA and DRGEP method led to lower retrievals and higher growths in ISAT, hence decreasing the performance of the tabulation layer. This had a major impact on the overall speed-up factors using these two methods, which are significantly lower than DRG and DAC. We have shown that the significant decrease of the number of species in the post-ignition step for EFA leads to meaningless results and requires smaller tolerances. However, the other methods include too many species in this step and they could therefore take advantage of this feature. This should be further investigated to combine the positive effects of all methods.

The PFA method performed globally well, but is slightly less effective than DRG and DAC because of its higher overhead and the greater number of species during the main combustion.

A significant complexity lies in the coupling between these reduction methods and the tabulation method: the species included by some definitions reduced the performance of ISAT; the impact of the changing number of species on the region of accuracy of the stored solutions is not trivial; and the tolerances of one layer partly determines the perfor-

mance of the other layer. A better comprehension of their interactions should remain the focus of future studies.

CHAPTER 7

Conclusion and perspectives

In the first part of this thesis, we have analyzed experimentally the main ethyl esters resulting from the reaction of the volatile fatty acids produced by the acidogenesis route with ethanol. We have first shown that these fuels, i.e. ethyl acetate (EtAc), ethyl propionate (EtPr), and ethyl butyrate (EtBu), can be used in HCCI on a large range of equivalence ratios. We have investigated how the HCCI operating zone and the combustion characteristics are modified by these fuels compared to ethanol. Within the esters, EtBu ignited first, followed by EtPr and EtAc, but all three were more resistant to auto-ignition than ethanol. For given inlet conditions, the better timing of EtBu and EtPr increased the higher limit of the operating zone while maintaining the lower limit. The ignition of EtAc was so delayed that the instability at lower equivalence ratios increased, which affected the lower limit. However, this also smoothed the pressure gradient at higher loads and increased the higher limit.

To use the ethyl esters from the acidogenesis route without additional processes, which further alter their nature or proportion, we have also investigated tri-component blends of EtAc, EtPr, and EtBu in the range of concentrations that is generally encountered at the output of the overall process. This study has shown that the combustion characteristics were mainly determined by the proportion of EtAc and EtBu and nearly insensitive to the proportion of EtPr. Also, there was a antagonistic effect between EtPr and the other two products. This resulted in a “dilution” effect, which reduced the variation of the combustion

characteristics for higher proportion of EtPr.

Many challenges remain for the successful implementation of these products, and to bring them out of the lab. First, the full range of products obtained by the biochemical process has to be investigated. It includes esters produced from minor organic acids but also esters produced by combining volatile fatty acids with glycerol (co-product of the biodiesel production). This will allow to select the fermentation parameters such that the more suitable ranges of products are produced. Second, we noticed that the required inlet temperature was higher than in common engine configurations. EtBu ignited first and was therefore the most suitable product if we wanted to decrease this parameter, but, another option may also be to blend the esters with ignition promoters such as n-heptane or dimethyl ether.

In the second part of this thesis, we have addressed the issue of using kinetic mechanisms to model the combustion in CFD simulations. In the context of HCCI engine simulations, we have first developed a simple method that allows to reduce detailed mechanisms with an iterative procedure and a 0D model. We combined this method with a new definition of the HCCI operating limits to compute the operating zone of iso-octane and ethyl acetate based on simulation results.

The use of this method becomes tedious when the number of species increases. Therefore, we developed a second method to automatically handle large mechanisms at runtime. This method, named tabulation of dynamic adaptive chemistry (TDAC), couples a tabulation method with a mechanism reduction method. It performs particularly well thanks to the real synergy between the two constitutive layers. On one hand, the tabulation avoids computing the reduction and the solution of the ODE system when a previous solution can be retrieved. On the other hand, the mechanism reduction method reduces the computational time of solving the ODE system and of handling the tabulation step. Compared to the direct integration of the detailed mechanism, this method is in very good agreement and achieves a speed-up factor of up to 900, which is significantly more than what has been reported by other techniques. This is one of the first fully functional methods that allow to include

detailed mechanisms in engine simulations without the need to rely on massively parallel infrastructures.

While this method has been first investigated for HCCI, its main concepts have a more general application for all reacting flow computations. The objective is therefore to continue the development of the TDAC method for the simulations of compression ignition (CI) and spark ignition (SI) engines. Future studies should further analyze the behavior of the constitutive parts of the method and modify them accordingly to increase the versatility of TDAC.

As a first step, we have achieved in this thesis the comparison between five reduction methods. It has been shown that the DRG and the DAC methods are the most effective, but interesting features were also observed in the other methods. For example, the reduction of the number of species kept after the main combustion by EFA was a beneficial feature even if it led to greater errors when the tolerance was too high. Because all these methods are based, in a different way, on the construction of graphs with species being the node and edges characterizing the coupling between species, future improvements of these reduction methods should take advantage of graph-based approaches such as what is used in [114].

We noticed that the ISAT algorithm used for the tabulation layer could be further optimized for internal combustion engine cases. We have already introduced some improvements in the context of HCCI (see Chapter 5). However, future studies should focus on the particular conditions encountered in CI and SI engines.

To further improve the efficiency of TDAC, new layers can be added to the tabulation and mechanism reduction methods, similarly to what is proposed as a preprocessing technique by Lu and Law [18]. Examples of new layers are mostly based on time scale analysis but without the use of the Jacobian or only the use of the Jacobian of the reduced mechanism: the quasi-steady state assumption (QSSA) [29], stiffness removal [115] or hybrid multi time scale (HMTS) [116].

Finally, the use of TDAC on parallelized cases could lead to some numerical issues. Similarly to what was observed in ISAT by Lu et al. [117], discontinuities in the species mass fractions may appear at the

interface between processors. Future research should therefore focus on the solutions that can be applied in these cases.

Bibliography

[1] S. Onishi, S. H. Jo, K. Shoda, P. D. Jo, S. Kato, SAE Technical Paper 790501 (1979).

[2] M. Noguchi, Y. Tanaka, T. Tanaka, Y. Takeuchi, SAE Technical Paper 790840 (1979).

[3] P. M. Najt, D. E. Foster, SAE Technical Paper 830264 (1983).

[4] R. H. Thring, SAE Technical Paper 892068 (1989).

[5] H. Zhao (Ed.), HCCI and CAI engines for the automotive industry, Woodhead Publishing, 2007.

[6] F. Zhao, T. W. Asmus, D. N. Assanis, J. E. Dec, J. A. Eng, P. M. Najt, Homogeneous Charge Compression Ignition (HCCI) Engines, Key research and development issues, SAE, 2003.

[7] M. Christensen, A. Hultqvist, B. Johansson, SAE Technical Paper 1999-01-3679 (1999).

[8] J. H. Mack, S. M. Aceves, R. W. Dibble, Energy 34 (2009) 782–787.

[9] R. Kleerebezem, M. C. M. van Loosdrecht, Curr. Opin. Biotechnol. 18 (2007) 207–212.

[10] W. Parawira, M. Murto, J. S. Read, B. Mattiasson, J. Chem. Technol. Biotechnol. 79 (2004) 673–677.

[11] K. Lata, K. V. Rajeshwari, D. C. Pant, V. V. N. Kishore, World J. Microbiol. Biotechnol. 18 (2002) 589–592.

[12] A. S. Ucisik, M. Henze, Water Res. 42 (2008) 3729–3738.

[13] S. Bengtsson, J. Hallquist, A. Werker, T. Welander, Biochem. Eng. J. 40 (2008) 492–499.

[14] H. Chang, N.-J. Kim, J. Kang, C. Jeong, Biotechnol. Bioprocess Eng. 15 (2010) 1–10.

[15] F. Contino, S. Bacq, E. Fockedey, Etude de la création de la société GreenGold. Annexes techniques, Master's thesis, Université catholique de Louvain, 2006.

[16] C. K. Westbrook, W. J. Pitz, H. J. Curran, in: H. Zhao (Ed.), HCCI and CAI engines for the automotive industry, Woodhead Publishing, 2007.

[17] T. Lu, C. K. Law, Proc. Combust. Inst. 30 (2005) 1333–1341.

[18] T. Lu, C. K. Law, Prog. Energy Combust. Sci. 35 (2009) 192–215.

[19] M. Bastian, S. Heymann, M. Jacomy, Gephi: An open source software for exploring and manipulating networks. International AAAI conference on weblogs and social media, 2009.

[20] S. Liu, J. C. Hewson, J. H. Chen, H. Pitsch, Combust. Flame 137 (2004) 320–339.

[21] M. Mehl, W. J. Pitz, M. Sjöberg, J. E. Dec, in: SAE 2009 International Powertrains, Fuels and Lubricants Meeting, SAE Paper No. 2009-01-1806, Florence, Italy.

[22] M. Mehl, H. J. Curran, W. J. Pitz, C. K. Westbrook, in: 2009 European Combustion Meeting, Vienna, Austria.

[23] M. Singer, S. Pope, Combust. Theor. Model. 8 (2004) 361–383.

[24] P. Pepiot-Desjardins, H. Pitsch, Combust. Flame 154 (2008) 67–81.

[25] W. Sun, Z. Chen, X. Gou, Y. Ju, Combust. Flame 157 (2010) 1298–1307.

[26] T. Nagy, T. Turányi, Combust. Flame 156 (2009) 417–428.

[27] A. S. Tomlin, M. J. Pilling, T. Turányi, J. H. Merkin, J. Brindley, Combust. Flame 91 (1992) 107–130.

[28] A. Massias, D. Diamantis, E. Mastorakos, D. A. Goussis, Combust. Flame 117 (1999) 685–708.

[29] M. Smooke, N. Peters, Reducing mechanisms, volume 384, Springer Berlin / Heidelberg, pp. 48–67.

[30] S. S. Ahmed, F. Mauss, G. Moréac, T. Zeuch, PCCP 9 (2007) 1107–1126.

[31] A. Saylam, M. Ribaucour, W. J. Pitz, R. Minetti, Int. J. Chem. Kinet. 39 (2007) 181–196.

[32] T. Zeuch, G. Moréac, S. S. Ahmed, F. Mauss, Combust. Flame 155 (2008) 651–674.

[33] J. Y. Chen, W. Kollmann, R. W. Dibble, Combust. Sci. Technol. 64 (1989) 315–346.

[34] T. Turányi, Comput. Chem. 18 (1994) 45–54.

[35] F. C. Christo, A. R. Masri, E. M. Nebot, S. B. Pope, Symp. (Int.) Combust. 26 (1996) 43–48.

[36] O. Colin, A. Pires da Cruz, S. Jay, Proc. Combust. Inst. 30 (2005) 2649–2656.

[37] L. Liang, J. G. Stevens, J. T. Farrell, Proc. Combust. Inst. 32 (2009) 527–534.

[38] K. He, I. P. Androulakis, M. G. Ierapetritou, Ind. Eng. Chem. Res. 49 (2010) 10471–10478.

[39] A. Babajimopoulos, D. Assanis, D. Flowers, S. Aceves, R. Hessel, Int. J. Engine Res. 6 (2005) 497–512.

[40] S. B. Pope, Combust. Theor. Model. 1 (1997) 41–63.

[41] J. B. Bell, N. J. Brown, M. S. Day, M. Frenklach, J. F. Grcar, R. M. Propp, S. R. Tonse, Proc. Combust. Inst. 28 (2000) 107–113.

[42] U. Maas, S. B. Pope, Combust. Flame 88 (1992) 239–264.

[43] O. Gicquel, N. Darabiha, D. Thèvenin, Proc. Combust. Inst. 28 (2000) 1901–1908.

[44] Q. Tang, S. B. Pope, Proc. Combust. Inst. 29 (2002) 1411–1417.

[45] Y. Shi, L. Liang, H.-W. Ge, R. D. Reitz, Combust. Theor. Model. 14 (2010) 69–89.

[46] R. Edwards, V. Mahieu, J.-C. Griesemann, J.-F. Larivé, D. J. Rickeard, SAE Technical Paper 2004-01-1924 (2004).

[47] F. Cherubini, N. Bird, A. Cowie, G. Jungmeier, B. Schlamadinger, S. Woess-Gallasch, Resour. Conserv. Recy. 53 (2009) 434–447.

[48] H. Zhao, J. Li, T. Ma, N. Ladommatos, SAE Technical Paper 2002-01-0420 (2002).

[49] J. E. Dec, Proc. Combust. Inst. 32 (2009) 2727–2742.

[50] S. Tanaka, F. Ayala, J. C. Keck, J. B. Heywood, Combust. Flame 132 (2003) 219–239.

[51] N. Jeuland, X. Montagne, Oil & Gas Science and Technology - Rev. IFP 61 (2006) 85–94.

[52] P. Risberg, Describing the auto-ignition quality of fuels in HCCI engines, Ph.D. thesis, KTH, 2006.

[53] J. Zigová, E. Šturdík, J. Ind. Microbiol. Biotechnol. 24 (2000) 153–160.

[54] S. Fernando, S. Adhikari, K. Kota, R. Bandi, Fuel 86 (2007) 2806–2809.

[55] V. L. Gonçalves, B. P. Pinto, J. C. Silva, C. J. Mota, Catal. Today 133-135 (2008) 673–677.

[56] A. Jaecker-Voirol, I. Durand, G. Hillion, B. Delfort, X. Montagne, Oil & Gas Science and Technology - Rev. IFP 63 (2008) 395–404.

[57] F. Contino, H. Jeanmart, SAE Technical Paper 2009-01-0297 (2009).

[58] C. K. Westbrook, W. J. Pitz, P. R. Westmoreland, F. L. Dryer, M. Chaos, P. Osswald, K. Kohse-Höinghaus, T. A. Cool, J. Wang, B. Yang, N. Hansen, T. Kasper, Proc. Combust. Inst. 32 (2009) 221–228.

[59] S. M. Walton, M. S. Wooldridge, C. K. Westbrook, Proc. Combust. Inst. 32 (2009) 255–262.

[60] W. K. Metcalfe, C. Togbé, P. Dagaut, H. J. Curran, J. M. Simmie, Combust. Flame 156 (2009) 250–260.

[61] M. H. Hakka, H. Bennadji, J. Biet, M. Yahyaoui, B. Sirjean, V. Warth, L. Coniglio, O. Herbinet, P. A. Glaude, F. Billaud, F. Battin-Leclerc, Int. J. Chem. Kinet. 42 (2010) 226–252.

[62] L. Gasnot, V. Decottignies, J. Pauwels, Fuel 84 (2005) 505–518.

[63] M. Tazerout, O. L. Corre, P. Stouffs, SAE Technical Paper 1999-01-3509 (1999).

[64] S. Butterworth, Wireless Engineer 7 (1930) 536—541.

[65] M. Sjöberg, J. Dec, SAE Technical Paper 2004-01-1900 (2004).

[66] G. F. Hohenberg, SAE Technical Paper 790825 (1979).

[67] G. Woschni, SAE Technical Paper 670931 (1967).

[68] H. Soyhan, H. Yasar, H. Walmsley, B. Head, G. Kalghatgi, C. Sorusbay, Appl. Therm. Eng. 29 (2009) 541–549.

[69] G. T. Kalghatgi, R. A. Head, Int. J. Engine Res. 7 (2006) 215–236.

[70] Cosilab Software, Version 3.2.1, Rotexo-Softpredict-Cosilab GmbH & Co. KG, Germany, http://www.SoftPredict.com, 2010.

[71] P. Saxena, F. A. Williams, Proc. Combust. Inst. 31 (2007) 1149 – 1156.

[72] F. Contino, F. Foucher, C. Mounaïm-Rousselle, H. Jeanmart, Energ. Fuel 25 (2011) 998–1003.

[73] R. D. Snee, Technometrics 23 (1981) 119–130.

[74] N. Morgan, A. Smallbone, A. Bhave, M. Kraft, R. Cracknell, G. Kalghatgi, Combust. Flame 157 (2010) 1122–1131.

[75] A. Khuri, J. Cornell, Response surfaces: designs and analyses, Statistics, textbooks and monographs, Marcel Dekker, 1996.

[76] C. K. Law, Combustion Physics, Cambridge University Press, 2006.

[77] R. J. Kee, F. M. Rupley, J. A. Miller, Chemkin-II: A fortran chemical kinetics package for the analysis of gas phase chemical kinetics, Technical Report, Sandia National Laboratories, 1989.

[78] L. F. Shampine, M. W. Reichelt, SIAM J. Sci. Comput. 18 (1997) 1–22.

[79] J. A. Miller, C. F. Melius, Combust. Flame 91 (1992) 21–39.

[80] Gambit 2.4 User's Guide, ANSYS, 2007.

[81] R. P. Hessel, D. E. Foster, S. M. Aceves, M. L. Davisson, F. Espinosa-Loza, D. L. Flowers, W. J. Pitz, J. E. Dec, M. Sjöberg, A. Babajimopoulos, SAE Technical Paper 2008-01-0047 (2008).

[82] Fluent 6.3 User's Guide, ANSYS, 2006.

[83] Z. Han, R. D. Reitz, Int. J. Heat Mass Transfer 40 (1997/2) 613–625.

[84] B. F. Magnussen, Modeling of nox and soot formation by the eddy dissipation concept. International Flame Research Foundation, 1989.

[85] S. Hong, M. S. Wooldridge, D. N. Assanis, Proc. Combust. Inst. 29 (2002) 711–718.

[86] A. A. Amsden, P. J. O'Rourke, T. D. Butler, KIVA-II: A Computer Program for Chemically Reactive Flows with Sprays, Los Alamos National Laboratory, 1989.

[87] A. de Risi, T. Donateo, D. Laforgia, ASME-ICE 36 (2001) 53–64.

[88] M. Jia, M. Xie, Fuel 85 (2006) 2593–2604.

[89] S.-C. Kong, Y. Sun, R. D. Reitz, J. Eng. Gas Turbines Power 129 (2007) 245–251.

[90] C. K. Westbrook, W. J. Pitz, O. Herbinet, H. J. Curran, E. J. Silke, Combust. Flame 156 (2009) 181–199.

[91] F. M. C. Gauding, B. Kerschgens, A. Vanegas, H. W. Won, N. Peters, C. Hasse, SAE Technical Paper 2009-01-0720 (2009).

[92] H. Weller, G. Tabor, H. Jasak, C. Fureby, J. Comput. Phys. 12 (1998) 620–631.

[93] T. Lucchini, G. D'Errico, F. Brusiani, G. M. Bianchi, in: Proceedings of the COMODIA 2008 conference.

[94] G. D'Errico, D. Ettorre, T. Lucchini, SAE Int. Jou. of Fuel and Lubricants 1 (2009) 452–465.

[95] L. Liang, J. G. Stevens, S. Raman, J. T. Farrell, Combust. Flame 156 (2009) 1493–1502.

[96] T. Lu, C. K. Law, Combust. Flame 144 (2006) 24–36.

[97] L. Lu, S. B. Pope, J. Comput. Phys. 228 (2009) 361–386.

[98] S. B. Pope, Algorithms for Ellipsoids, Technical Report FDA-08-01, Cornell University, 2008.

[99] W. H. Press, S. A. Teukolsky, W. T. Vetterling, B. P. Flannery, Numerical Recipes: The Art of Scientific Computing, Cambridge University Press, third edition, 2007.

[100] M. Embouazza, D. C. Haworth, N. Darabiha, SAE Technical Paper 2002-01-2773 (2002).

[101] V. Kumar, M. Gavrilova, C. Tan, P. L'Ecuyer, I. Veljkovic, P. Plassmann, D. Haworth, A Scientific On-line Database for Efficient Function Approximation, volume 2667, Springer Berlin / Heidelberg, pp. 963–963.

[102] G. Bader, P. Deuflhard, Numer. Math. 41 (1983) 373–398.

[103] R. Seiser, H. Pitsch, K. Seshadri, W. J. Pitz, H. J. Gurran, Proc. Combust. Inst. 28 (2000) 2029–2037.

[104] H. J. Curran, P. Gaffuri, W. J. Pitz, C. K. Westbrook, Combust. Flame 129 (2002) 253–280.

[105] H. J. Curran, P. Gaffuri, W. J. Pitz, C. K. Westbrook, Combust. Flame 114 (1998) 149–177.

[106] C. K. Law, Proc. Combust. Inst. 31 (2007) 1–29.

[107] Z. Han, R. D. Reitz, Combust. Sci. Technol. 106 (1995) 267–295.

[108] J. B. Heywood, Internal Combustion Engine Fundamentals, McGraw-Hill, 1988.

[109] G. D'Errico, D. Ettorre, T. Lucchini, F. Contino, in: Multi-Dimensional Engine Modeling Meeting, SAE Congress, 2010.

[110] K. He, I. P. Androulakis, M. G. Ierapetritou, Chem. Eng. Sci. 65 (2010) 1173–1184.

[111] J. Revel, J. Boettner, M. Cathonnet, J. Bachman, Journal de chimie physique 91 (1994) 365–382.

[112] G. Karypis, V. Kumar, SIAM J. Sci. Comput. 20 (1998) 359–392.

[113] M. Valorani, F. Creta, D. A. Goussis, J. C. Lee, H. N. Najm, Combust. Flame 146 (2006) 29–51.

[114] K. He, M. G. Ierapetritou, I. P. Androulakis, Combust. Flame 155 (2008) 585–604.

[115] T. Lu, C. K. Law, C. S. Yoo, J. H. Chen, Combust. Flame 156 (2009) 1542–1551.

[116] X. Gou, W. Sun, Z. Chen, Y. Ju, Combust. Flame 157 (2010) 1111–1121.

[117] L. Lu, S. R. Lantz, Z. Ren, S. B. Pope, J. Comput. Phys. 228 (2009) 5490–5525.

APPENDIX A

Molecular structure of the major products obtained by the acidogenesis route

The following figures illustrate the molecular structure of the major ethyl and glyceryl esters presented in Chapter 1. Only one of the three isomers of the mono- and di- esters of glycerol are presented.

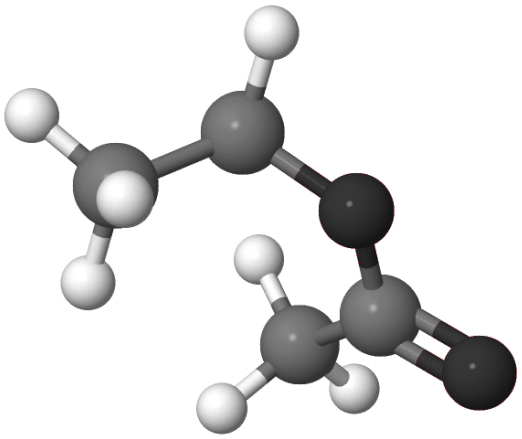

Figure A.1: Ethyl Acetate

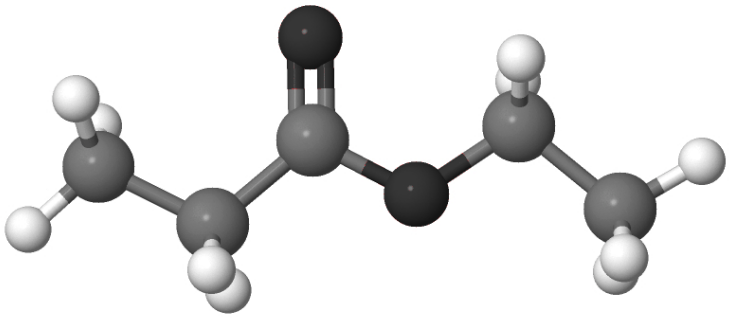

Figure A.2: Ethyl Propionate

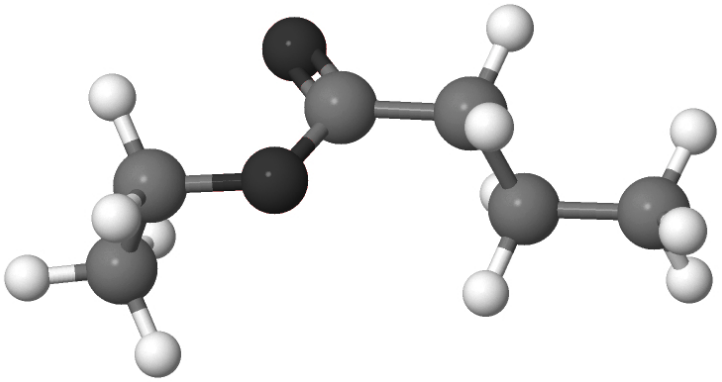

Figure A.3: Ethyl Butyrate

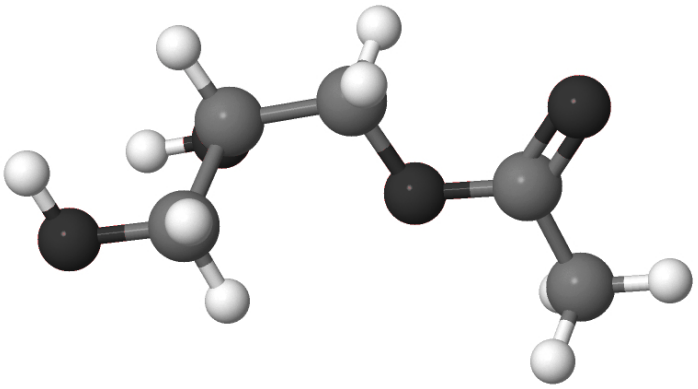

Figure A.4: Monoacetin

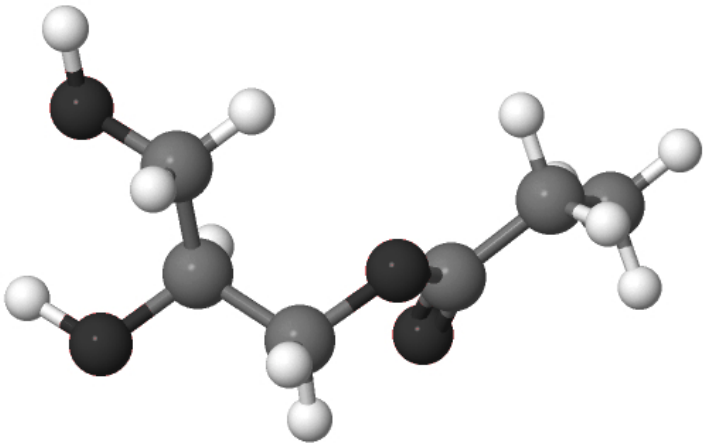

Figure A.5: Monopropionin

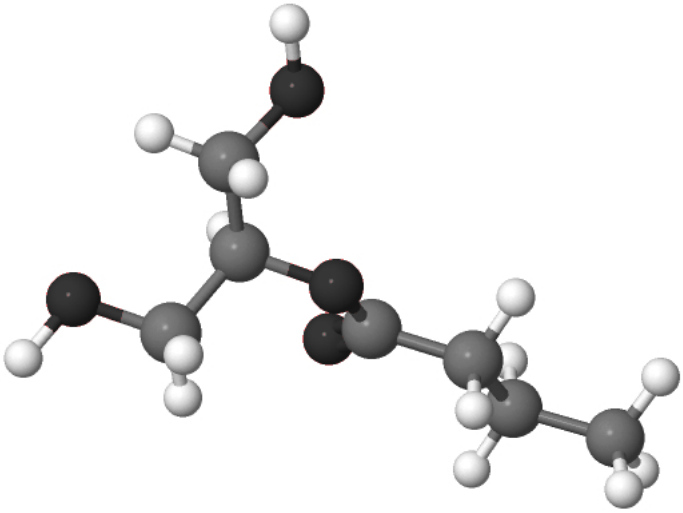

Figure A.6: Monobutyrin

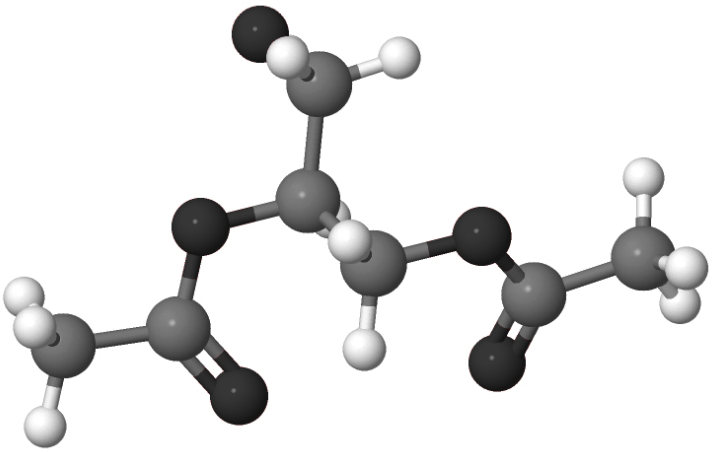

Figure A.7: Diacetin

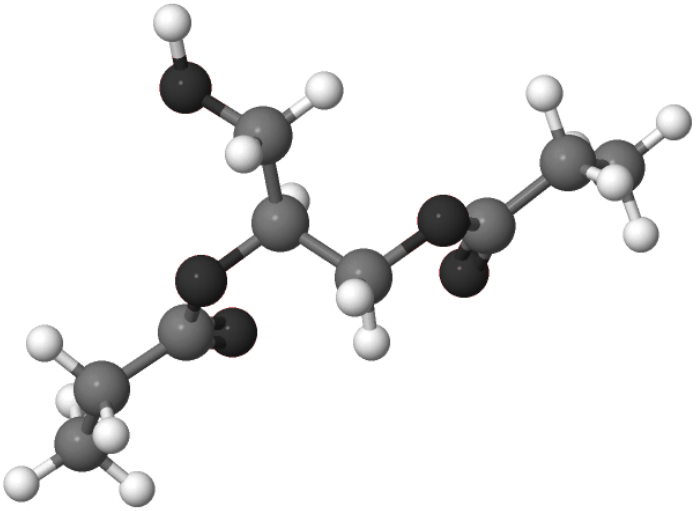

Figure A.8: Dipropionin

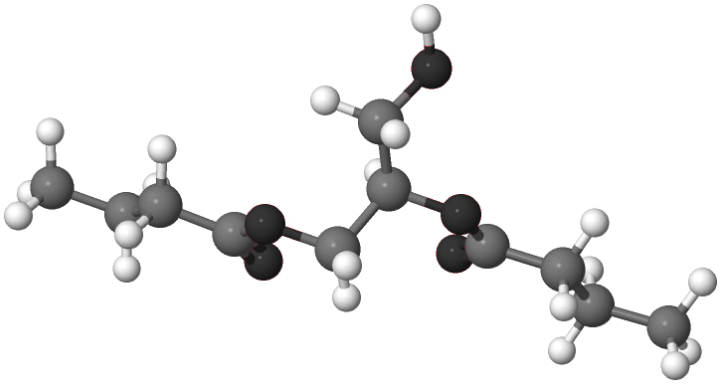

Figure A.9: Dibutyrin

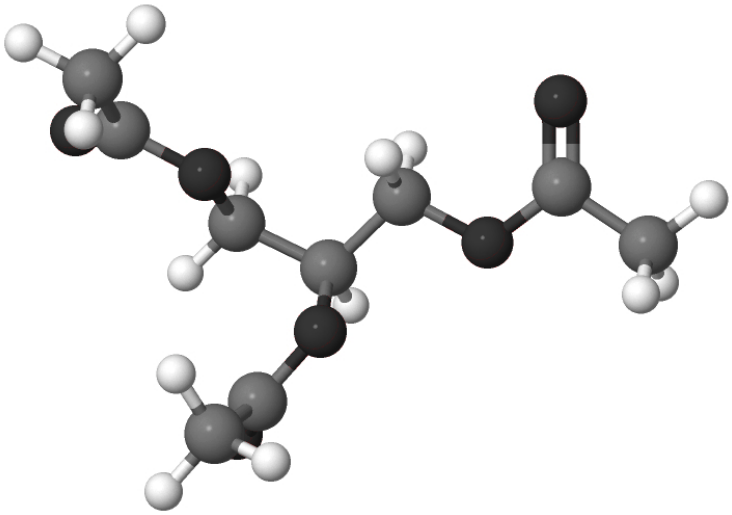

Figure A.10: Triacetin

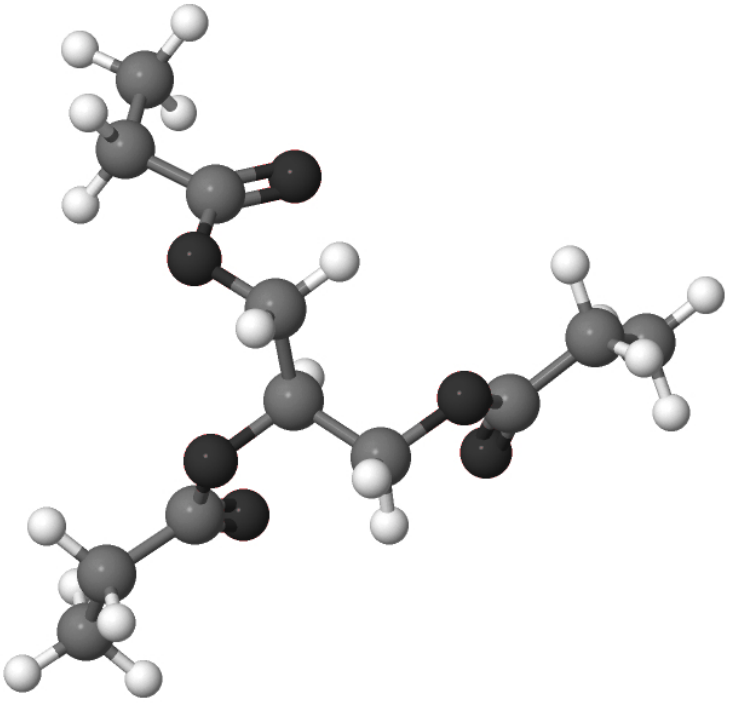

Figure A.11: Tripropionin

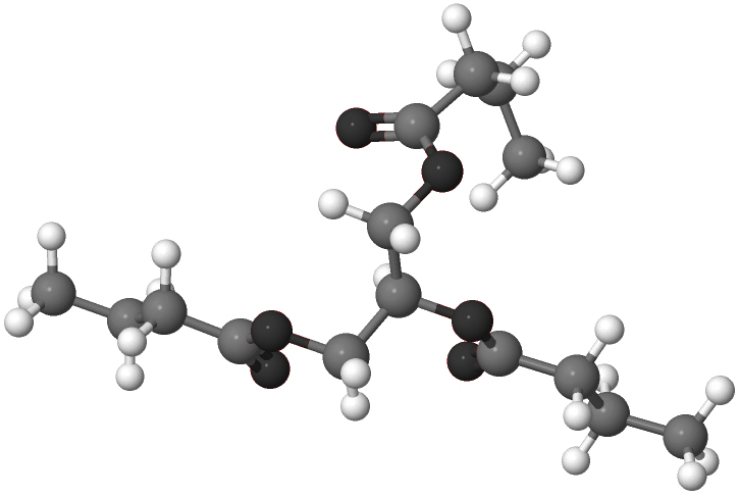

Figure A.12: Tributyrin

APPENDIX B

Supplementary material for Chapter 4

This appendix presents supplementary results of the numerical simulations used in Chapter 4. In the figures below, pressure traces obtained for a large range of equivalence ratio are compared to experimental results and computational results of Hessel et al. [81]. Experimental and numerical results are in good agreement.

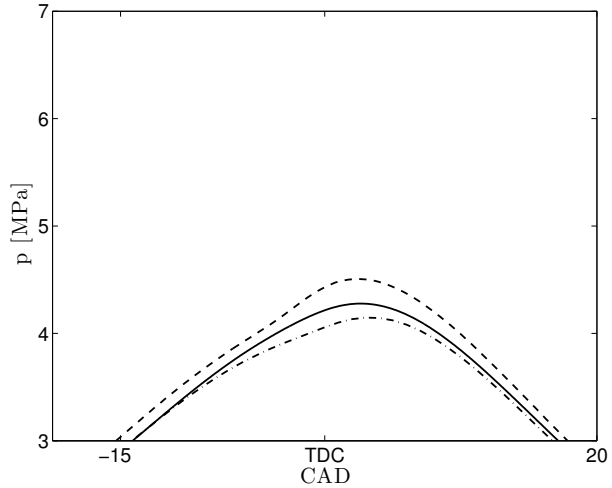

Figure B.1: Pressure near TDC, $\phi = 0.1$. Dash-dotted: Hessel et al. [81]. Dashed: Experiments [81]. Solid: Current study.

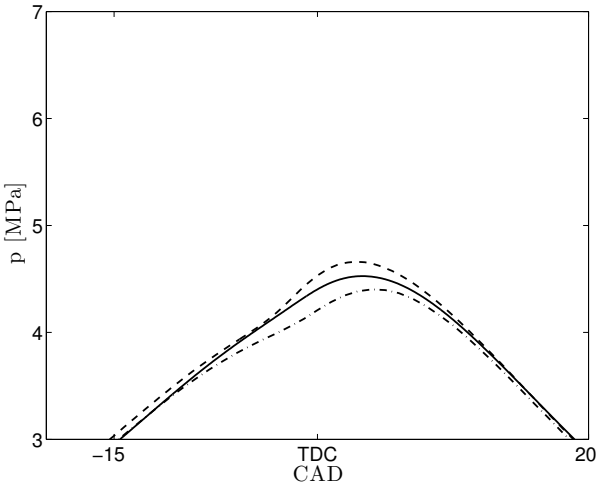

Figure B.2: Pressure near TDC, $\phi = 0.12$. Dash-dotted: Hessel et al. [81]. Dashed: Experiments [81]. Solid: Current study.

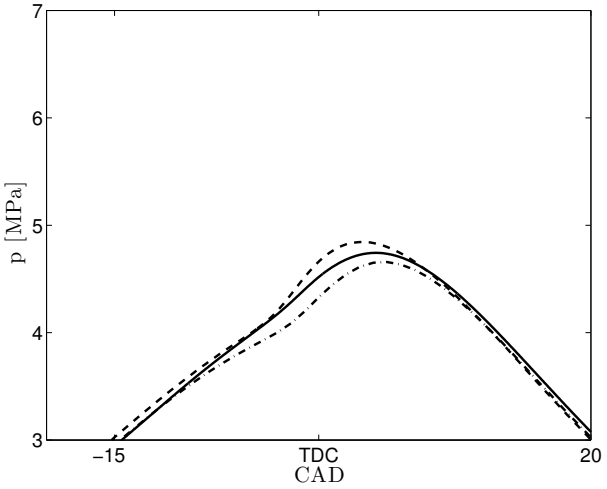

Figure B.3: Pressure near TDC, $\phi = 0.14$. Dash-dotted: Hessel et al. [81]. Dashed: Experiments [81]. Solid: Current study.

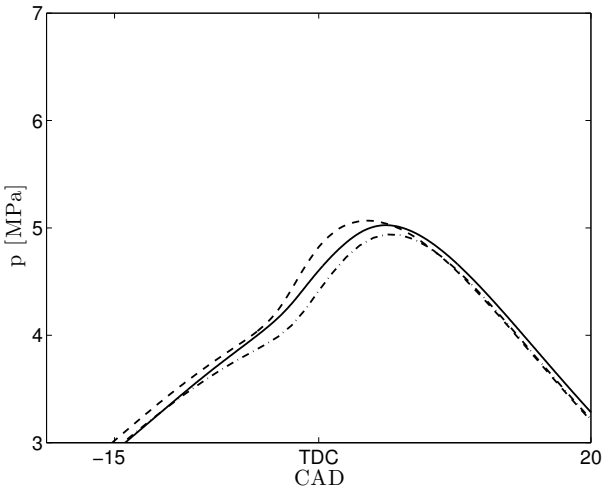

Figure B.4: Pressure near TDC, $\phi = 0.16$. Dash-dotted: Hessel et al. [81]. Dashed: Experiments [81]. Solid: Current study.

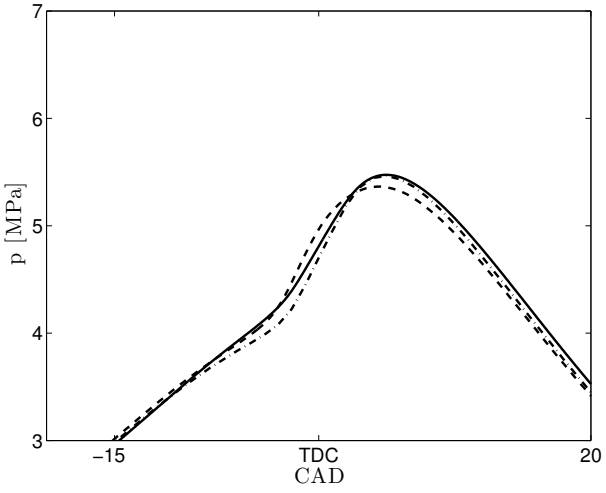

Figure B.5: Pressure near TDC, $\phi = 0.18$. Dash-dotted: Hessel et al. [81]. Dashed: Experiments [81]. Solid: Current study.

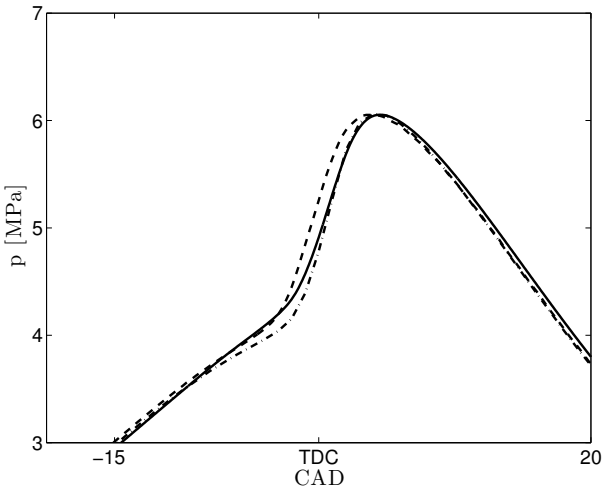

Figure B.6: Pressure near TDC, $\phi = 0.22$. Dash-dotted: Hessel et al. [81]. Dashed: Experiments [81]. Solid: Current study.

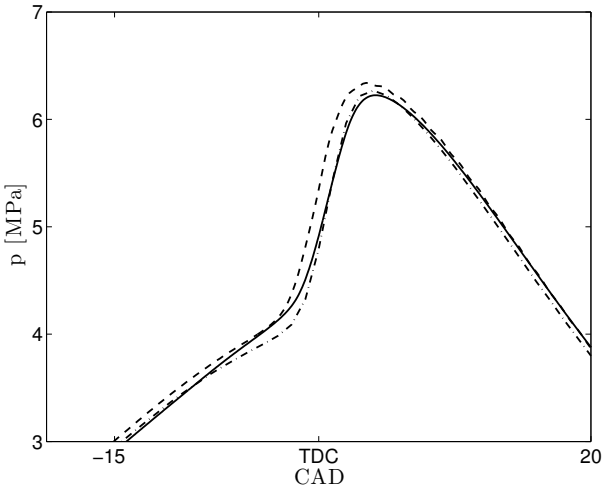

Figure B.7: Pressure near TDC, $\phi = 0.24$. Dash-dotted: Hessel et al. [81]. Dashed: Experiments [81]. Solid: Current study.

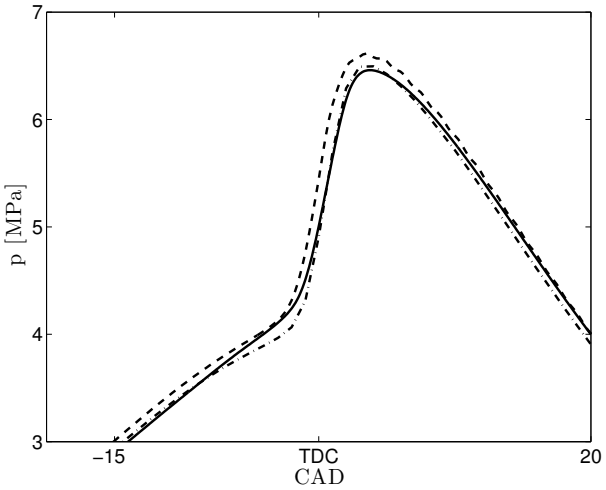

Figure B.8: Pressure near TDC, $\phi = 0.26$. Dash-dotted: Hessel et al. [81]. Dashed: Experiments [81]. Solid: Current study.

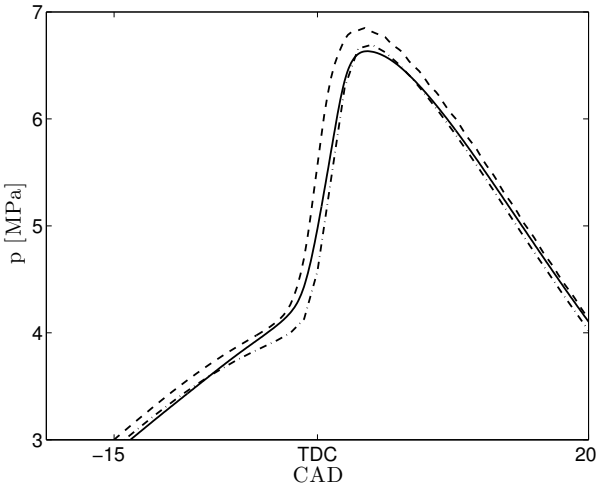

Figure B.9: Pressure near TDC, $\phi = 0.28$. Dash-dotted: Hessel et al. [81]. Dashed: Experiments [81]. Solid: Current study.

APPENDIX C

Pseudo-code of the methods in Chapter 6

This appendix presents the pseudo code of the five methods described in Chapter 6.

Directed Relation Graph (DRG)

This is a modified version of the pseudo code presented in [96].

1) Linear time computation of r_{AB}^{DRG}

for all reactions i **do**
  $\omega_i \leftarrow \omega_{fi} - \omega_{bi}$
  $\nu_{Ai} \leftarrow$ stoech. coef. of A in i
  for all species pairs A, B involved in i **do**
    if edge $A \rightarrow B$ **not** initialized **then**
      init $r_{num}[A][B]$
      $r_{num}[A][B] \leftarrow |\nu_{Ai} * \omega_i|$
    else
      $r_{num}[A][B] \leftarrow r_{num}[A][B] + |\nu_{Ai} * \omega_i|$
    end if
    $r_{den}[A] \leftarrow |\nu_{Ai} * \omega_i|$
  end for
end for
for all species A **do**
  for all initialized edges $A \rightarrow B$ **do**
    $r[A][B] \leftarrow r_{num}[A][B]/r_{den}[A]$
  end for

end for

2) Depth-first search

for all target species T **do**
PUSH(Q, T) // add T on top of FIFO stack Q
activeSpecies$[T] \leftarrow$ **true**
end for
while Q **not** empty **do**
$M_i \leftarrow$ POP(Q) // remove and return top of stack Q
for all initialized edges $M_i \rightarrow M_j$ **do**
if $r[M_i][M_j] \geqslant \epsilon$ **and** activeSpecies$[M_j]$ is **false then**
PUSH(Q, M_j)
activeSpecies$[M_j] \leftarrow$ **true**
end if
end for
end while

3) Skeletal mechanism

for all reactions i **do**
for all species A involved in i **do**
if activeSpecies$[A]$ **not true then**
DISABLE(i)
break
end if
end for
end for
return activeSpecies

Directed Relation Graph with Error Propagation (DRGEP)

1) Linear time computation of r_{AB}^{DRGEP}

for all reactions i **do**
$\omega_i \leftarrow \omega_{fi} - \omega_{bi}$
$\nu_{Ai} \leftarrow$ stoech. coef. of A in i
for all species pairs A, B involved in i **do**

if edge $A \rightarrow B$ **not** initialized **then**
init $r_{num}[A][B]$
$r_{num}[A][B] \leftarrow \nu_{Ai} * \omega_i$
else
$r_{num}[A][B] \leftarrow r_{num}[A][B] + \nu_{Ai} * \omega_i$
end if
if $(\nu_{Ai} * \omega_i) \geqslant 0$ **then**
$P[A] \leftarrow \nu_{Ai} * \omega_i$
else
$C[A] \leftarrow -\nu_{Ai} * \omega_i$
end if
end for
end for
for all species A **do**
for all initialized edges $A \rightarrow B$ **do**
$r[A][B] \leftarrow |r_{num}[A][B]| / \max(P[A], C[A])$
end for
end for

2) Scaling

for all element e **do**
for all species A **do**
$P[e] \leftarrow P[e] + N_{e,A} * \max(0, P[A] - C[A])$
$C[e] \leftarrow C[e] + N_{e,A} * \max(0, C[A] - P[A])$
end for
end for
for all target species T **do**
$\alpha_T \leftarrow \max_{\text{all elements e}} N_{e,T} * |P[T] - C[T]| / P[e]$
end for
call DFS()

3) Group-based direct interaction coefficients

while Ndisabled $\geqslant$ NGB **do** // NGB = 100 in our study
partialSortLow(R,NGB) // sort the NGB lowest value in front of R
disable(R,NGB) // disable the NGB first entry of R
for all initialized edges $A \rightarrow B$ **do**

$r_{num}[A][B] \leftarrow 0$
end for
for all reactions i **do**
$\omega_i \leftarrow \omega_{fi} - \omega_{bi}$
$\nu_{Ai} \leftarrow$ stoech. coef. of A in i
if reaction i contains disabled species **then**
for all species A involved in i **do**
for all initialized edges $A \rightarrow B$ **do**
$r_{num}[A][B] \leftarrow r_{num}[A][B] + \nu_{Ai} * \omega_i$
end for
end for
else
for all species pairs A, B involved in i **do**
$r_{num}[A][B] \leftarrow r_{num}[A][B] + \nu_{Ai} * \omega_i$
end for
end if
end for
call DFS()
end while

4) Skeletal algorithm

for all reactions i **do**
for all species A involved in i **do**
if activeSpecies[A] **not true then**
DISABLE(i)
break
end if
end for
end for
return activeSpecies

Definition of function DFS

function DFS()
for all species A **do**
$R[A] \leftarrow 0$

end for
for all target species T **do**
if $\alpha_T \geqslant \epsilon$ **then**
PUSH(Q, T) // add T on top of FIFO stack Q
activeSpecies$[T] \leftarrow$ **true**
R[T]=1
end if
end for
while Q **not** empty **do**
$M_i \leftarrow$ POP(Q) // remove and return top of stack Q
for all initialized edges $M_i \rightarrow M_j$ **do**
$Rtemp \leftarrow R[Mi] * r[M_i][M_j]$
if $Rtemp \geqslant \epsilon$ **and** $Rtemp \geqslant R[M_j]$ **then**
PUSH(Q, M_j)
$R[M_j] \leftarrow Rtemp$
activeSpecies$[M_j] \leftarrow$ **true**
end if
end for
end while
end function

Path Flux Analysis (PFA)

1) Computation of the r_{AB}^{P-1st} *and* r_{AB}^{C-1st}
for all reactions i **do**
$\omega_i \leftarrow \omega_{fi} - \omega_{bi}$
$\nu_{Ai} \leftarrow$ stoech. coef. of A in i
for all species pairs A, B involved in i **do**
if link A, B **not** initialized **then**
init $P_s[A][B]$
init $C_s[A][B]$
if $(\nu_{Ai} * \omega_i) \geqslant 0$ **then**
$P_s[A][B] \leftarrow \nu_{Ai} * \omega_i$
else

$C_s[A][B] \leftarrow \nu_{Ai} * \omega_i$
end if
else
if $(\nu_{Ai} * \omega_i) \geqslant 0$ **then**
$P_s[A][B] \leftarrow P_s[A][B] + \nu_{Ai} * \omega_i$
else
$C_s[A][B] \leftarrow C_s[A][B] + \nu_{Ai} * \omega_i$
end if
end if
if $(\nu_{Ai} * \omega_i) \geqslant 0$ **then**
$P[A] \leftarrow \nu_{Ai} * \omega_i$
else
$C[A] \leftarrow -\nu_{Ai} * \omega_i$
end if
end for
end for
for all species A **do**
for all initialized links A, B **do**
$r^{P-1st}[A][B] \leftarrow P_s[A][B]|/\max(P[A], C[A])$
$r^{C-1st}[A][B] \leftarrow C_s[A][B]|/\max(P[A], C[A])$
end for
end for

2) Computation of the r_{AB}^{P-2nd} *and* r_{AB}^{C-2nd}

for all species A **do**
for all initialized links A, B **do**
for all initialized links B, M **do**
if M **not** A **then**
if second generation link A, B **not** initialized **then**
init $r^{P-2nd}[A][B]$
init $r^{C-2nd}[A][B]$
$r^{P-2nd}[A][B] \leftarrow r^{P-1st}[A][M] * r^{P-1st}[M][B]$
$r^{C-2nd}[A][B] \leftarrow r^{C-1st}[A][M] * r^{C-1st}[M][B]$
else
$r^{P-2nd}[A][B] \leftarrow r^{P-2nd}[A][B] + r^{P-1st}[A][M] * r^{P-1st}[M][B]$

$r^{C-2nd}[A][B] \leftarrow r^{C-2nd}[A][B]+r^{C-1st}[A][M]*r^{C-1st}[M][B]$
end if
end if
end for
end for
end for

3) Depth first search with r_{AB}^{PFA}
for all target species T **do**
PUSH(Q, T) // add T on top of FIFO stack Q
activeSpecies$[T] \leftarrow$ **true**
end for
while Q **not** empty **do**
$M_i \leftarrow$ POP(Q) // remove and return top of stack Q
for all initialized first or second generation links $M_i \rightarrow M_j$ **do**
$r[M_i][M_j] \leftarrow r^{P-1st}[M_i][M_j]+r^{C-1st}[M_i][M_j]+r^{P-2nd}[M_i][M_j]+$
$r^{C-2nd}[M_i][M_j]$
if $r[M_i][M_j] \geqslant \epsilon$ **and** activeSpecies$[M_j]$ is **false then**
PUSH(Q, M_j)
activeSpecies$[M_j] \leftarrow$ **true**
end if
end for
end while

4) Skeletal algorithm
for all reactions i **do**
for all species A involved in i **do**
if activeSpecies$[A]$ **not true then**
DISABLE(i)
break
end if
end for
end for
return activeSpecies

Dynamic Adaptive Chemistry (DAC)

1) Computation of the r_{AB}^{DAC}

for all reactions i **do**
  $\omega_i \leftarrow \omega_{fi} - \omega_{bi}$
  $\nu_{Ai} \leftarrow$ stoech. coef. of A in i
  for all species pairs A, B involved in i **do**
    if edge $A \rightarrow B$ **not** initialized **then**
      init $r_{num}[A][B]$
      $r_{num}[A][B] \leftarrow \nu_{Ai} * \omega_i$
    else
      $r_{num}[A][B] \leftarrow r_{num}[A][B] + \nu_{Ai} * \omega_i$
    end if
    if $(\nu_{Ai} * \omega_i) \geqslant 0$ **then**
      $P[A] \leftarrow \nu_{Ai} * \omega_i$
    else
      $C[A] \leftarrow -\nu_{Ai} * \omega_i$
    end if
  end for
end for
for all species A **do**
  for all initialized edges $A \rightarrow B$ **do**
    $r[A][B] \leftarrow |r_{num}[A][B]| / \max(P[A], C[A])$
  end for
end for

2) Computation of ϕ *and* ϕ_l

for all species A **do**
  if A **not** (CO_2 **or** H_2O) **then**
    $N_C \leftarrow N_C + N_{C,A}{}^*Y_A$
    $N_H \leftarrow N_H + N_{H,A}{}^*Y_A$
    $N_O \leftarrow N_O + N_{O,A}{}^*Y_A$
    if $N_{C,A} \geqslant$ **or** A is O_2 **then**
      $N_{l,C} \leftarrow N_{l,C} + N_{C,A}{}^*Y_A$
      $N_{l,H} \leftarrow N_{l,H} + N_{H,A}{}^*Y_A$

$N_{l,O} \leftarrow N_{l,O} + N_{O,A}{}^*Y_A$
end if
end if
end for
$\phi \leftarrow (2{}^*N_C + N_H/2 - z' {}^*N_C)/ (N_O - z' {}^*N_C)$ // z' is O/C in fuel
$\phi_l \leftarrow (2{}^*N_{l,C} + N_{l,H}/2)/ (N_{l,O})$
if $\phi \geqslant 0.001$ **then**
if $\phi_l \geqslant 0.001$ **then**
PUSH(Q,fuel) // add fuel on top of FIFO stack Q
R[fuel]=1
end if
PUSH(Q,CO) // add CO on top of FIFO stack Q
R[CO]=1
PUSH(Q,HO_2) // add HO_2 on top of FIFO stack Q
R[HO_2]=1
else
PUSH(Q,CO_2) // add CO_2 on top of FIFO stack Q
R[CO_2]=1
PUSH(Q,H_2O) // add H_2O on top of FIFO stack Q
R[H_2O]=1
end if

3) Depth first search with R_{AB}

while Q **not** empty **do**
$M_i \leftarrow$ POP(Q) // remove and return top of stack Q
for all initialized edges $M_i \rightarrow M_j$ **do**
$Rtemp \leftarrow R[Mi] * r[M_i][M_j]$
if $Rtemp \geqslant \epsilon$ **and** $Rtemp \geqslant R[M_j]$ **then**
PUSH(Q, M_j)
$R[M_j] \leftarrow Rtemp$
activeSpecies[M_j] $\leftarrow$ **true**
end if
end for
end while

4) Skeletal algorithm

for all reactions i **do**
  for all species A involved in i **do**
    if activeSpecies[A] **not true then**
      DISABLE(i)
      break
    end if
  end for
end for
return activeSpecies

Element Flux Analysis (EFA)

1) Computation of $\dot{a}_{AB}$ for all source-sink pairs

for all reactions i **do**
  for all species S in i **do**
    $N_{a,i} \leftarrow N_{a,i} + N_a[S]$
  end for
  for all source-sink pairs A, B involved in i **do**
    if pair A, B **not** initialized **then**
      for all elements a **do**
        init $\dot{a}[A][B]$
        $\dot{a}[A][B] \leftarrow (|\omega_{fi}| + |\omega_{bi}|) * N_a[A] * N_a[B]/N_{a,i}$
        $\dot{a}_{\text{tot}} \leftarrow \dot{a}_{\text{tot}} + \dot{a}_{AB}$
      end for
    else
      for all elements a **do**
        $\dot{a}[A][B] \leftarrow \dot{a}[A][B] + (|\omega_{fi}| + |\omega_{bi}|) * N_a[A] * N_a[B]/N_{a,i}$
        $\dot{a}_{\text{tot}} \leftarrow \dot{a}_{\text{tot}} + \dot{a}_{AB}$
      end for
    end if
  end for
end for
for all initialized source-sink pairs A, B **do**
  for all elements a **do**
    $\dot{a}[A][B] \leftarrow \dot{a}[A][B]/\dot{a}_{\text{tot}}$

```
    end for
  end for
2) Selection of the source-sink pairs
  cumFlux ← 0
  while cumFlux ⩽ cutoff do
    for all elements a do
      idx ← partialSortHigh(ȧ,SSF)
      for i = 1 to SSF do
        activeSpecies[idx[i]] ← true// idx keeps track of the species
        ID
        remove(ȧ, i)
      end for
    end for
  end while
3) Skeletal algorithm
  for all reactions i do
    for all species A involved in i do
      if activeSpecies[A] not true then
        DISABLE(i)
        break
      end if
    end for
  end for
  return activeSpecies
```

APPENDIX D

Supplementary material for Chapter 6

This appendix presents supplementary results of the numerical simulations used in Chapter 6.

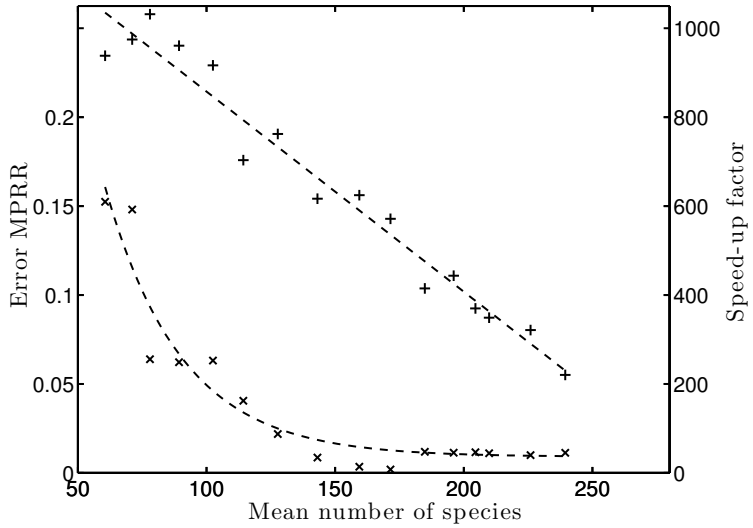

Figure D.1: Error (left axis) on MPRR and speed-up (right axis) for the DRG method.

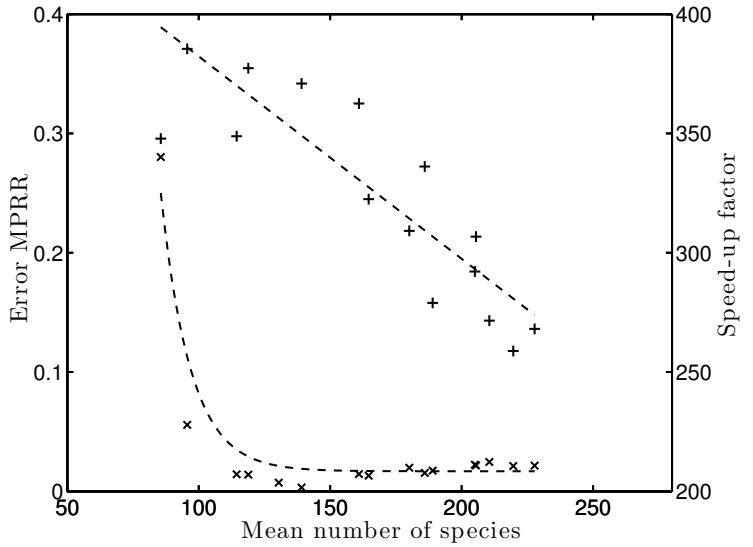

Figure D.2: Error (left axis) on MPRR and speed-up (right axis) for the DRGEP method.

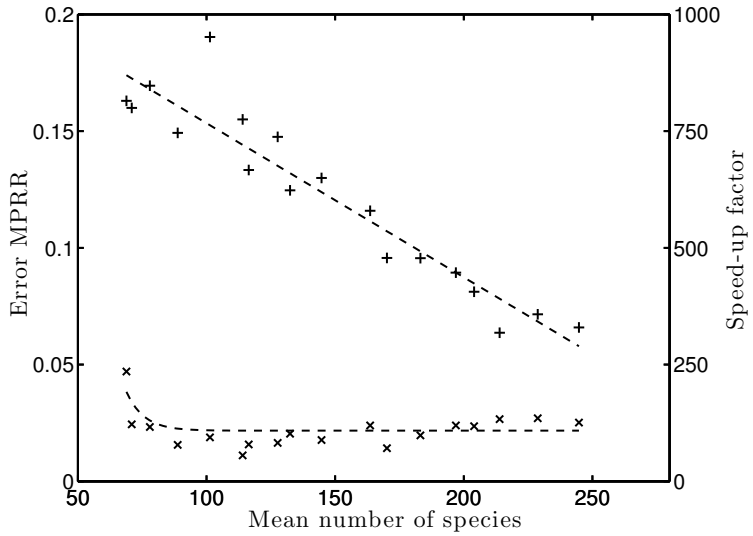

Figure D.3: Error (left axis) on MPRR and speed-up (right axis) for the DAC method.

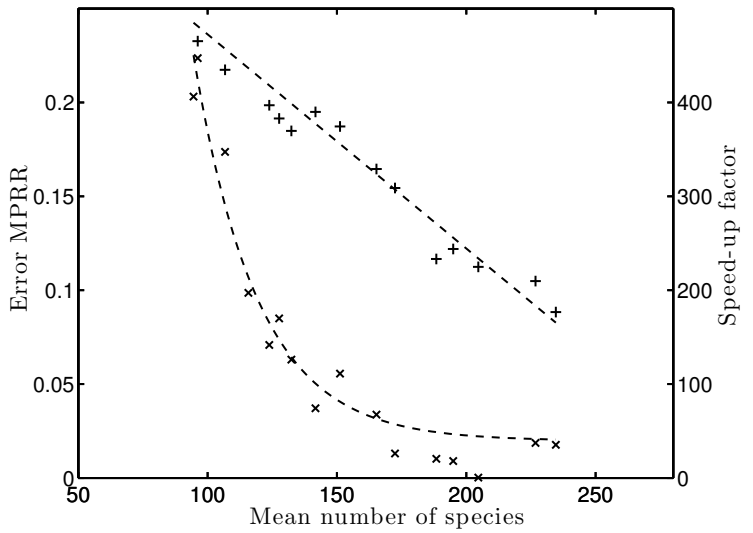

Figure D.4: Error (left axis) on MPRR and speed-up (right axis) for the EFA method.

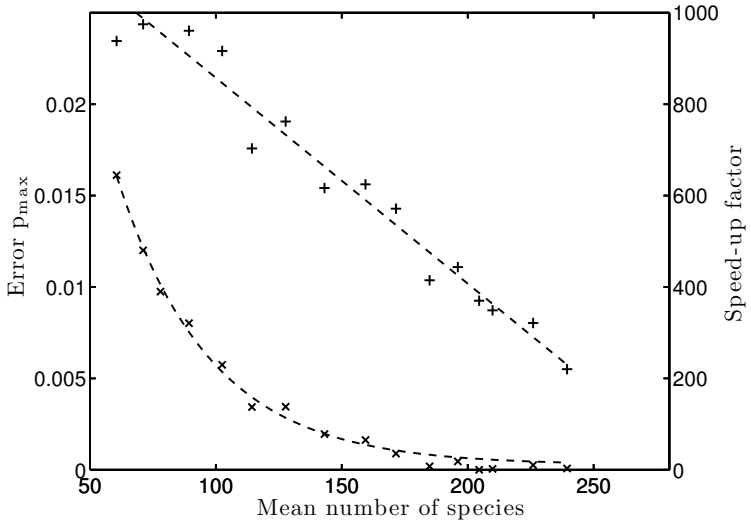

Figure D.5: Error (left axis) on p_{max} and speed-up (right axis) for the DRG method.

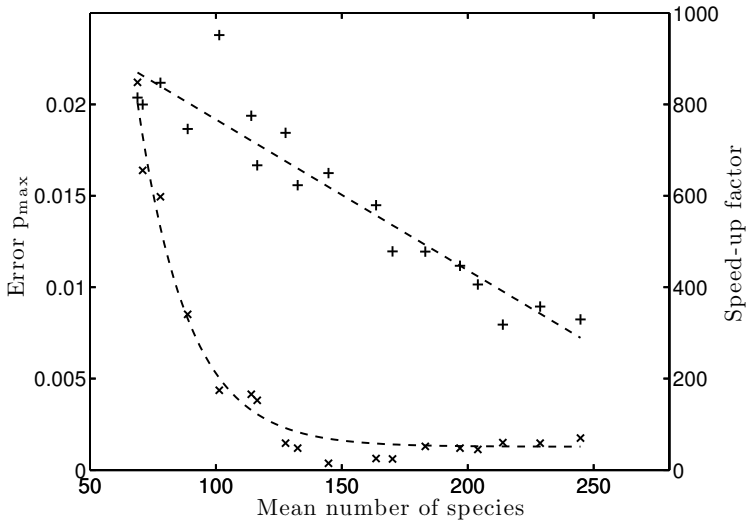

Figure D.6: Error (left axis) on p_{max} and speed-up (right axis) for the DAC method.

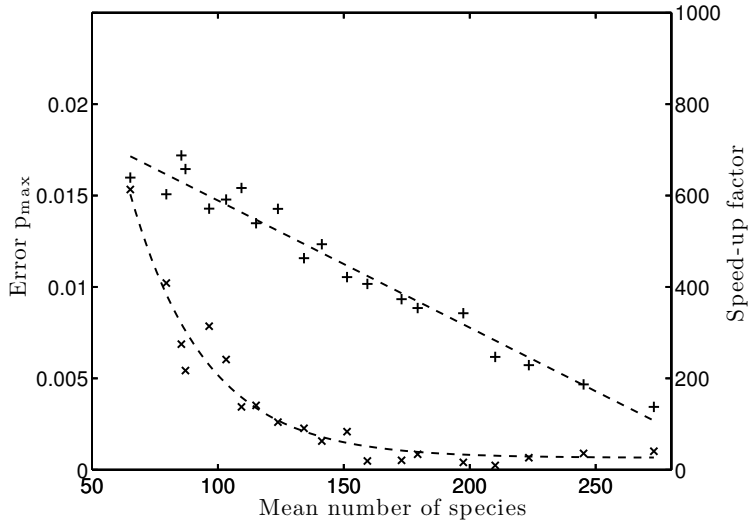

Figure D.7: Error (left axis) on p_{max} and speed-up (right axis) for the PFA method.

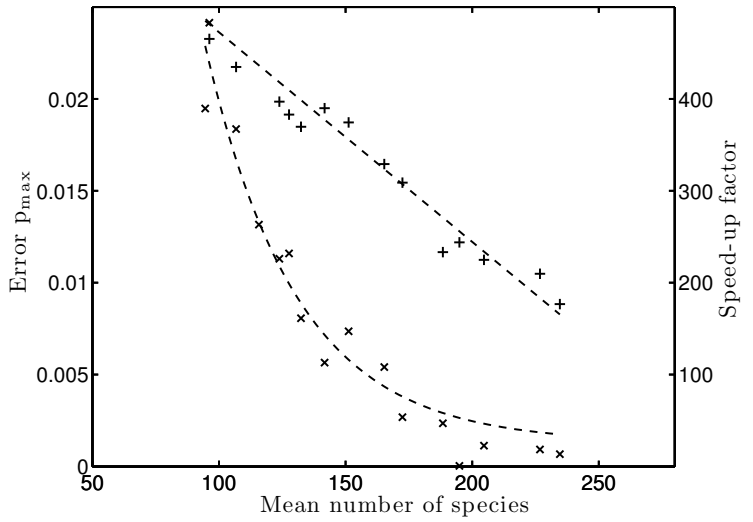

Figure D.8: Error (left axis) on p_{max} and speed-up (right axis) for the EFA method.

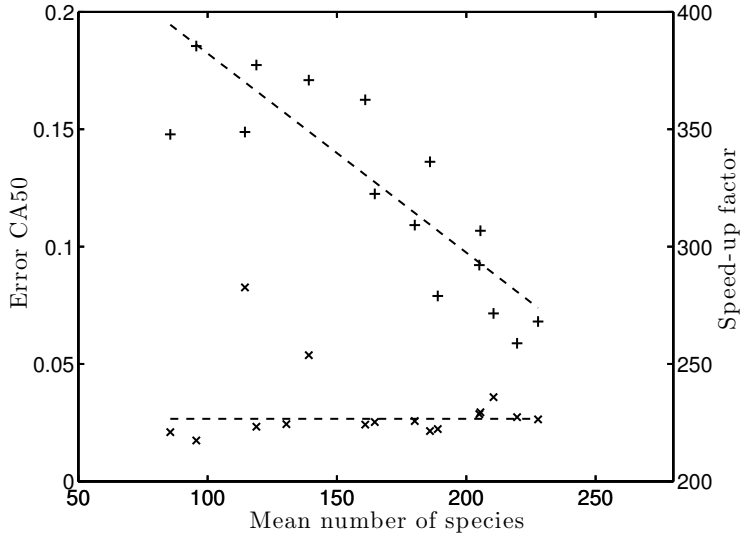

Figure D.9: Error (left axis) on CA50 and speed-up (right axis) for the DRGEP method.

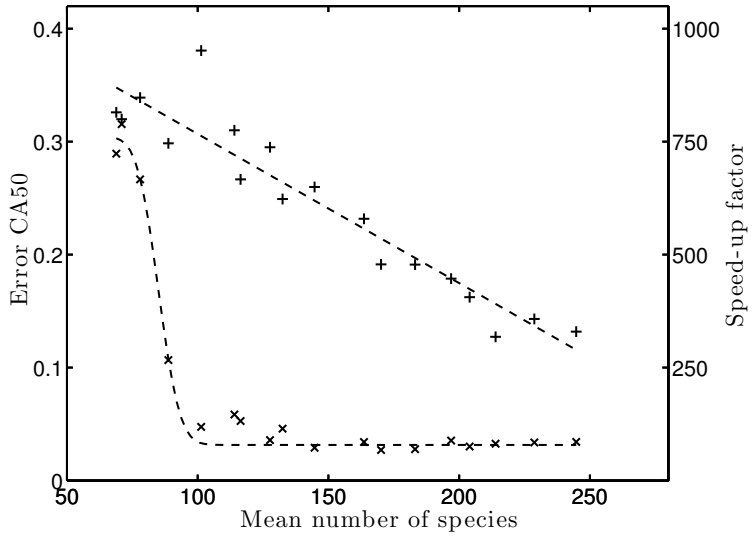

Figure D.10: Error (left axis) on CA50 and speed-up (right axis) for the DAC method.

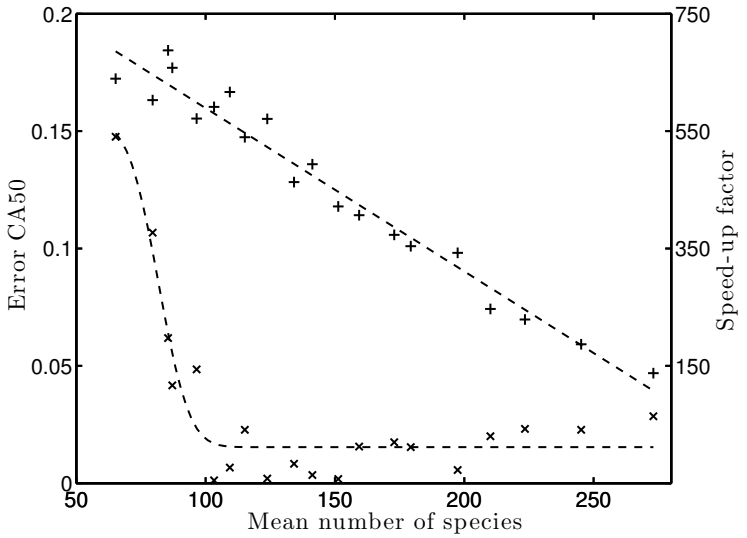

Figure D.11: Error (left axis) on CA50 and speed-up (right axis) for the PFA method.

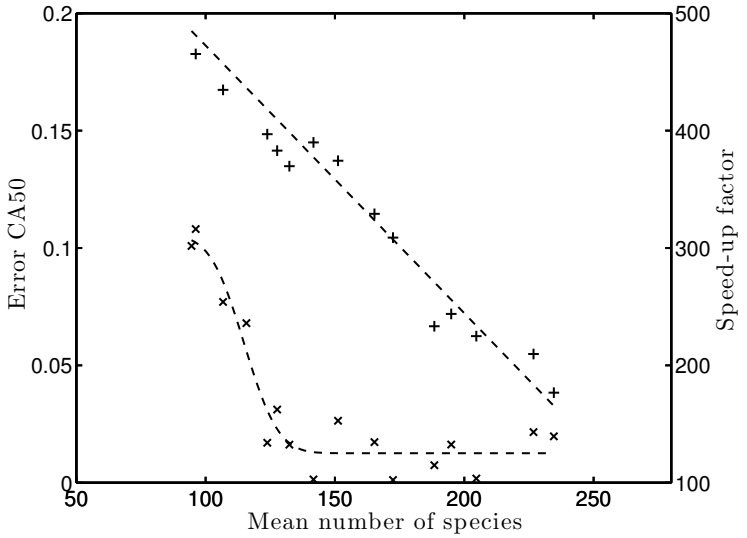

Figure D.12: Error (left axis) on CA50 and speed-up (right axis) for the EFA method.

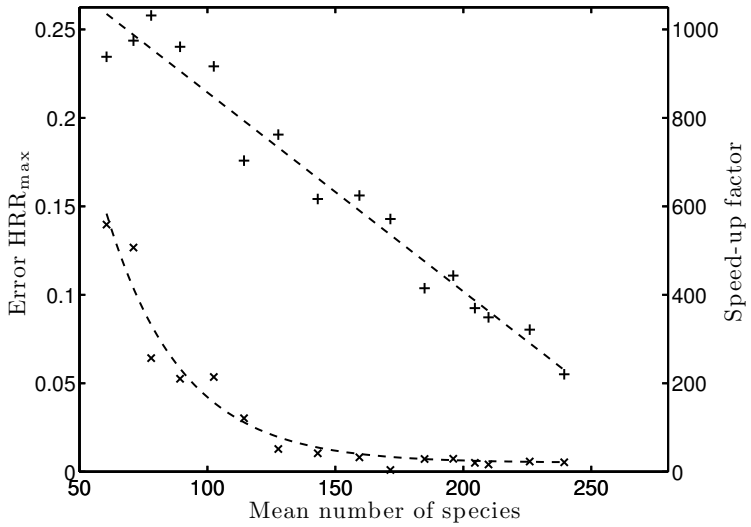

Figure D.13: Error (left axis) on HRR_{max} and speed-up (right axis) for the DRG method.

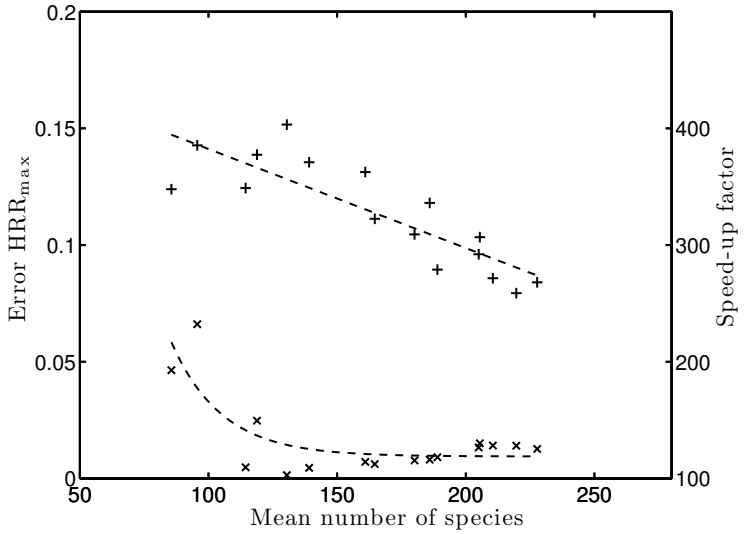

Figure D.14: Error (left axis) on HRR_{max} and speed-up (right axis) for the DRGEP method.

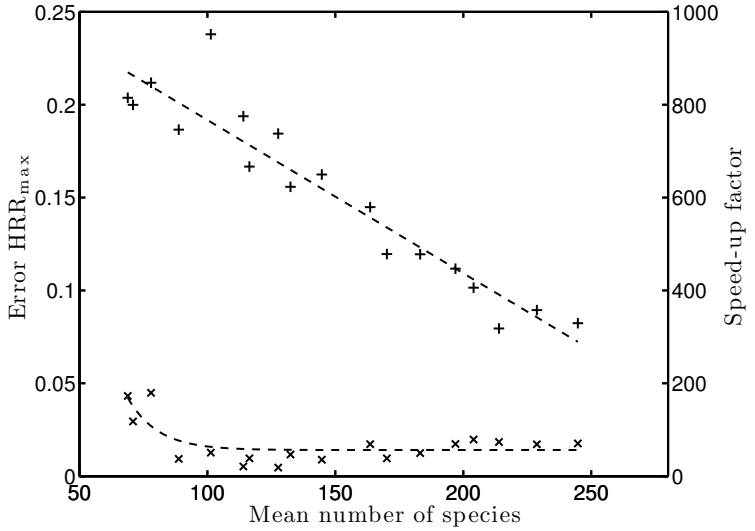

Figure D.15: Error (left axis) on HRR_{max} and speed-up (right axis) for the DAC method.

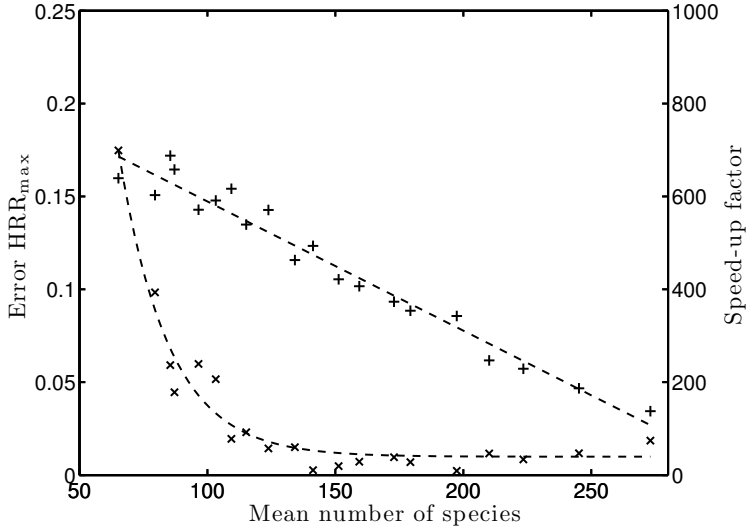

Figure D.16: Error (left axis) on HRR_{max} and speed-up (right axis) for the PFA method.

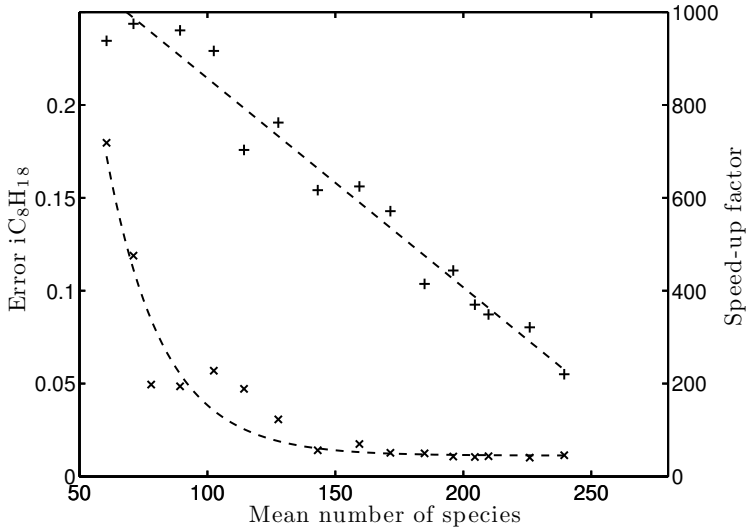

Figure D.17: Error (left axis) on the fuel (iC_8H_{18}) mass fraction based on equation (6.31) and speed-up (right axis) for the DRG method.

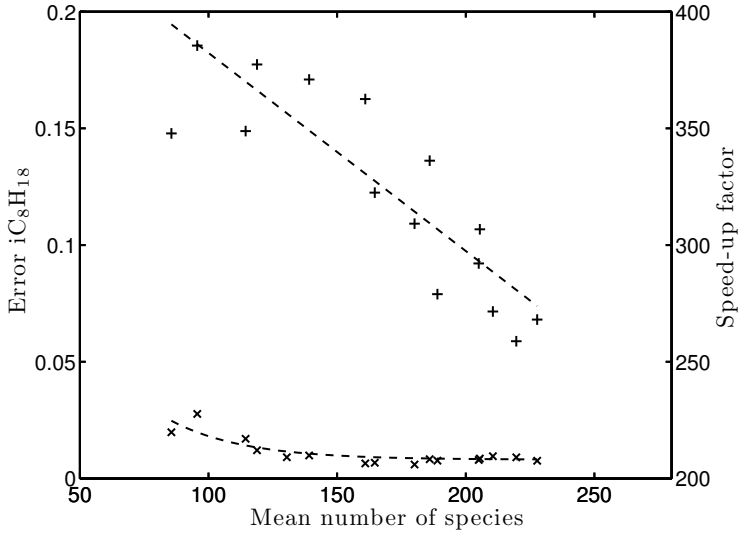

Figure D.18: Error (left axis) on the fuel (iC_8H_{18}) mass fraction based on equation (6.31) and speed-up (right axis) for the DRGEP method.

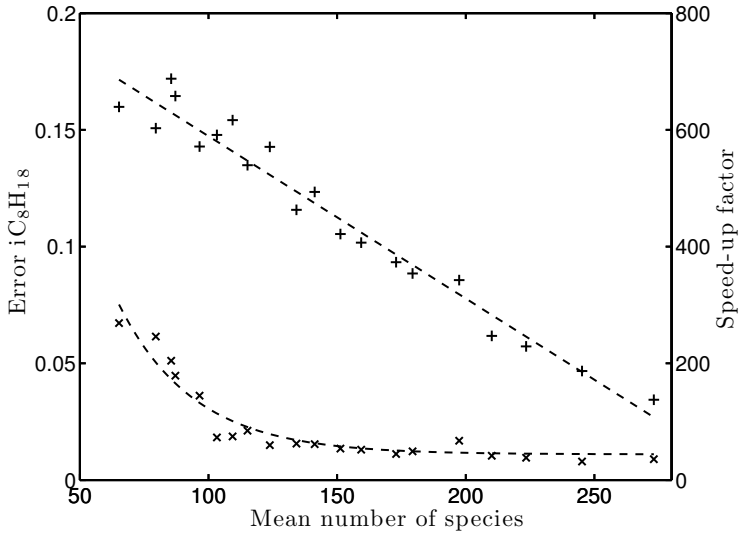

Figure D.19: Error (left axis) on the fuel (iC_8H_{18}) mass fraction based on equation (6.31) and speed-up (right axis) for the PFA method.

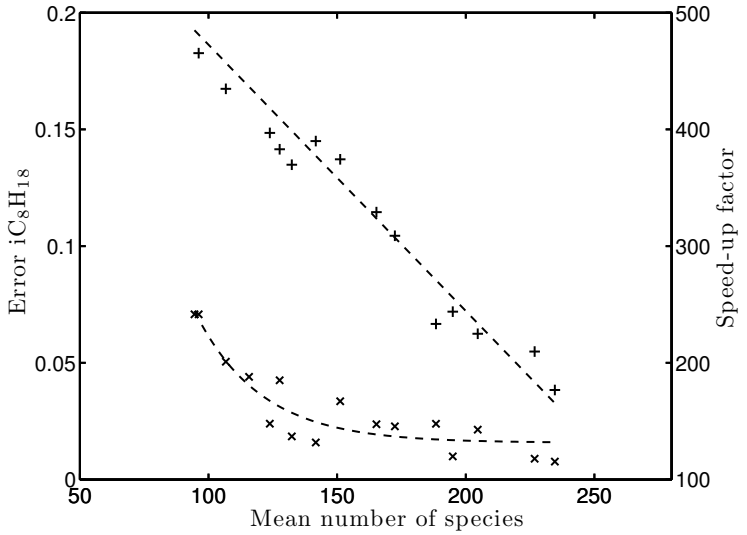

Figure D.20: Error (left axis) on the fuel (iC_8H_{18}) mass fraction based on equation (6.31) and speed-up (right axis) for the EFA method.

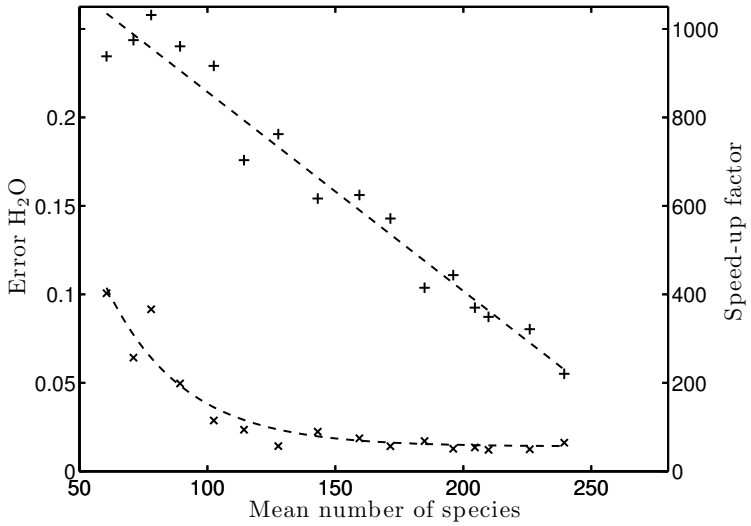

Figure D.21: Error (left axis) on H_2O mass fraction based on equation (6.31) and speed-up (right axis) for the DRG method.

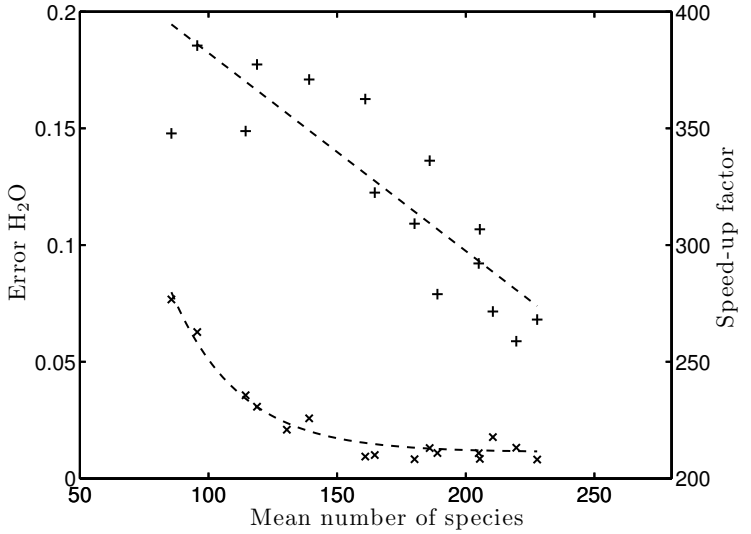

Figure D.22: Error (left axis) on H_2O mass fraction based on equation (6.31) and speed-up (right axis) for the DRGEP method.

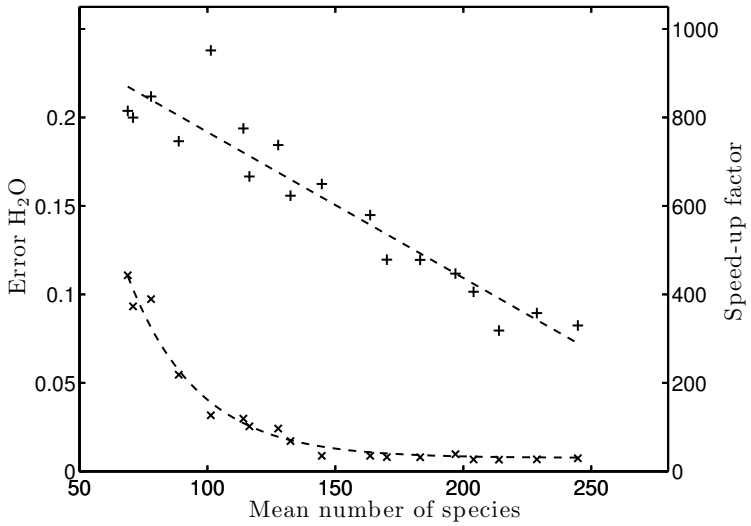

Figure D.23: Error (left axis) on H_2O mass fraction based on equation (6.31) and speed-up (right axis) for the DAC method.

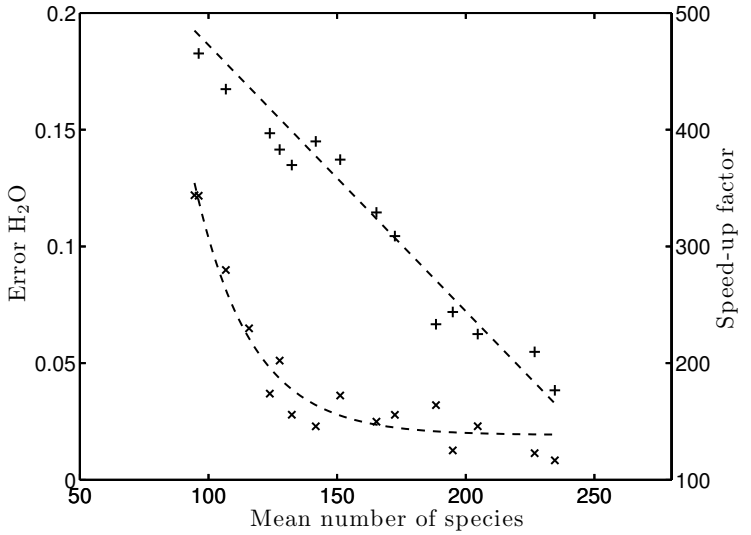

Figure D.24: Error (left axis) on H_2O mass fraction based on equation (6.31) and speed-up (right axis) for the EFA method.

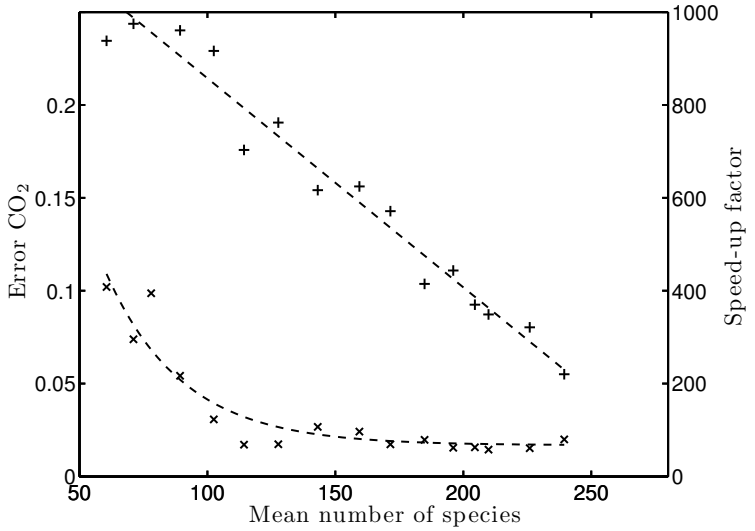

Figure D.25: Error (left axis) on CO_2 mass fraction based on equation (6.31) and speed-up (right axis) for the DRG method.

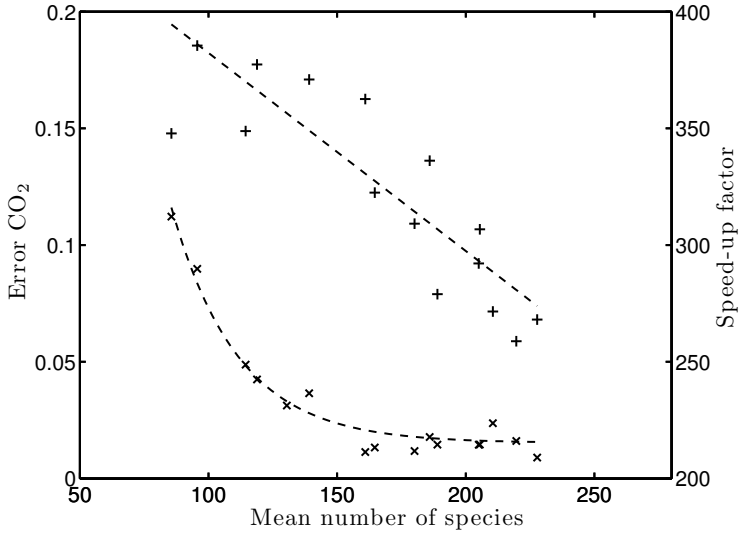

Figure D.26: Error (left axis) on CO_2 mass fraction based on equation (6.31) and speed-up (right axis) for the DRGEP method.

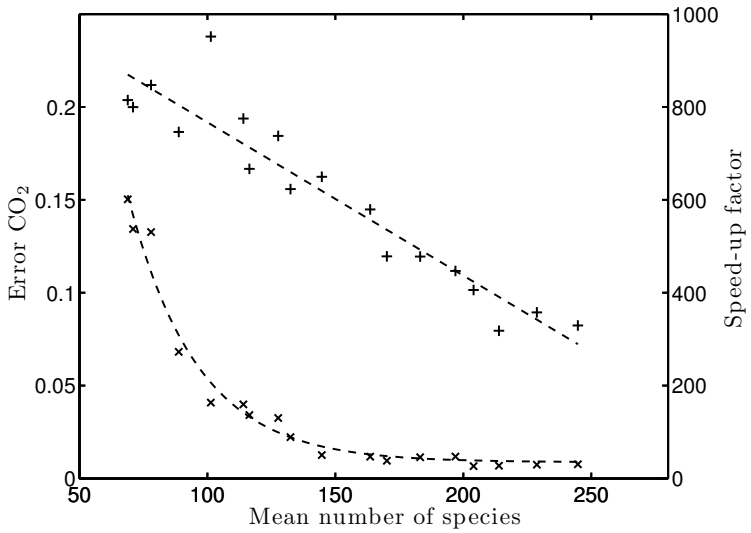

Figure D.27: Error (left axis) on CO_2 mass fraction based on equation (6.31) and speed-up (right axis) for the DAC method.

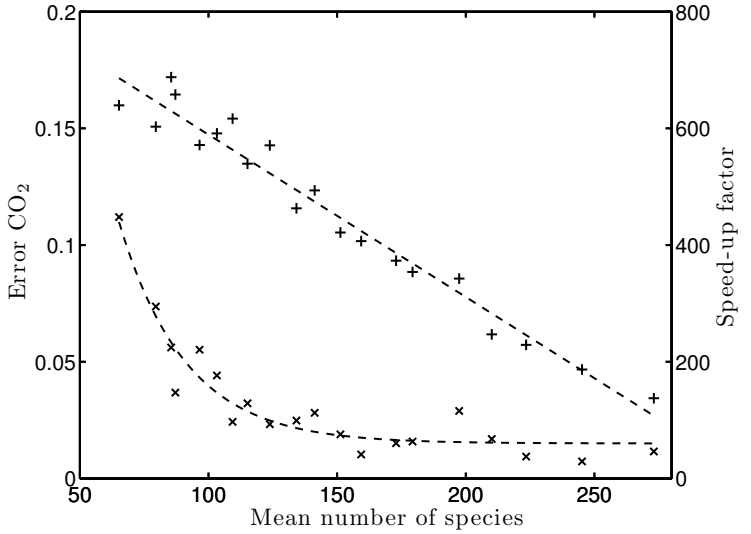

Figure D.28: Error (left axis) on CO_2 mass fraction based on equation (6.31) and speed-up (right axis) for the PFA method.